Visual Navigation of a Virtual Blowfly

Jens Peter Lindemann

Dipl. Inform. Jens Peter Lindemann
email: jlindema@techfak.uni-bielefeld.de

Abdruck der genehmigten Dissertation[1]
zur Erlangung des akademischen Grades Doktor-Ingenieur (Dr. Ing).

Der Technischen Fakultät der Universität Bielefeld
am 8. Dezember 2005 vorgelegt von Jens Peter Lindemann.

Gutachter:

- Prof. Dr. Gerhard Sagerer
- Prof. Dr. Martin Egelhaaf

Prüfungsausschuss:

- Prof. Dr. Helge Ritter
- Prof. Dr. Gerhard Sagerer
- Prof. Dr. Martin Egelhaaf
- Dr. Robert Haschke

---

[1] Gedruckt auf alterungsbeständigem Papier nach ISO 9706

Acknowledgements

The virtual blowfly presented in this thesis — like most scientific projects — is the result of teamwork. Therefore in the first place I want to thank the team, the members of the Neurobiology Department of Bielefeld University for the many fruitful and encouraging discussions.

I thank my principal advisor Martin Egelhaaf for his many helpful advises and for making it possible for me to work on this project. I also thank Martin Egelhaaf for his appreciation of my personal situation as a father of small children having to spend a substantial amount of energy and time for them.

Gerhard Sagerer and Helge Ritter gave me the opportunity to defend my interdisciplinary project in the technical faculty and to receive a doctor's degree in engineering while working in the biology.

My work on this project was funded by the graduate program Strategies and Optimisation of Behaviour.

Hans van Hateren helped me a lot in discussions regarding the sensory model and with his aid on the analysis of the responses to behaviourally generated stimuli.

Last but not least I want to thank my family. My parents both had their part in seeding the interests that led me through this project. On the one hand, my father, an electronics engineer by himself, started my technical interest. My mother, on the other hand, facilitated my interest in natural sciences in every possible way.

I especially want to thank my dear wife Elke and my sons Erik and Till for the support and the patience they showed during the last years.

Visual Navigation of a Virtual Blowfly

Dissertation zur Erlangung des akademischen Grades
Doktor der Ingenieurwissenschaften (Dr.-Ing.)

der Technischen Fakultät der Universität Bielefeld
vorgelegt von

Jens Peter Lindemann

Bielefeld, November 2005

Contents

1 Introduction

When an animal or a “sighted” robot moves around, the image of the environment moves on its retina or camera sensor accordingly. These characteristic image movements, constituting the so-called “optic flow”, contain information about both the ego-motion of the system and the spatial structure of the surrounding. For many animals the correct interpretation of the optic flow is essential for the control of ego-motion. Especially fast flying insects depend to a high degree on the visual control of their flight manoeuvres.

Obstacle avoidance, for instance, is only possible for these animals by the use of visual information. Also for the estimation of flight speed and heading direction, vision is important. Wind sensing only gives information of the relative movements between the animal and the surrounding air volume. Sensing the absolute trajectory above ground based on wind cues is impossible, because the ego-motion of the animal is superimposed by the movements of the surrounding air in these signals. Furthermore, airborne insects are very likely incapable of sensing the gravity field which means that they cannot use it to control their orientation in space. Dipteran insects (flies, mosquitos) are equipped with mechanical sensing organs (halteres) registering self-rotations of the animal, but this system is limited to relatively high dynamic stimulation and cannot sense slow drift movements (Hengstenberg et al., 1986; Nalbach, 1994).

Even for longterm navigation the optic flow can be useful. For bees the estimation of distance flown is thought to be derived from the integration of optic flow (for review see Srinivasan and Zhang, 2003).

The analysis of optic flow is a complicated task, which is not yet satisfactorily solved for technical systems. While it is relatively straightforward to compute the ego-motion parameters of a mobile system from the local image velocities, the reliable correct estimation of these velocities from real-world images causes problems. Approaches to control mobile robots on optic flow information are characterised by a high computational effort and are often restricted to certain types of environment. In contrast to that, animals are clearly capable of analysing the visual information in real time and within almost arbitrary environments. While they evolved in differently structured environments, flies can easily deal also with artificial environments created by man.

That small flying insects successfully navigate based on optic flow information using a relatively small group of a few thousand neurons, makes it likely that these animals developed very efficient mechanisms for this task. It is therefore interesting for technical applications to investigate the solutions that nature found for this problem and to use them as a blueprint or at least as inspiration for the development of technical systems.

An important animal model for the investigation of mechanisms of optic flow processing in the neurobiology and biological cybernetics is the blowfly. Different species have been investigated, the most prominent are *Calliphora vicina*, a red-eyed blowfly and *Lucilia sericata*, a greenish sheep fly. Besides these, a much smaller fly has been used for behavioural studies, *Drosophila melanogaster*, which is also an important model organism in genetical research.

The mechanisms of motion information processing implemented in the visual system of these animals are known in such detail, that an algorithmic model exists which can easily be simulated by technical systems (Kern et al., 2001a). See chapter 2 for an overview.

Most research on visual processing has been done using very simple and artificial stimuli in the past. Using simple stimuli was an important precondition for the systematic analysis of the processing mechanisms. It is a traditional method of system analysis to describe a system by its responses to a defined set of test signals. However, it is not trivial that the mechanistic models formulated on the basis of these simple signals are responding in a realistic way also to the more complex signals encountered by the visual system in a behaving animal.

The rapid development of computer hardware recently made it feasible, to use stimuli that are, with respect to dynamics and spatial structure close to signals that a fly is confronted with in unrestricted behaviour. These stimuli are created by reconstructing the retinal images a fly has seen in a video recorded behavioural experiment. By recording the neural activities caused by replaying these images to a fly in an electro-physiological experiment, the internal neural states of the behaving animal can be estimated (Kern et al., 2001b). By replaying the same image sequences to a simulated computer model and by comparing the model output and the electrophysiologically determined responses, the validity of the model derived from the system analysis for more realistic input can be tested (see Chapter 4). It turns out, that the model simulation can reproduce the responses of the cells of an animal with an unexpected degree of fidelity, although the very same traces were suspected to be in disaccordance to the model on first sight.

For the understanding of the visual control for behaviour, the knowledge of the processing done in the sensory part of the visual system is only a first building block. Based on the simulation model and behavioural experiments, the transformation of the sensory signals to the actual reactions of the animal can be studied. As for any system acting in a closed loop and thereby in a recurrent dynamic situation, it is hard for humans to judge hypotheses formulated for the coupling. Already very simple designs can show very complex and unexpected emergent properties, as a simple model (Boeddeker et al., 2003) for the chasing behaviour of the fly shows. A simulation environment that facilitates the test of hypotheses is therefore a valuable tool for this research.

1.1 Structure of the thesis

The first part of this thesis (chapter 2) gives an overview of the fly motion vision system.

Chapter 3 describes technical preconditions for the replay of behaviourally generated optic flow. Section 3.1 describes a software system for the reconstruction of flight paths from video camera data. Section 3.2 discusses the software necessary for the virtual reconstruction of the retinal images the fly has received during flight. Section 3.3 focusses on a specialised display device that allows the replay of computer generated image sequences to the fly's almost omni-directional and very fast vision system.

In chapter 4, the algorithmic model of the fly motion vision system is described in detail and the validity of this model for behaviourally generated optic flow is tested by comparison of the simulation results to the responses measured in electrophysiological experiments.

Chapter 5 gives a first example for the control of behaviour based on the sensory information processed by this model. By simulation of a small feed-forward neuronal system, this activity can be correlated to certain features of the behaviour.

The thesis closes in a conclusion and an outlook given in chapter 6.

1.2 Contribution

With this thesis I contribute a simulation framework for closed-loop simulation of the optic-flow based navigation of a blowfly. Hypotheses drawn from physiological and behavioural analysis of the fly nervous systems can be tested for sustainability by these simulation experiments. As part of the framework I implemented a model of the sensory processing of visual motion stimuli. While the computational structure of this model was taken from literature and is known as one of the most influential computational models in neuroscience, this thesis contributes a systematical parameterisation and quantitative analysis of the model for the response to behaviourally generated stimuli.

Tools for the quantitative analysis of behavioural experiments and for the replay of naturalistic visual motion stimuli in physiological experiments had to be developed as a prerequisite of this analysis. Several contributions to this development are also part of this thesis. This new replay approach revealed that neurons previously assumed to mostly code rotational self-motion of the animal signal information on translational motion and thus indirectly also on the 3D layout of the environment. This finding also is reproduced by the model neurons when stimulated with the same set of stimuli.

The sensory module parameterised to quantitatively reproduce the measured responses of sensory neurons in the fly's visual system forms the input stage to a simple navigational system challenged in closed-loop simulations with the task to avoid the walls of a virtual flight arena. The ability of the system to solve this task under certain conditions shows that the depth information coded in the responses of the sensory neurons can be successfully decoded and used for navigational purposes, on the one hand. That the virtual fly fails under seemingly similar conditions a real fly can easily deal with, shows that certain extensions of the sensory and the controller module are necessary. However, the framework presented here is designed modular so that such extensions can be introduced and tested easily.

2 Processing of optic flow: Fly neuroethology

Neuroethology is a young science field that aims at understanding the neural mechanisms underlying animal behaviour. For the understanding of the visual control of locomotion behaviour, the blowfly is a classical model organism. This chapter gives a short overview of research results in this context. The fly mainly exploits the retinal image movements, the so-called "optic flow" for the control of locomotion. Thus the first section describes some basic properties of optic flow. In the following section, the neuronal system analysing the optic flow pattern is sketched. The typical flight behaviour of blowflies and the resulting effects on the neuronal representation of self motion is outlined. A short review of the research dealing with robots inspired by the fly visual system closes this chapter.

2.1 Optic flow

During ego-motion of an animal or a vision equipped robot, the image of the environment moves on its visual sensors in a characteristic way. These movements are usually referred to as "optic flow". The term "optic flow" was introduced to vision science by Gibson (1950), a psychologist dealing with depth perception. Gibson observed that the retinal image movements caused by ego-motion of an observer carry information about the spatial layout of the environment. He suggested that this information source is used by biological systems for depth perception, detection of moving objects and ego-motion estimation.

2.1.1 Basic types of optic flow

Any movement of an observer can be decomposed into a rotation, given by the rotation axis and the rotation angle, and a translation given by the direction and the translational distance. Two basic types of optic flow are generated by translations of the observer, on the one hand, and by rotations, on the other hand (figure 2.1).

The optic flow generated by rotation does not carry information on the spatial

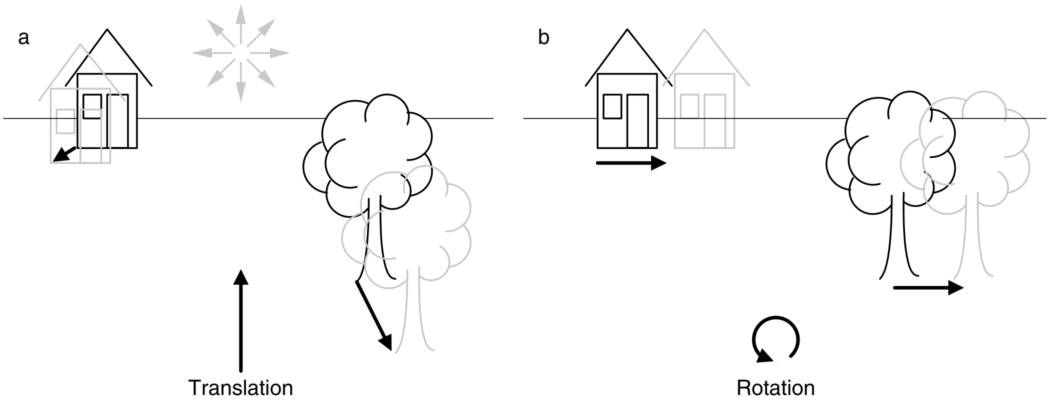

Figure 2.1: The two principal locomotion types generate different optic flow patterns. Translation (a) generates flow with low velocities for distant objects and large velocities for objects close to the observer. Rotation (b) generates image velocities independent of the distance of objects.

layout of the environment, but causes rigid global movements in the visual field. The direction of image motion is perpendicular to the rotational axis in any point of the visual sphere. The local velocities of this flow field do not depend on the distance of an observed object (figure 2.1b), but on the viewing direction of the observed point with respect to the rotational axis. The velocity is zero if the viewing direction is along the rotational axis. It increases with increasing angular difference to this axis with a maximum for viewing directions perpendicular to the rotational axis (see figure 2.2).

For optic flow generated by a pure translation, the direction of image motion only depends on the direction of motion of the observer. Any point in the visual field moves parallel to the direction of the ego-motion. But the local velocities in this case depend on both the viewing direction and the distance of the objects viewed in this direction. For a viewing direction equal to the locomotion direction, the image velocity is zero. This point in the visual field is often referred to as the "focus of expansion", abbreviated FOE. For a given environmental distance, the image velocity is maximal, if the viewing direction is perpendicular to the locomotion direction (figure 2.2). For any point in the visual field, the image velocity depends inversely on the distance between the observer and the environment. This means that objects close to a moving observer seem to move faster than distant objects (figure 2.1a).

Note, that all these properties of the optic flow depend on the assumption that the environment is fixed. Moving objects in the environment also cause retinal image motion, but the direction and velocity of this motion is determined by the relative motion of object and observer, not by the observer's motion alone.

The existence of moving objects in a scene complicates the task of self-motion estimation, on the one hand. On the other hand, the discontinuities in retinal motion resulting from the object motion can be exploited to segregate objects from the stationary background.

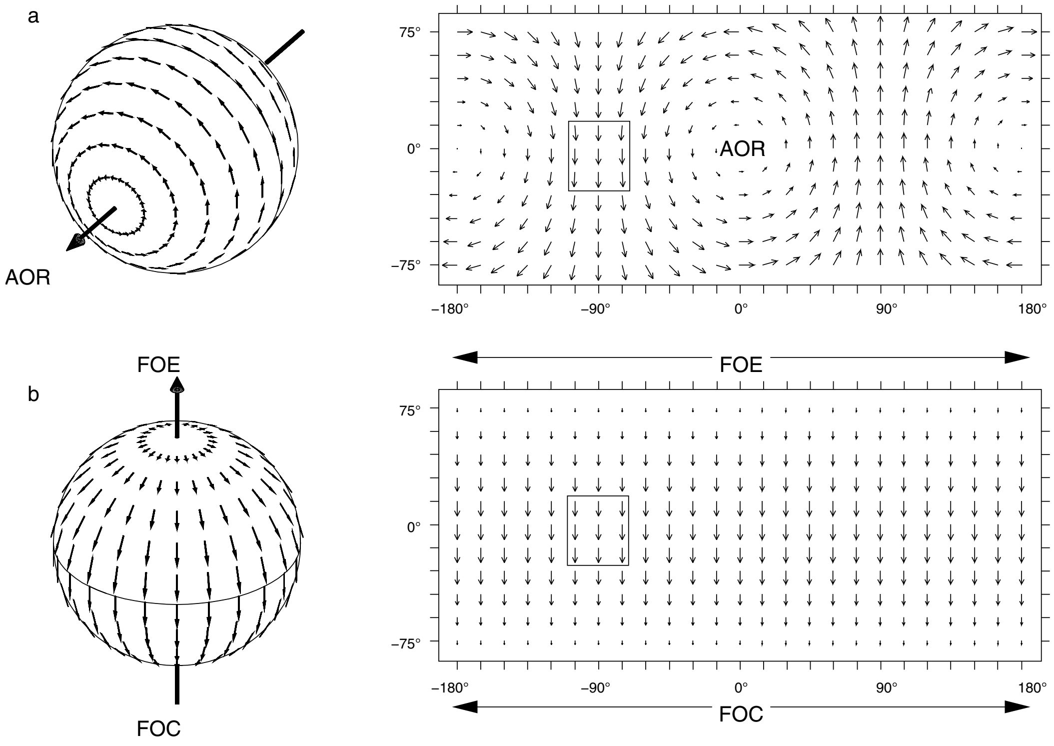

Figure 2.2: The optic flow generated by pure rotation (a) about a rotational axis "AOR" and by a pure translation (b) in the direction indicated by the arrow. The focus of expansion "FOE" and the focus of compression "FOC" of the flow field indicate the direction of movement in the case of pure translation. The right-hand panels show the flow field in a cylindrical projection. Note, that the polar points (FOE, FOC in b) are mapped to the entire x-axis in this projection at an elevation of 90° (not shown in the panels). Note also that the local retinal velocities in certain parts (squares in the cylindrical plot) of the visual field are almost identical for both movements. (Modified from Krapp and Hengstenberg, 1996)

2.1.2 Reconstruction of self-motion parameters

To investigate the possibility of reconstructing the self-motion and the spatial structure from the image movements, Koenderink and van Doorn formulated a simple mathematical model (Koenderink and van Doorn, 1987). In this approach, the environment is represented by a set of three dimensional "fiducial points" D_i in a coordinate system centred in the position of an observer. The projections of these points to a (unit) sphere are given by $d_i = \frac{D_i}{|D_i|}$. The motion of these projected points on the sphere can be computed for a given translation T and a rotation R as follows:

$$p_i = \frac{\delta d_i}{\delta t} = p_i^T + p_i^R = -\frac{T(T \cdot d_i)d_i}{|D_i|} - R \times d_i \tag{2.1}$$

where R is a vector directed along the rotational axis and encoding the angular velocity in its length, T a vector pointing in the direction of the translation and coding the velocity in its length. $\cdot$ denotes the scalar product and $\times$ the vector product.

Note that the distance of the environmental point $|D_i|$ appear only in the flow component determined by the translation vector. The equation further represents that the rotational (p_i^R) and translational (p_i^T) components of the flow field are additive. This property of the 3D situation is preserved in the 2D projection.

The reconstruction of the self-motion parameters R and T as well as the distances D_i from the optic flow field encountered by the system can be defined as a minimisation problem: Given a set of image points d_i moving at (measured) velocities p_i, determine the R', T' and $|D_i'|$ minimising the differences between the measured velocities and the velocities expected from equation 2.1. This problem can be solved for a minimal number of 5 fiducial points, but the numerical error is reduced with increasing number of local velocity measurements (Koenderink, 1986).

Principal limits

The translational component of the optic flow is defined by the ratio of the translational velocity and the distances to objects in the environment (equation 2.1). This has an important consequence for the reconstruction of translational velocity and the distance profile of a scene. If both of these parameters cannot be estimated from another data source, only a relative profile can be reconstructed and absolute values can be computed from the optic flow neither for the translational velocity nor for absolute distances (Dahmen et al., 2001). If one of these parameters, either the absolute distance of one object or the absolute velocity is known or can be measured independently from other modalities, the absolute values of the other parameters can be calculated.

If the position of the fiducial points in the 3D environment can be assumed as fixed, at least the time-course of the translation velocity can be reconstructed from the optic flow. Furthermore, the time to contact with some object in the environment can be calculated from optic flow. Neuronal circuits that seem to extract this parameter from the flow were found in pigeons (Sun and Frost, 1998) and locusts (Blanchard et al., 2000; Gabbiani et al., 2001).

Realistic motion sensors usually view a limited part of the visual sphere. Rotations and translations can generate very similar local motion patterns in such a limited field of view. In figure 2.2 the boxes show a $30° \times 30°$ field of view in which the local velocities caused by the different movements are almost the same. For the reconstruction of self-motion parameters, a wide field of view therefore is a prerequisite (Dahmen et al., 1997).

The aperture problem

The first step in the reconstruction of the self-motion parameters is the measurement of the local image velocities. Regardless of the technique used for this analysis, a theoretical problem arises for the correct detection of the local motion direction, the so-called "aperture problem" (Hildreth, 1984). If a moving straight edge is viewed through a small aperture, only the motion component perpendicular to that edge can be measured. Motion along the edge is "invisible" for the local analysis. Figure 2.3 illustrates this for a linear edge viewed through an aperture and for the velocities measurable through apertures on a moving circular arc.

Detectablility

Theoretically, the projection of any visible point of the environment moves on the retina, when an observer moves. However, if a scene contains homogeneously coloured (and lighted) objects, some regions of the retinal image have no contrast, making a detection of the retinal velocity impossible.

In an environment containing objects of different distances from an observer occlusions also make the unambiguous velocity detection impossible in the retinal region containing the edges of a closer object when translational movements result in relative motion of the objects.

2.1.3 Technical approaches

The technical approaches to the exploitation of optic flow for navigation can be divided into two processing steps. First, the optic flow field has to be computed from a sequence of images. In a second step, these local velocity estimations are used to reconstruct the self-motion parameters of a moving agent.

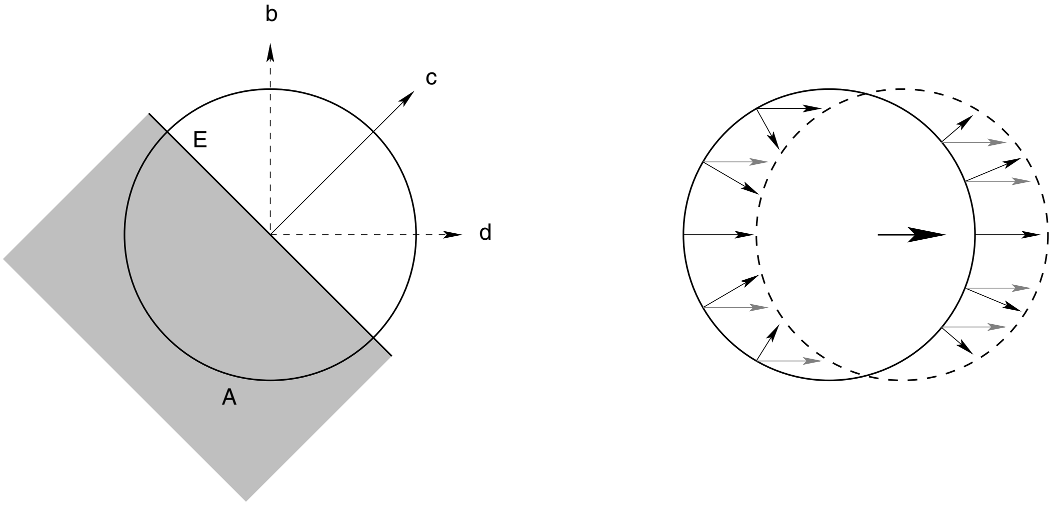

Figure 2.3: A moving straight edge (E) viewed through a small aperture (A) is shown in the left figure. Only the motion component perpendicular to the edge (c) can be measured in this situation. Other motion directions (like b,d) cannot be discriminated. For a moving circle (right figure), local velocity measurements also can give only the motion component perpendicular to the edge (true motion directions are gray, detectable motion directions black). Figure adapted from Hildreth (1984).

Computation of local velocities in technical systems

Different approaches exist for computing optic flow fields in technical systems. These approaches differ in the way they compute the estimates of the local image velocities. Besides the aperture problem, the estimation techniques need to deal with sensor noise, luminance changes, occlusions, and problems arising from partially transparent objects in the scene. All these effects complicate the robust estimation of local velocities.

Some algorithms for the optic flow estimation are based on tracking of image features over some consecutive images (e.g. Ballard and Brown, 1982). To do this, the algorithm must automatically find some image locations with properties that allow the detection and matching in subsequent frames (Chellappa and Zheng, 1995). While this approach may be robust with respect to pixel noise and can avoid the aperture problem, it cannot deliver a dense optic flow field. To generate these from the sparse local estimates, interpolation is necessary (Brady and Wang, 1992).

Other algorithms try to estimate local velocities on the basis of the spatio-temporal luminance function. Most of these algorithms, in computer science literature called "differential techniques" are based on a scheme also known as the "gradient motion detector" to biologists and psychologists. From the temporal development of the three dimensional image function $I(x, y, t)$ during motion, the so-called optic flow constraint can be derived:

$$\frac{\delta I}{\delta x} u_x + \frac{\delta I}{\delta y} u_y + \frac{\delta I}{\delta t} = 0, \tag{2.2}$$

where $u = (u_x, u_y)$ is the sought-after local image velocity. This equation relates the spatial and temporal gradients of the luminance function to the velocity. The optic flow constraint is ill-posed, because it contains two unknowns in one linear equation, which is the mathematical equivalent of the aperture problem (Bab-Hadiashar and Suter, 1998). The algorithms based on this constraint thus have to use additional constraints to overcome this problem. They can roughly be split into two groups. One approach is to use a global smoothness assumption (i.e. that the velocities and motion directions change smoothly across the visual field), the other approach assumes local constancy (i.e. that neighbouring points have similar velocities and directions of motion). These two approaches are viewed by most authors as opposing, although recently they were combined into one algorithm (Bruhn and Weickert, 2005). For a review of different algorithms see e.g. Bab-Hadiashar and Suter (1998); Barron et al. (1994); Beauchemin and Barron (1995).

All these algorithms have to deal with the problem that the estimation of the local image gradients is very sensitive to pixel noise. Thus, the optic flow fields computed from the image function usually are noisy themselves. If they are used for the estimation of self-motion parameters, it can be advantageous to thin out the flow field using some confidence measure (Dev et al., 1996; Stöffler et al., 2000; Vázques et al., 1994).

Recently, Calow et al. developed a space variant filtering method inspired by the receptive fields of motion sensitive neurons in the mammalian cortex to improve the quality of noisy optic flow estimates. They demonstrate, that this filtering process can reduce the noise in the output of a computer vision algorithm such that the reconstruction of the heading direction of a moving camera gets more stable. However, as the authors point out in Calow et al. (2004), the method may not lead to more correct estimates of the real flow field.

Reconstruction of the motion parameters

Most technical approaches try to compute the self-motion parameters from the local motion measurements by some kind of (least squares) fit of the estimated flow field to the theoretical flow field resulting from these parameters.

Koenderink and van Doorn (1987) present an iterative algorithm solving this problem. They derive a set of coupled equations, that can be solved numerically. Starting from an initial setting of the rotation and the translation, they iteratively improve the estimate by applying the equations. Dahmen et al. (1997) obtain the initial estimates by assuming zero translation when calculating the first estimate of rotation. For the initial translation estimate they assume the rotation to be zero and the fiducial points to be placed at equal distances.

Other algorithms were proposed to compute the parameters in one step. For a comparison of different approaches to solve the reconstruction of ego-motion parameters see for example Tomasi et al. (1996).

Starting from the iterative algorithm of Koenderink and van Doorn (1987), Dahmen et al. (1997, 2001) derived also a "one-shot" mechanism to estimate the self-motion parameters using a filtering approach. The filters they derived show interesting similarities to the receptive fields found in wide-field motion sensitive neurons in the fly (see also section 2.2.3). It was shown that under certain assumptions these receptive fields are indeed optimal filters for the extraction of self-motion parameters from an optic flow field (Franz and Krapp, 1998).

A filter-based estimator cannot infer the relative distances of individual fiducial points. Thus, assumptions about the typical distribution of distances must be made for the construction of the filters (Franz and Krapp, 1998). This also implies that the estimate is worse if the assumed distance statistics differ significantly from the real environment in a certain situation.

Based on distance statistics obtained from a given environmental situation, the filters can be optimised for the self-motion estimation in that surrounding. This was implemented and tested using a robotic system in an office environment (Franz and Chahl, 2002). A similar approach was also used for flight control of a simulated air vehicle (Neumann, 2004).

2.2 The blowfly visual system

The part of the blowfly visual system processing the optic flow can be divided into three modules (figure 2.4). The first module, the peripheral elements of the system located in neuropiles called retina and lamina are not strictly specialised in optic flow processing, but may also form the input stage of other parts of the visual system.

The second module, assumed to be located in the neuropile called medulla, calculates local motion information from fluctuations in the activity of neighbouring peripheral elements. In contrast to other visual information like light intensity, the velocity of an image cannot directly be represented by information obtained at only a single point in the retinal image. By measuring the intensity of a single dot of the image over time, directed image motion cannot be separated from undirected brightness changes.

Neurons of the so-called lobula complex, the third module, integrate the local motion signals spatially, coding wide field motion by their activity. Each of these integrating neurons, the so-called tangential cells, extracts different aspects of optic flow from the local motion field. Most of these neurons respond to wide-field motion in their receptive field, while others signal motion discontinuities and are thought to play a role in object detection and figure-ground segmentation (Borst and Egelhaaf, 1993b; Borst and Haag, 2002; Egelhaaf et al., 2002; Hausen and Egelhaaf, 1989). Furthermore, the tangential cells are coupled in a complex recurrent network presumably narrowing the selectivity of the response to certain optic flow patterns (Cuntz et al., 2003; Haag and Borst, 2003, 2004).

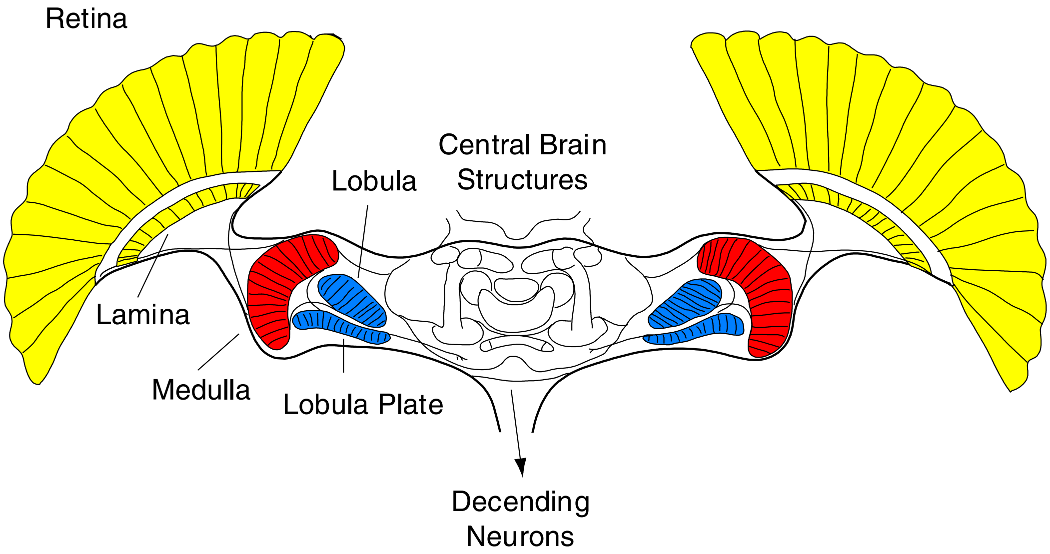

Figure 2.4: Schematic drawing of the fly brain seen in a horizontal cross section. The photoreceptor cells in the eye form the retina. The signals of these cells are propagated retinotopically (conserving spatial neighbourhood) through lamina and medulla where a column can be found for each ommatidium of the eye. The output neurons of the optic flow processing system are located in the lobula plate. The colours show the neuronal modularisation of optic flow processing: Yellow areas do non-motion-specific per-ommatidium preprocessing, in the red area local motion detection is expected to take place, and the blue areas contain spatially integrating neurons. (modified from Hausen, 1984)

An extraordinarily detailed functional model exists for the motion vision system of a fly. This model was developed based on numerous experimental findings from electro-physiological studies and observations of behaving animals. It is one goal of this thesis to elaborate this model to account for the complex responses of an important output element of the third module to natural optic flow experienced by freely flying blowflies. The following sections summarise the structure of the system is and sketch the modelling approaches for the different neuronal modules. Details of the model are discussed in chapter 4.

2.2.1 Peripheral elements

Retina

The input stage for the whole visual system is formed by the components of the eye. Insects have compound eyes that are constructed from many small ommatidia, each of which contains a lens and only a few photoreceptors (e.g. eight in the blowfly's eye). Each of these ommatidia is directed to a different point in the environment, the directions of the optical axes of neighbouring ommatidia differ by a few degrees.

The ommatidia of a blowfly form a basically hexagonal pattern. Only at a few points, this pattern shows anatomical irregularities changing the number of ommatidial rows between parts of the ommatidial lattice. The spatial resolution and the angular distance between the points in space viewed by neighbouring ommatidia changes systematically with the retinal position (Petrowitz et al., 2000).

Typically, a single ommatidium does not provide a spatially resolved image, but records the mean light intensity radiated by a single small area in the environment. Thus, the neural image is not composed of numerous small spatially resolved overlapping images as suggested by some popular illustrations, but is spatially discretised by the retina into as many discrete image elements, as ommatidia are present in the eye. Neighbouring elements of this spatially discretised image receive light from neighbouring points in the environment. This arrangement is preserved through the following stages in the processing, an architectural property called "retinotopy".

The photoreceptors contain light sensitive pigments that are photochemically split by incoming photons starting a cascade of chemical reactions that finally change the conductance of the cell's membrane and thereby cause a change in the cell's membrane potential. Thus, the photoreceptors finally encode the luminance of the incoming light by their membrane potential. In insect photoreceptors an increase in luminance is encoded by a depolarisation[1] of the photoreceptor membrane (Hardie, 1985; Laughlin, 1984).

---

[1] A resting neuron typically shows a negative in-cell polarisation of some ten millivolts. The response to an input signal is usually named relative to this resting potential. "Depolarisation" thereby denotes a more positive, "hyperpolarisation" a more negative polarisation compared to the resting potential.

Flies are equipped with 8 photoreceptors per ommatidium. Two of these photoreceptors (labelled R7 and R8) are located behind each other along the optical axis of the ommatidium. They are sensitive to different wavelengths, or colours of light. Along with this potentially colour resolving system, 6 additional photoreceptors have different optical axes (labelled R1 through R6) and form a monochromatic system which is the input for the motion detection module. For each of these photoreceptors, five photoreceptors in neighbouring ommatidia have the same optical axis. This redundant equipment with photoreceptors increases the sensitivity of the system and reduces the noise of the pooled signal under low light conditions.

Lamina

The photoreceptors R1–R6 form synapses to neurons called large monopolar cells (LMCs) in the first visual neuropile, the lamina. The lamina contains a column of neurons for each ommatidium in the retina. Each lamina column contains differently responding LMCs numbered successively.

In a circuit called "neural superposition" the information of photoreceptors viewing the same point in space are pooled in one lamina column (figure 2.5). As a result, a one-to-one relation of ommatidia on the eye's surface and the elements of the neural image in the lamina is created. Spatial neighbourhood among the input channels is conserved, the lamina columns are fed by photoreceptor inputs retinotopically.

It is still an open question, which of the lamina elements form the input to the local motion detectors. Some authors discuss separate on-off channels as the input to the motion detection system (Douglass and Strausfeld, 2001). Candidates for these cells are the LMCs L3 and L4 of the lamina (Jansonius and van Hateren, 1991, 1993)).

The majority of authors however assumes the LMCs L1 and L2 to be the input elements of the local motion detection system (for discussion see Egelhaaf and Borst, 1993). A depolarisation in the photoreceptors R1–R6 causes these LMCs to hyperpolarise, the "sign" of the neural response to light is reversed. These LMCs react to a step of light intensity with a short transient response component, forming a kind of temporal high-pass filter (figure 2.6). While the response of a perfect high pass filter to a step input would decline to zero after this initial peak, the steady state response of an L1/L2 LMC also encodes the luminance level at least in the dark-adapted eye (Juusola et al., 1996).

For the model presented in chapter 4, L1 and L2 are assumed to be the relevant input units, when LMCs are mentioned below, the LMCs L1 and L2 are referred to.

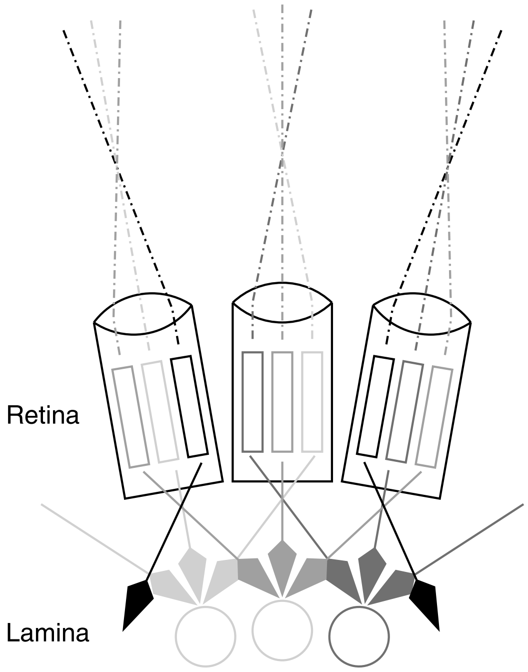

Figure 2.5: Schematic circuitry of neural superposition. The signals of all photoreceptors in neighbouring ommatidia that receive parallel incoming light from a given light source (e.g. blue rays) are pooled in a single lamina column (blue circle). The spatial neighbourhood of the light directions and photoreceptors is conserved at the level of the lamina (retinotopical projection).

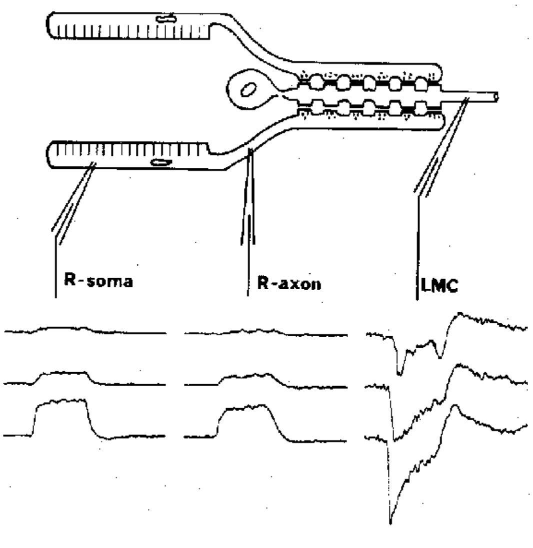

Figure 2.6: Responses of a photoreceptor and a large monopolar cell (LMC) to luminance steps at different luminance levels. The signals of the photoreceptor is a low pass filtered version of the light signal. The LMC response shows high pass characteristics, but a low gain DC component is transfered, too. The sign of the signal is reversed between Photoreceptor and LMC. Figure taken from Laughlin (1984).

2.2.2 Local elementary motion detection

The neural circuitry underlying elementary motion detection is still unknown. The second visual neuropile, the medulla, is most likely the site where these circuits are located. The cells in this region of the brain are known anatomically, but only very few studies on their physiology exist (Douglass and Strausfeld, 2001).

Based on behavioural experiments with the beetle *Chlorophanus* Hassenstein and Reichardt proposed an algorithmic model of the mechanism of local motion detection in insects (Hassenstein and Reichardt, 1956). Originally proposed in the 1950s, the model is still used in a very similar form and is probably the most successful cybernetical model at all.

This model, the so-called correlation motion detector[2], codes motion information by correlating the temporal signal of one input channel with the time-shifted signal of a neighbouring channel. The signals of one input channel are compared with the delayed signals of a neighbouring channel via multiplication. The time shifting is usually achieved by a linear temporal low-pass filter. Such a circuit is direction selective but responds to both motion and global luminance changes (flicker). To make the circuit insensitive to flicker, the multiplication output is subtracted from that of a mirror symmetrical circuit.

In its original formulation the model was composed of linear temporal filters and a multiplication stage (figure 2.7). In more recent publications the model is usually simplified by removing most of the linear filters proposed in the original publications. A version reduced to the functionally essential components is shown in figure 2.8.

One key feature of this motion detection scheme is that, while it signals the direction of motion very accurately, it does not code image velocity unambiguously. The response of the detector is ambiguous in various ways. With increasing velocity, the response reaches an optimum and declines afterwards. Stimulus parameters unrelated to velocity, such as spatial wavelength composition and contrast of the moving pattern, acceleration and higher derivatives of the velocity, change the level of reaction, too. This makes it practically impossible to reconstruct the image velocity from the detector's reaction. Nevertheless, all these ambiguities can also be found in the behavioural responses of animals and in the signals recorded from motion sensitive neurons (for review see Egelhaaf and Borst, 1993).

---

[2] In the literature, the correlation motion detector is sometimes called "Reichardt detector", referring to one of its inventors.

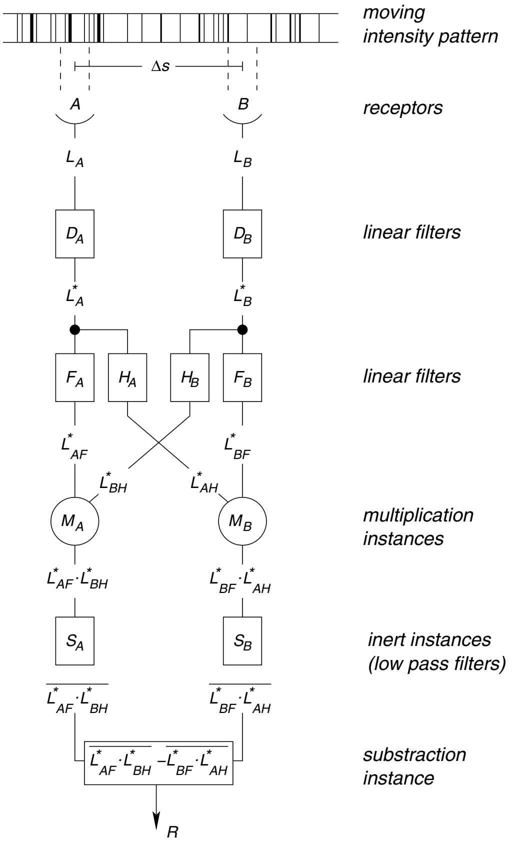

Figure 2.7: Generalised elementary structure of the original correlation motion detection model. The model is composed from linear filters (D, F, H, and S) and a multiplication. Note that the model is composed of two mirror symmetrical subunits. (Redrawn from Reichardt and Varjú, 1959)

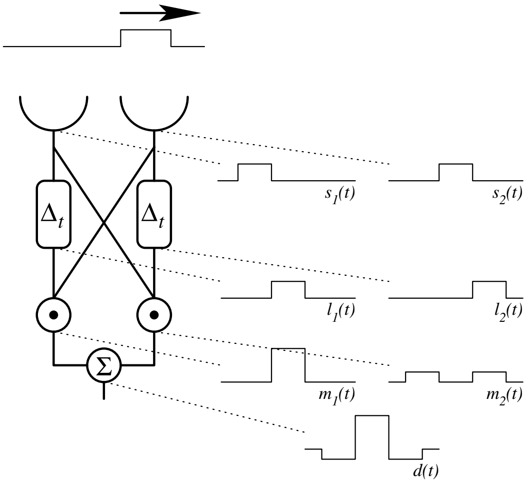

Figure 2.8: Schematic drawing of a simple version of the correlation detector. A motion signal is computed from the signal $s_1(t)$ of one input channel and the delayed signal of a neighbouring channel $l_2(t) = s_2(t - \Delta_t)$ by multiplication $m_1(t) = s_2(t)l_1(t)$. To get a detector output that is insensitive to background flicker, the signals of two mirror symmetrical circuits are subtracted $d(t) = m_1(t) - m_2(t)$.

2.2.3 Tangential cells: Optic flow filters

In the third visual neuropile of the fly, the lobula plate, approximately 50 individually different neurons exist that are identifiable in each fly both anatomically and by their response profile. These cells spatially integrate the signals of local motion detectors and are subsumed as the group of "tangential cells". Each of these tangential cells is present only once in each half of the mirror symmetrically organised visual system.

Different subgroups of these cells can be distinguished by the response mode of the cells and their spatial integration properties. Some cells respond specifically to local irregularities in the optic flow, signalling the presence of small moving objects. Other elements integrate local motion estimates of large areas of the visual field, responding best to wide-field motion caused by ego-motion of the animal (Borst and Egelhaaf, 1993b; Borst and Haag, 2002; Egelhaaf et al., 2002; Hausen and Egelhaaf, 1989). This latter group can be subdivided into cells that are presynaptic to other tangential cells and elements that are most likely output elements of the motion vision system. These cells show signals that are superpositions of graded polarisation changes and action potentials of variable amplitude (Haag et al., 1997; Hausen, 1982a,b)).

The group of output neurons contains 13 individually characterised cells for each eye or visual lobe. Three of them, the so-called HS-cells respond to horizontal motion. They are distinguished by an appended letter that denotes the position of the receptive field: HSN (north) responds to horizontal motion in the dorsal[3], the HSS (south) in the ventral and the HSE (equatorial) in the fronto-lateral field of view (Hausen, 1982a,b).

The ten VS-cells respond predominantly to vertical downward motion in different portions of the visual field. These cells are distinguished by appending numbers, counting the cells by the equatorial position of their receptive field from anterior to posterior (Hengstenberg, 1982; Hengstenberg et al., 1982). Across the receptive field of these cells both the local sensitivity to motion and the local orientation[4] of the motion detectors are changing (Krapp et al., 1998).

The receptive fields of the VS-cells look very similar to velocity fields caused by self-rotation of the animal, if the local preferred directions within their receptive fields are plotted in a cylindrical plot (Krapp et al., 1998, 2001). This led to the conclusion, that these cells act as rotation detectors. Nevertheless they react not very selectively to rotations individually and must be combined by a subtraction of the particular opposing neuron in the other hemisphere to create elective

---

[3] To describe the position of the receptive field of a neuron independently from the orientation of the animal, it is useful to adopt some anatomical terms: "Dorsal" denotes the back and "ventral" the belly, "anterior" the head and "posterior" the tail end and "lateral" refers to the sides of the animal.

[4] In the literature this local orientation is often called the "local preferred direction".

rotational sensors (Karmeier et al., 2003, 2005). While self-rotation about a given axis may be the best, or "matched" stimulus for a neuron, the same neuron is also strongly excited by optic flow generated by translation. The VS1-cell for example shows a receptive field that is similar to the velocity field caused by rotation of the animal about the horizontal short axis of the body (pitch), but is also driven to depolarised membrane potentials by the optic flow experienced during lift translation.

2.3 Blowfly behaviour

The behaviour of blowflies was closely investigated in the context of motion vision. The small size of the animals allows investigating the behaviour in the laboratory. In different studies, the animals were analysed in relatively unconstrained behavioural situations. For example flies were video recorded while the animals walked freely in cylindrical setups (Kern et al., 2001a,b)) or flew in flight tunnels (Kern et al., 2000). In other experiments, the fly carried small copper coils that could be located within a alternating magnetic field while flying in a cubic cage (Schilstra and van Hateren, 1999; van Hateren and Schilstra, 1999). Recently, high speed video equipment was used to record the trajectories of flies flying outdoors (Boeddeker et al., 2005).

In contrast to these relatively unrestrained situations, fly behaviour was also analysed in experiments where the animal was in a fixed position. For this purpose, flies were glued with wax to the axis of a device measuring the forces the fly produces by flapping their wings stationary (Götz, 1983). These forces can be recorded and analysed in an open-loop fashion, or can be used to control the stimulus (Kimmerle and Egelhaaf, 2000; Kimmerle et al., 1997). In these simulated closed-loop experiments flies are for example able to compensate global motion or to fixate objects (Reichardt and Poggio, 1976; Warzecha and Egelhaaf, 1996).

Using these techniques, the walking and flight behaviour of the blowfly was analysed and described. Some of the results are summarised in the following.

2.3.1 Optomotor response

If an insect is rotated about the vertical axis (yaw) by external forces, it responds with an active compensatory rotation into the opposite direction. The quantitative analysis of this behaviour, often interpreted to serve the stability of a straight walk or flight, was the basis for the motion detection model described in section 2.2.2. The experimental paradigm of this analysis was a beetle walking on a Y-maze globe in the centre of a rotating patterned drum (see figure 2.9). Depending on the rotational direction and velocity, the beetle showed different turning preferences at the branches of the globe (Hassenstein and Reichardt, 1956).

Figure 2.9: A tethered beetle walking on a Y-maze globe. Based on experiments like this the algorithmic model for the elementary motion detection was formulated in the 1950's. (figure from Borst, 2000)

Other experimental paradigms reveal the same behaviour. Flies walking inside of a rotating striped cylinder show a preference for turns following the motion of the pattern (Götz and Wenking, 1973). In stationary flight in such a cylinder, a constant torque in the direction of the motion can be measured (Götz, 1983; Reichardt and Poggio, 1976).

A behaviour similar to this so-called optomotor response of insects can be found in one or the other form almost universally throughout the animal kingdom. The eye movements of vertebrates including humans in such a situation are interpreted similarly.

A possible mechanistic explanation is the generation of the compensatory rotation on the basis of the difference in the responses of neurons sensitive to horizontal motion. This hypothesis is supported by the finding that the yaw rotation force generated by a tethered flying fly shows a similar dependence on pattern velocity as the responses of tangential neurons. Another support for the hypothesis is the finding that unilaterally blinded flies show a slight preference to turn towards the open eye. It could be shown, that this preference on average generates an optic flow pattern which causes a zero response in the output tangential neurons which are assumed to control this particular behaviour. With the other neuron not responding because their input is cut of, this leads to a zero difference signal (Kern et al., 2000).

2.3.2 Characteristics of blowfly flight

Flies show a characteristic pattern of motions in free flight behaviour. Although they are able to fly slow continuous turns while chasing targets (Boeddeker et al., 2003), they seem not to do this in normal cruising flight or in obstacle avoidance tasks. Instead, their flight trajectory is characterised by straight segments intermitted by sharp fast turns, commonly referred to as body saccades. These saccades last only for a few milliseconds, but having rotational velocities up to several thousand degrees per second, they can change the orientation of the fly by up to 90 degrees in this short time (Schilstra and van Hateren, 1999; van Hateren and Schilstra, 1999). The head is actively rotated in advance to the body movement so that these turns appear to be even shortened with respect to the gaze. In the initial phase of the turn, the head compensates for the turn which leads to a stabilisation of the prior gaze direction at the onset of the turn. The head then actively shifts to the new gaze direction, again compensating for the turn in its last phase so that the new gaze direction already is maintained before the body stops turning. This behaviour can be interpreted as an active vision strategy stabilising the gaze rotationally as much as possible (Schilstra and van Hateren, 1998b). By such a gaze stabilisation the rotational and translational components of the optic flow are largely segregated at the level of behaviour.

In blowflies, these sharp turns in body orientation and gaze are not obviously reflected in the trajectory of the body's centre of weight. Due to sideward drift after a body saccade, presumably caused by the inertia of the fly, the trajectories look relatively smooth and do not have the sharp corners that could be expected from the rapid changes in body orientation (van Hateren et al., 2005).

It is not clear so far, what triggers a body saccade. In a study analysing the saccades of *Drosophila melanogaster*[5], Tammero and Dickinson come to the conclusion that fronto-lateral image expansion triggers the saccades (Tammero and Dickinson, 2002a,b)). This can be interpreted as an avoidance of approaching objects.

When flying in a flight tunnel, blowflies avoid the situation that their gaze is parallel to their actual flight direction. This is suggested, because the fly seems to initiate a saccade as soon as the sideward drift component of the body trajectory becomes negligible (Kern, personal communication).

The saccadic flight mode of blowflies may be of advantage for the optic flow analysis by separating of the rotational and the translational optic flow component on a behavioural basis. Simulation experiments supporting this hypothesis are discussed in chapter 5.

---

[5] *Drosophila melanogaster* is a small fruit fly.

2.3.3 Tunnel centring

Flies (or bees) flying in an elongated tunnel tend to fly in the centre of this tunnel. In an environment containing obstacles, they tend to keep roughly equal distances to these.

This behaviour can be explained by the active balancing of the optic flow experienced on the two eyes. If the animal gets closer to an object, the flow generated on the corresponding eye, gets faster due to the dependence of the translational flow component on object distance. This hypothesis is supported by the finding that the insect shifts to a more lateral position in the tunnel if one of the walls is moving itself (for a review see Srinivasan and Zhang, 2003).

2.4 Information coded in tangential cell responses

As described in section 2.2.3 the tangential cells are believed to extract parameters of self-motion from the optic flow field based on their receptive field structure (Hausen, 1982a,b; Hausen and Egelhaaf, 1989; Krapp et al., 2001). One particularly well analysed output cell of the visual system, the HSE neuron responding to visual wide-field motion is depolarised by front-to-back motion in the ipsilateral[6] visual field and hyperpolarised during motion in the reverse direction (Egelhaaf et al., 2002). Although HSE also responds to forward translation, it was concluded to specialise in encoding rotations around the vertical axis of the head (yaw) (Horstmann et al., 2000), because it receives excitatory input also from the contralateral eye during back-to-front motion via the identified H1- and H2-neurons (also form the group of tangential cells). Responses to natural optic flow, however, cast doubt on this conclusion.

Retinal image sequences a blowfly had seen in a behavioural experiment were reconstructed and used as stimuli for an electrophysiological analysis of the cell's responses to optic flow with a spatial and temporal statistics close to the natural situation. The velocity profile of yaw rotations in these stimuli reflects the blowfly's saccadic flight style (see section 2.3.2, figure 2.10). The cell briefly hyperpolarises during saccadic turns evoking null-direction motion. In contrast to expectations from responses to conventional stimuli it does not consistently depolarise, but often hyperpolarises slightly, during preferred-direction saccades (see figure 2.11).

Many of the larger depolarisations are in fact not evoked during preferred-direc-

---

The text of section 2.4 is a shortened version of the one previously published in Kern et al. (2005b).

[6] The two vertically separated mirror-symmetrical halves of the brain or the halves of the visual sphere are named with respect to an observed neuron to be "ipsilateral" (same side) or "contralateral" (opposite side).

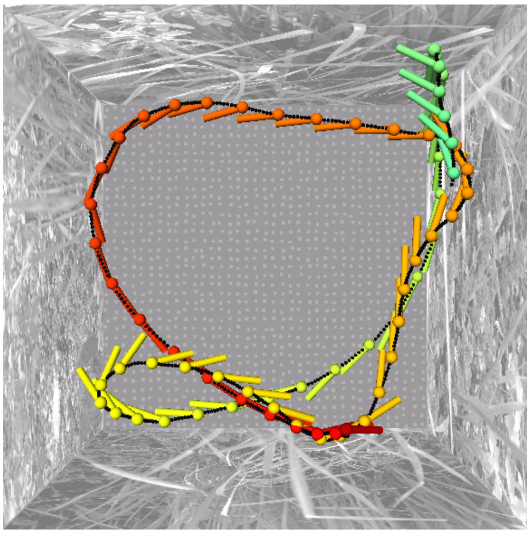

Figure 2.10: Down-view of a flight trajectory (dotted line), with head position and orientation shown every 50ms (time colour coded: start red, finish green). Figure redrawn from Kern et al. (2005b)

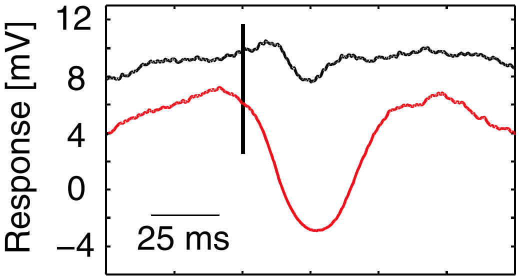

Figure 2.11: Saccade triggered averages, calculated from the mean responses of HSE for preferred-direction (black) and null-direction (red) saccades (63 different saccades). Vertical line denotes time of saccade peak velocity. Figure redrawn from Kern et al. (2005b)

tion saccades, but between saccades (positive response level before saccades in figure 2.11).

This surprising feature is not caused by the possibility that the angular velocities during saccades are too large to be perceived by the motion vision system. When the neuron is stimulated exclusively with the original rotations without any superimposed translation, pronounced depolarising response peaks during preferred-direction saccades occur. From the considerable difference between the responses plotted in figures 2.13b and 2.13c it follows that the translational optic flow component has a major impact on the neuronal response profile, even though it is much smaller than the rotational component evoked by saccades. Since between saccades blowflies keep their gaze stable apart from small-amplitude, broad-band yaw rotations (figure 2.12a, 2.14), they may gather useful information about the outside world from the translational optic flow components that dominate at low frequencies in inter-saccadic intervals. For example, knowledge of sideward translation may be used by the animal for obtaining range information in the frontal visual field through motion parallax, or in the lateral

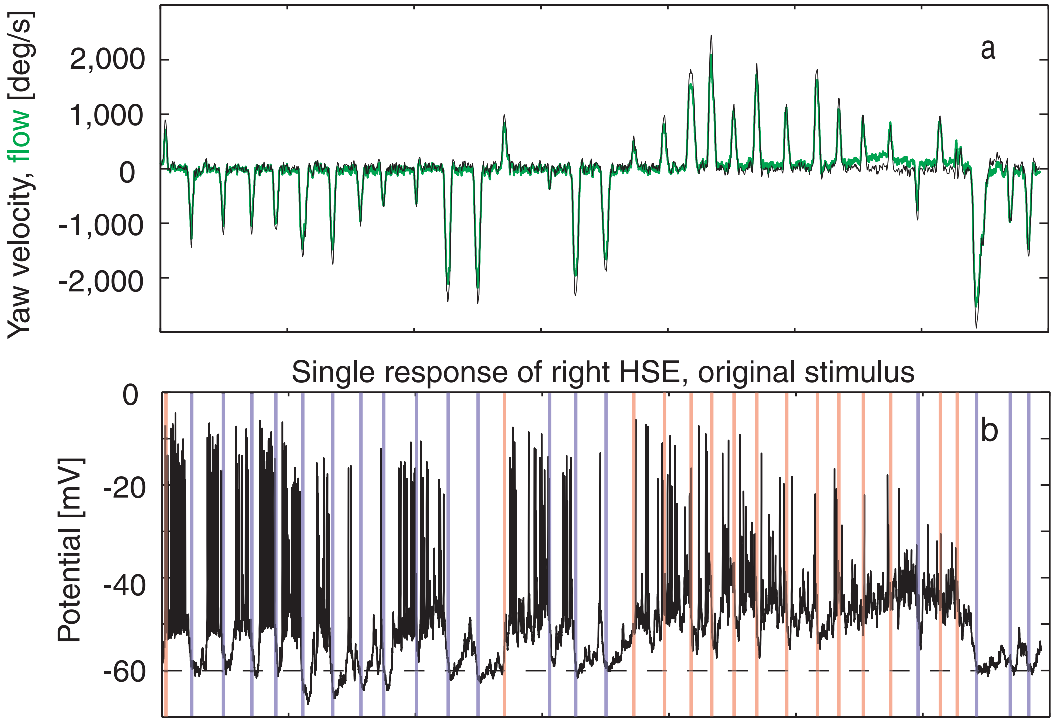

Figure 2.12: a. Head yaw velocity (black) and total optic flow (green) during the flight shown in figure 2.10. Positive velocities denote leftward turns, PD for the right HSE. b. Membrane potential of a right HSE in response to this flight. Note that the cell is mainly depolarised inbetween saccades indicated by the vertical lines. Figure redrawn from Kern et al. (2005b)

visual field by gauging image expansion there. HSE-cells may thus be tuned to provide behaviourally relevant information on the animal s self-motion especially between saccades.

To test this hypothesis, Kern et al. (Kern et al., 2005b) analysed the inter-saccadic response segments by masking the saccadic segments of stimulus and response. The similarity between the original self-motion parameters and the estimated ones based on a linear reconstruction approach is quantified by the coherence, a measure that varies between 0 (i.e. both signals are unrelated) and 1 (i.e. perfect reconstruction) (van Hateren and Snippe, 2001).

Whereas the coherence of the inter-saccadic yaw velocity and the neuronal response was significant only between approximately 20Hz and 60Hz, there was considerable coherence between sideward velocity and the neuronal responses at low frequencies (figure 2.15). Surprisingly, the coherence was much smaller for the forward velocity of the fly although HSE responds well to constant-velocity front-to-back motion of the retinal image (Hausen, 1982a,b; Horstmann et al.,

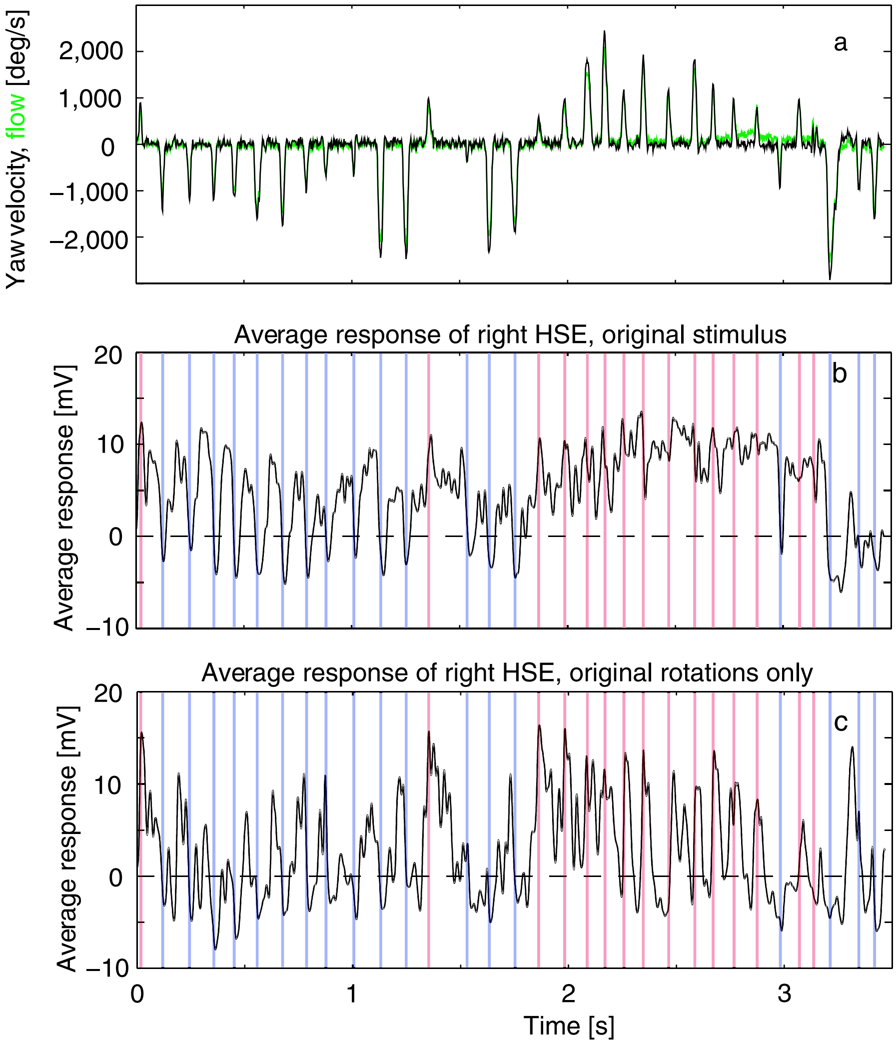

Figure 2.13: a. Head yaw velocity (black) and total optic flow (green) b. Average membrane potential of the right HSE (N=6 cells, n=17 responses). c. As b, with rotations only (position of fly fixed in centre of cage; N=6, n=11). Broken lines denote resting potential, red vertical lines indicate peak times of preferred-direction saccades, magenta lines those of the null-direction saccades. Figure redrawn from Kern et al. (2005b)

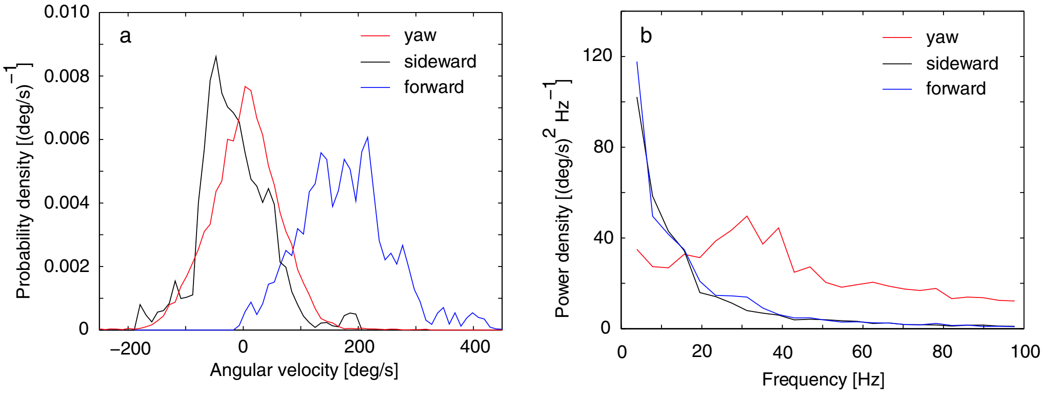

Figure 2.14: Properties of the inter-saccadic stimulus for the trajectories. a. Probability density function of yaw velocity (red), sideward (black), and forward (blue) velocity. Forward is parallel to the frontal axis of the fly's head, sideward is perpendicular to the head's plane of symmetry. Sideward and forward velocities were converted to angular velocities by multiplying by the nearness (= inverse distance) averaged over the trajectories and over the receptive fields of the neurons. b. Power spectra of yaw velocity (red), sideward (black), and forward (blue) angular velocity. Figure redrawn from Kern et al. (2005b)

2000). The coherence with the other self-motion parameters (upward velocity, pitch and roll) was negligible. It can be concluded from these results that HSE might make use of the difference in frequency content of rotations and translations (figure 2.14b) to provide information on both optic flow components in adjacent frequency bands (figure 2.15). This is possible because the inter-saccadic yaw velocities are smaller by an order of magnitude than during saccades (compare figures 2.12a and 2.14a). Hence, the saccadic gaze strategy may be viewed as a specialisation that enables the extraction of translatory optic flow amidst rotatory optic flow that would otherwise dominate the response if smooth yaw-rotations were used exclusively for steering.

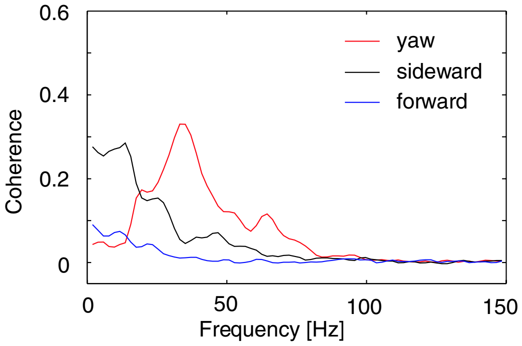

Figure 2.15: Average Coherence of yaw velocity (red), sideward (black), and forward (blue) velocity with HSE response, inter-saccadic parts of stimulus and response only. Figure redrawn from Kern et al. (2005b)

By combining the responses of the HSE-cells from both halves of the brain, the specificity of the inter-saccadic responses to the translational optic flow components can be enhanced. The summation of the responses almost exclusively signifies forward velocity (figure 2.16a), whereas the difference between the responses almost exclusively signifies the sideward and yaw velocities (figure 2.16b). The latter signals can be separated by low-pass and band-pass filtering, respectively. It is not known whether the blowfly actually uses such a processing scheme, but it is clear that the information on yaw, forward, and sideward velocity can be extracted by simple operations that can also be interpreted in neuronal terms.

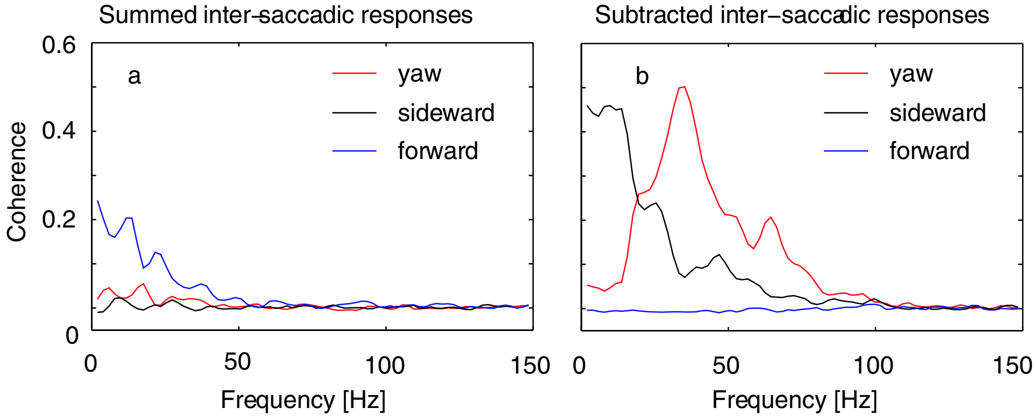

Figure 2.16: Coherence of stimulus parameters with combined HSE responses, inter-saccadic parts of stimulus and response only. a. Average coherence of yaw (red), sideward (black) and forward (blue) velocity with the summed responses of right and left HSE (N=5). b. As a, for the subtracted responses of right and left HSE. Figure redrawn from Kern et al. (2005b)

Since translational optic flow depends on the distance of the animal to objects in its environment (see section 2.1), the dependence of the neuronal responses on translation velocity is likely to reflect the spatial relation of the animal to its surroundings. This prediction is supported by experiments in which the optic flow of a given flight trajectory was tested not only for the original flight arena but also for virtual flight arenas of increasingly larger size (Kern et al. (2005b)).

Although the cell experiences the largest optic flow during saccades, it may encode behaviourally relevant information especially between saccades. Since between saccades blowflies keep their gaze stable apart from small, broad-band yaw rotations, they may gather useful information about the outside world from the translational optic flow components that dominate at low frequencies in inter-saccadic intervals. Indeed, between saccades neuronal signals provide rich information about the spatial relation of the animal to its surroundings.

A possible approach to test these hypotheses for sustainability is to analyse hypothetical control schemes based on HSE responses in a closed loop simulation.

Some initial results of such simulation experiments are shown in chapter 5.

2.5 Fly inspired robots

The promising research on the fly's optic flow processing inspired several researchers to implement robot systems that adopt part of the mechanisms studied in the fly. These systems show that the bionic[7] application of the optic flow processing strategy of the fly nervous system can be advantageous to mobile robots. While most of these robots are not intended to be a model of the fly, they provide evidence that the functional hypotheses drawn from neuroscience are sustainable.

Common to the existing systems is a mismatch to the fly in respect to the dynamics of the movements. Most fly inspired robots are classical mobile robots using the differential force generated by two wheels for steering and driving. Most of these system do not claim to be models for the flight behaviour of insects, but are engineering applications of the principles discovered in flies.

The following sections describe several of the fly inspired robots. This overview is not meant to be complete.

2.5.1 Franceschini

One of the first robots implementing a navigational system inspired by optic flow processing of the fly is the robot built by Franceschini and coworkers in the early '90s (Franceschini et al., 1992). This robot was equipped with a segmented visual system, implementing the basic properties of the blowfly elementary motion detection in discrete analog hardware. Based on this motion detection system, the robot was able to steer through a cluttered environment and avoid obstacles while approaching a target defined by a beacon.

This system implements two sets of motion detectors, one system viewing the side and a second system monitoring the frontal part of the visual field. The inter-detector angles are varied with the position of the input elements in a sinusoidal fashion compensating for the properties of a forward translational flow field.

While it was not a primary goal of the project to mimic insect behaviour in detail, the system uses a special saccadic strategy to separate the rotational from translational components of the optic flow. The system was programmed to move straight forward for a portion of time, integrating the received motion signals

---

[7] This term is formed from the words BIOlogy an techNIC and denotes adaptation of design principals from biology in technical systems.

and than turn away from so-detected obstacles in a sharp turn. This movement strategy is similar to the saccadic gaze strategy observed in blowfly behaviour.

2.5.2 Coombs

Roberts and Coombs (1993) built a robot using motion information from two peripheral views to implement the centring behaviour observed in bees and flies. This robot moves in the centre of a tunnel and avoids obstacles by balancing the flow experienced on both sides.

The basic idea for the system is inspired by insect neuroethology, but the implementation is far from being a model for the insect neuronal system. The system uses so-called gradient motion detectors showing properties different from the properties of biological motion detection. The local motion signals are not spatially integrated but the maximum velocity is extracted from the motion image.

Nevertheless, this system also uses compensatory camera rotations to behaviourally separate the rotational and the translational components of the optic flow.

2.5.3 Harrison and Webb

Harrison and Koch (1999) designed an analog VLSI[8] implementation of the blowfly motion detection system. The chip integrates the entire motion pathway from an adaptive photoreception stage to the spatial integration of correlation-type motion detectors. This chip was tested in an electrophysiologist setup showing similar responses to rotating stripe patterns as the horizontal tangential cells of a fly (Harrison and Koch, 2000).

The chip was used as an "eye" of several robots. It served to implement an optomotor-balance behaviour which was able to correct for systematic biases in the robot's motor system. In an integration with auditory and olfactory systems, the chip was tested also in a multi-modal robot system (Webb and Harrison, 2000; Webb et al., 2004). In this system, a looming sensor derived from the optomotor-chip was used to implement frontal object avoidance.

2.5.4 Huber

Huber et al. (1999) implemented a simple one-dimensional model of the fly motion vision system and used the spatially integrated horizontal image motion signals to control small robots in simulation and desktop experiments. The system

---

[8] "V"ery "L"arge "S"cale "I"ntegration refers to a class of (analog) microchips.

was shown to have the capability of an optomotor stabilisation of the image. Furthermore, the system showed fixation behaviour in the presence of an isolated black stripe similar to a behaviour also observed in walking flies.

2.5.5 Neumann

Neumann implemented a fly inspired flight control system for an autonomous helicopter tested in a simulation environment (Neumann, 2004). The system used optic flow information for optomotor heading stabilisation, altitude control and obstacle avoidance. While he used correlation-type motion detectors for local motion detection and created wide-field optic flow filters inspired by fly tangential cells, the spatial layout of these filters were optimised for the different tasks. The sensor detecting unintended yaw rotations (e.g. induced by control noise or wind) is an equatorial ring of horizontal motion detectors. The filter signalling ground proximity is formed by detectors oriented along the local movement directions of an expansion flow field in the downward half-sphere. Obstacle detection is accomplished by fronto-laterally oriented expansion detectors with a single focus of expansion frontal to the system.

Roll and pitch of the system are controlled visually on the basis of statical images, a system which is inspired by the dorsal light reflex of insects stabilising their upright posture in a natural environment, too.

2.5.6 Reiser

Based on the experimental results of previous studies on flight behaviour of *Drosophila melanogaster* (Tammero and Dickinson, 2002a,b), Reiser and Dickinson implemented a saccadic wall avoiding system on a robotic arm positioning a camera in a cylindrical environment (Reiser and Dickinson, 2003). This system uses optic flow analysed by fronto-lateral expansion detectors with one focus of expansion on each side. The saccades the system initiates to avoid the walls of the arena are triggered by a threshold operation on the signals of these expansion detectors. The direction of the saccade is chosen to turn away from the side on which the threshold was hit, the angular amplitude of the saccades is not determined by the optic flow, but is drawn from a random distribution. With this approach, the camera can travel inside the cylinder, visually avoiding the walls.

2.6 Summary

This chapter introduced the basic concepts and scientific results that form the basement of the developments described in the remaining parts of the thesis.

Starting from the definition of "optic flow" and the discussion on the information coded in these retinal image movements, the neuronal apparatus in the fly brain extracting the behaviourally relevant signals was sketched. The saccadic turns observed in the blowfly flight behaviour are responsible for the very specific dynamics of the stimuli the system is confronted to in free flight. Recent results on the information extracted from such behaviourally generated stimuli by the output neurons of this system leads to the hypothesis that depth information may be coded in the signals of the HSE-neurons previously assmued to primarily serve as rotation detectors. A very brief summary about existing technical applications of this approach to optic flow processing were given in the last part of the chapter.

The following chapter describes tools for the further analysis of the neuronal system outlined above. The experimental results on the response of tangential cells to naturalistic image sequences cited in section 2.4 were already derived aided by the FliMax (see section 3.3). These same results represent the benchmark for the calibration of a quantitative simulation model for the sensory system (see chapter 4). This model implements the optic flow processing neuronal system sketched above. The simulated neuronal responses of this model then form the input variables for the closed-loop simulation of a hypothetical control system discussed in chapter 5.

3 Technical tools for the analysis of fly visual navigation

This chapter describes technical tools needed for the analysis of the visual navigation system of flies using behaviourally generated optic flow stimuli. Such stimuli are formed by the image sequence a fly has seen during a free-flight behavioural experiment. These sequences can be reconstructed, if the flight trajectory of the fly is known quantitatively. The retinal image sequence can be generated by computer graphics from this trajectory, if a detailed 3D-model of the experimental setup exists. Otherwise a panoramic imaging device can be used to record the retinal images in the original environment in which the flight was recorded (Boeddeker et al., 2005).

The first step for the creation of such stimuli in both cases is the quantitative analysis of the animal's behaviour. Section 3.1 describes "Flytrace", an image processing system designed for the quantitative reconstruction of 2D trajectories from video sequences recorded in behavioural experiments with walking and flying blowflies. In the following, the term "trajectory" comprises both the time-dependent position of the fly and the orientation of its body axis. Based on two of these 2D trajectories obtained from different viewing directions and the knowledge of the cameras' positions and viewing directions, the 3D-trajectory of the fly can be reconstructed.

Once the trajectory of an animal is known, the retinal images can be reconstructed from a 3D-model of the experimental setup by computer graphics methods. Section 3.2 describes software used to generate retinal images from the trajectory data. The reconstructed retinal images are either fed into a model of the visual pathway which is described in chapter 4 or replayed to a fly while recording the tangential cell responses to these image sequences.

Flies have almost omni-directional vision and extraordinarily fast photoreceptors demanding for a high-frequency presentation of the image sequences on an almost panoramical display. Section 3.3 introduces "FliMax", a specifically designed display device for the replay of these image sequences to a fly in an electro-physiological replay experiment.

To evaluate the further processing of this sensory information by the fly, the sensory-motor coupling must be analysed. This can be done with an input-output analysis, if the responses of sensory neurons and the motor output can be recorded for the same stimuli. The motor output of a flying fly is a complex motion pattern of the flapping wings. Two parameters of this pattern, the wingbeat amplitude and frequency for the two wings can be recorded with a setup described in section 3.4.

A more indirect approach to analyse the sensory-motor coupling is the attempt to mimic the behaviour of a fly in a closed loop simulation of a virtual agent using the model of the sensory neurons described in chapter 4 as its input. The software needed for such experiments is described in section 3.5, the results are presented in chapter 5.

3.1 Recording the flies behaviour

For the creation of behaviourally generated stimuli, the trajectory of a walking or flying animal must be reconstructed. Two principally different approaches have been taken to record such trajectories.

The animals can be equipped with small search coils that register time-varying magnetic fields generated by a set of field coils surrounding the cage in which the fly is flying (figure 3.1). Such a technique has been established for the blowfly by Schilstra and van Hateren (1998a). A disturbance of the fly's behaviour by the additional load of the coils and the attached cables could not be observed, but cannot be excluded completely.

This tracking with miniature coils is only applicable in relatively small setups. Also, the setup must not have too many obstacles because of the wire connecting the search coils with the recording equipment. On the other hand the fly's position and orientation in space can be recorded with high temporal and spatial resolution using search coils. Also the tracking of the fly's head is currently only possible using coils. The flight data used for the calibration of the model described in chapter 4 was generated in this setup.

A different approach is to record the flight with cameras and reconstruct the trajectory from the recorded image sequences. With the camera approach the flies can be observed in almost arbitrary environments. Although the space viewed by the cameras is also limited, they can be placed in an open and even outdoors environment (Boeddeker et al., 2005). Obstacles cause problems in this approach only if they disturb the view of a camera on the fly. Another advantage of the approach is that the animals do not need to be prepared in any way.

The positions of the fly can be reconstructed from image sequences at least as precisely as with the coil technique (Boeddeker et al., 2003; Schilstra and van Hateren, 1998a). The reconstruction of the yaw- and pitch-orientation of the body from images are possible, but the achievable precision depends on the ori-

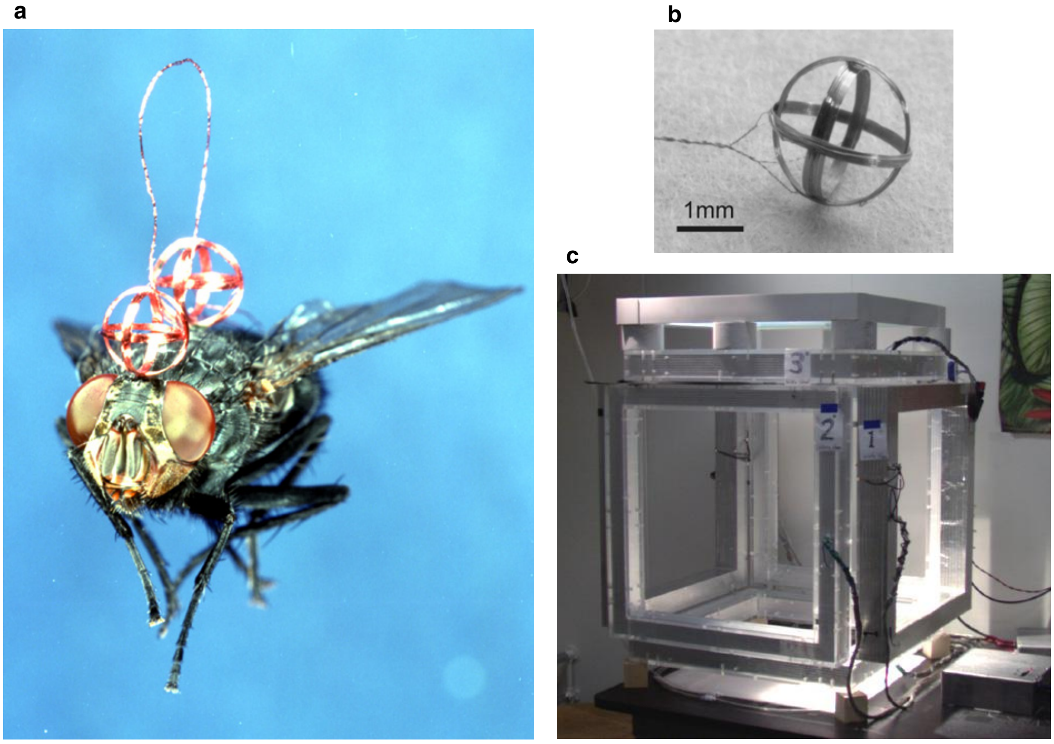

Figure 3.1: The setup for magnetic tracking of flying blowflies. The flies carry small sets of three orthogonally arranged coils (b) on their head an thorax (a) while flying between six field coils (c) generating a time-varying magnetic fields. The induced currents are measured by a computer via thin copper wires. The position and orientation of the fly can be reconstructed from these signals at high temporal and spatial resolution. (Photos: J. H. van Hateren, http://hlab.phys.rug.nl/)

entation of the fly with respect to the camera's viewing direction. If the camera, for example, records the fly in side-view, the reconstruction of the pitch angle is much more precise than if the fly is flying towards the camera. The reconstruction of the roll-orientation cannot be estimated robustly because even the optimal back-view of a flying fly is almost circular if the wings cannot be detected in the image. The orientation of the head cannot be resolved in an image showing a significant section of the environment without actively tracking the fly with pan/tilt cameras (see section 6.1.2).

The trajectory is defined by an $N \times 6$ matrix for N time steps. For each time step the 3 Cartesian coordinates and 3 angles defining the orientation of the fly in space have to be computed.

The basis of the reconstruction are 2D image sequences recorded either by standard video cameras or special high speed digital cameras. To reconstruct the 3D data, at least two different synchronously recorded views are necessary. From each of these image sequences the individual 2D positions and directions of the animals are extracted as described in the following section 3.1.1. In a second reconstruction step the 2D information is integrated to 3D-positions and directions, while the perspective distortions of the images have to be considered. This second step is described in section 3.1.2.

3.1.1 2D image processing

The 2D image processing is done by a digital image processing system specifically designed for the detection of small moving objects in front of a stationary background. Figure 3.2 gives an overview of the image processing steps and an example of the images to be processed by the system.

All algorithms used for 2D image processing are from the standard toolbox of digital image processing as described in text books like Jähne (1997) or Sonka et al. (1999).

Computer-aid in favour of elaborated automatics

In his diploma thesis Lutterklas (1996) described a system for analysing the 2D image data. For the local analysis of the single images his system already used most of the methods detailed below. Based on the local analysis the system tried to assign each detected region to the trajectory of an individual fly automatically. This was done by constructing a graph of possible trajectories that was assessed globally to find the most plausible ones.

For the experimental everyday work this system was of only limited use, because inevitable detection failures could blow up the graph so that the system's performance got unacceptable or ruined the result completely. His original implementation also did not allow the user to correct the detection failures in a convenient way prior to the construction of the graph.

One major design goal for a new implementation and extensions of the original system was therefore to provide the user with automatic processing up to a helpful degree. Automatic processing needed to be interruptable and restartable at any point to ease the correction of errors early in the process. Automatics should be an aid for the user of the system and should not prohibit manual intervention.

During re-implementation and testing it turned out that it is possible in most cases to create correct trajectories with pure local processing of adjacent images and an acceptable amount of user interaction. Therefore the global assessment of possible trajectories was not re-implemented in the currently used system.

Image sources

Two different sources of image sequences have to be handled by the software.

Until recently, the behavioural data have been recorded with standard black and white video equipment (Boeddeker et al., 2003; Kern et al., 2000, 2001a). These cameras provide the images in an interlaced PAL video signal that is digitised using a black and white frame grabber (Data Translation DT3155) from analog video tape after the experiments are finished. The shutters of the two cameras are synchronised and the video timer signal inserted in both camera images makes the manual identification of matching frames possible. The images are stored in sequentially numbered TIFF files by the grabber software.

As a result of the interlacing the effective temporal resolution of these sequences is 50 Hz although only 25 full frames are transfered to the hardware. Therefore the software must treat the two fields of each frame as images for adjacent time steps. The drawback of this procedure is, that the pixels in these fields have a 1:2 aspect ratio. This can be corrected by repeating each line of the image twice and doing all processing on this enlarged image, but this correction would be gained by a significant loss of performance, since the corrected images are doubled in size and all per-pixel processing is done redundantly on the data. Furthermore, operations on neighbouring pixels are distorted in the vertical direction by the repetition of scan lines. When the processing is done on the raw fields, the aspect ratio has to be respected at all stages of processing. In the current implementation the software uses the fields for all internal processing, doing the doubling of lines only for displaying purposes.

A more up-to-date method of image acquisition is to record the data using digital full frame cameras. The newer results shown below are recorded with two digital full frame cameras (Redlake MotionPro) providing 500 black and white frames per second at a resolution of 1024×1024 pixels. While these images are of much better quality with respect to resolution and pixel noise compared to those obtained from PAL videotape, the sheer amount of image data[1] provided by this setup poses a strong urge for further optimisation of the processing.

Regardless of the source the images used for the processing are gray level images digitised at a intensity resolution of 8 Bit per pixel.

For the digital high speed cameras, the image sequences are stored in an uncompressed AVI format by the camera software. Compression with a standard algorithm for image sequences is provided by the software, but this feature is not used in order to avoid artifacts introduced by lossy compression.

Both cameras are controlled by a common computer ensuring the synchronous recording of the sequences and common starting times for the two sequences

---

[1] The two cameras record 1000MBytes raw image data each second.

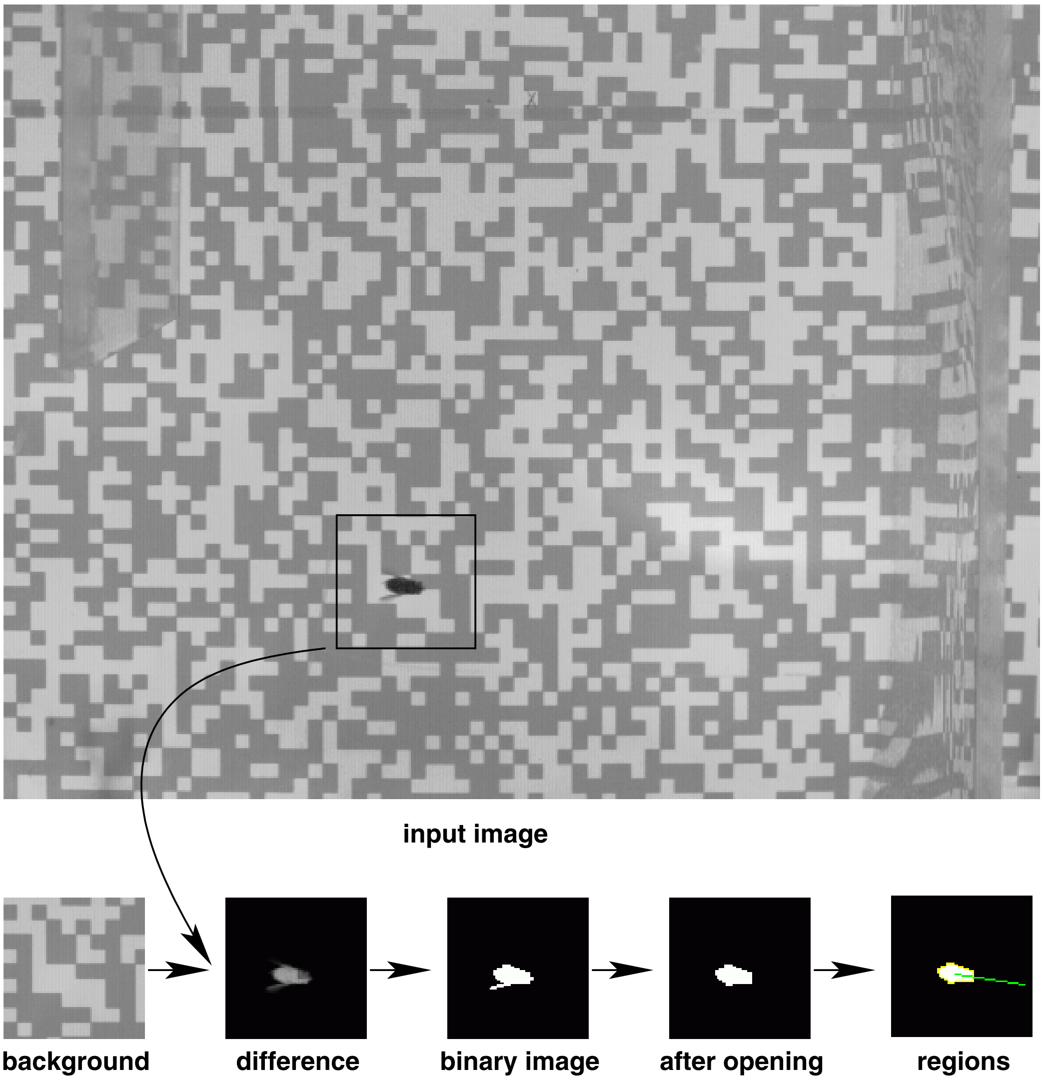

Figure 3.2: Example for the image processing steps. On top a large part of the input image (a fly flying in a flight tunnel) is shown as seen from above. Below the individual processing results are shown. From left to right: The background image calculated as the mean of 10 input images, the difference image, the binarised version of the difference image, the binary image preprocessed by the opening method and the outline of the region and its orientation indicated by green lines.

recorded in an experiment.

Object-background discrimination

In the experimental setups the cameras are mounted at fixed positions. Therefore it can be assumed that the background is an invariant image component throughout a sequence. This eases the discrimination of background and object, the object can be extracted by simply subtracting the mostly invariant background image.

Background image

The background image can easily be derived from the sequence by pixel wise calculation of the mean of a representative sample of single images.

Depending on the individual experiment it can be useful to limit the background image calculation to a part of the sequence. For instance, if an animal sits at a fixed location for the majority of the images and flies away later, a background image calculated from the complete sequence would show the sitting animal, leading to a result where the sitting animal is detected as an additional object when the fly has started and the object undetected in the section showing the sitting fly.

The user chooses as a first step of the analysis which part of the sequence should be the basis of the background calculation and how many images should be used. The background image is then calculated as

$$I_{bg}(x,y) = \frac{1}{N}\sum_{n=0}^{N-1} I(x,y,t_{min} + n\frac{(t_{max} - t_{min})}{N})$$

Where t_{min} defines the beginning, t_{max} the end of the section, and N the number of images used. $I(x,y,t)$ is the intensity function of the complete sequence and $I_{bg}(x,y)$ is the calculated background image.

The user can alternatively choose to use a stored background image. Using a single frame of the empty scene is possible, but the calculation of the mean has the additional advantage that the pixel noise of the camera is reduced in the resulting background image to a large degree which causes a significant reduction of background noise in the difference images.

Difference image

For each time step t a difference image $D(x,y,t)$ is calculated from the background image and the (preprocessed) image taken at that time step:

$$D(x,y,t) = |I(x,y,t) - I_{bg}(x,y)|$$

Using the absolute value of the difference causes the object to be represented by positive values in the resulting image regardless of the polarity of the intensity difference between background and object. A white object on a black background or a black object on a white background are both represented by the same difference values. The values of the difference image thus represent the contrast between the background and the current image at each position.

Binary image

In the next step, the difference image is converted to a binary image by a thresholding operation.

$$\begin{aligned} B(x,y,t) &= 0 \quad \text{if} \quad I(x,y,t) < T \\ &= 1 \quad \text{otherwise} \end{aligned}$$

The threshold T is chosen by the user or can be calculated from a representative difference image using the following iterative algorithm (see e.g. Gonzales and Woods, 2002). This algorithm is sometimes referred to as "midpoint method" for threshold selection.

1. Set the initial threshold value to

   $$T_0 = \frac{(max(I(x,y)) - min(I(x,y)))}{2}$$

   This is a good initial value for the threshold under the assumption that the maximum intensity value lies within an object while the minimum value is from the background.

2. For each iteration step t do a binarisation using T_t and compute the mean gray level of the two segments of the image

$$\begin{aligned}\mu_t^0 &= \frac{\sum_{(i,j)|I(i,j)<T_t} I(i,j)}{n_0} \\ \mu_t^1 &= \frac{\sum_{(i,j)|I(i,j)\geq T_t} I(i,j)}{n_1}\end{aligned}$$

where n_0 and n_1 are the number of elements in the segments.

3. Calculate a new threshold value

$$T_{t+1} = \frac{\mu_t^0 - \mu_t^1}{2}$$

4. Iterate Steps 2 and 3 until the new threshold is close to the previous

$$|T_{t+1} - T_t| < \epsilon$$

The parameter of this break condition should be small, but not too small to prevent oscillations. $\epsilon = 5$ lead to reasonable results.

This automatic selection of a threshold causes problems in the case that no pronounced object is present in the binarised frame. The algorithm then chooses the threshold to lie within the background noise which results in a binary image with many very small regions. This can be detected by calculating the mean intensity of the binary image, which should be $\overline{I(x,y)} \ll 0.5$ when only few small objects are segmented from the background.

Processing of the binary image

Two situations can make a further preprocessing of the binary image advantageous. If the contrast between object and background is bad or changing within the object region, frayed edges of the object may result, that add noise to the further processing steps. If the background is not completely time-invariant (for example caused by moving leaves in an outdoor environment), many small regions of background noise may appear in the difference image.

Both effects are reduced by applying a morphological operation to the binary image called “opening”. A morphological operation changes the form of regions in a pixel image. In a binary image this can be achieved by convolution with a filter mask. Two basic operations can be defined for a square mask consisting of ones Jähne (1997). The dilating operator is defined as

$$B'(x,y,t) = \bigvee_{a=-R}^{R} \bigvee_{b=-R}^{R} B(x+a, y+b, t)$$

The Dilatation sets a pixel in the resulting image to one if at least one of the original pixels beyond the mask are one. All regions in the image are extended by R pixels by application of this operation. The opposite, the eroding operator is defined as

$$B'(x,y,t) = \bigwedge_{a=-R}^{R} \bigwedge_{b=-R}^{R} B(x+a, y+b, t)$$

The erosion sets a pixel in the resulting image to one if all pixels of the original image beyond the mask are one. This operation decreases the size of each region in the image by R pixels. Regions smaller than the mask is removed completely. Thin structures of the image are removed if their width is smaller than R.

The opening operation is created by application of both operators in iteration. First all small regions are removed by erosion of the image and afterwards the original size of the remaining regions is reconstructed by dilation.

Segmentation

Using a simple recursive region growing method, the binary image is segmented:

1. Find a white pixel not yet assigned to a region in the binary image by linear search.
2. Label this pixel to be part of the new region in a second binary label image.
3. For each of the 4 neighbouring pixels (up, down, left, and right): If the pixel is white and not labelled as region, recurse to step 2

Note that by using only 4 neighbouring pixels, the algorithm has the tendency to find convex regions and to detect separate regions, if two white blobs are neighbours only via diagonally neighbouring pixels. In the top-view of a fly this can lead to the separation of the wings into individual regions. These regions are eliminated by later plausibility checks (see below). Detecting the fused region as one region (i.e. by using the neighbourhood of 8 pixels) would make the detection of the body orientation more unreliable.

Several parameters are calculated to characterise each region. The size is given by the number of pixels contained in the region. The centre of gravity is calculated as the mean of the pixel locations.

The orientation and the eccentricity of the object are calculated using a momentum based approach described in Jähne (1997) is applied. For the object region a set of moments is defined as

$$m_{p,q} = \sum_{i=1}^{n} (x_i - \langle x \rangle)^p (y_i - \langle y \rangle)^q$$

where $(\langle x \rangle, \langle y \rangle)$ is the centre of gravity of the region and n the number of pixels of the region $\langle \rangle$ brackets denote the expected value.

The second order moments ($p + q = 2$) form an inertial tensor of the region. The orientation ϕ and the eccentricity ϵ are defined as

$$\phi = \frac{1}{2} \arctan \frac{2m_{1,1}}{m_{2,0} - m_{0,2}}$$

and

$$\epsilon = \frac{(m_{2,0} - m_{0,2})^2 + 4m_{1,1}^2}{(m_{2,0} + m_{0,2})^2}$$

The angle ϕ gives the orientation of an ellipse fitted to the region. The eccentricity ϵ is a measure of the roundness of the region, varying between 1 for a line and 0 for a circular object.

The set of detected regions is pruned using different criteria, which are defined and parameterised by the user. Regions that do not match all these criteria are not processed further. Criteria are:

- A region of interest defined by a polygon. Regions must contain at least one pixel lying inside of this polygon.
- A range of expected region sizes.
- A range for the expected eccentricity.

Trajectory detection

To reconstruct the 2D-trajectories of more than one fly, the correspondence of regions in adjacent images must be detected.

For any moving object in a sequence of images sampled at a sufficiently high frame rate it can be assumed that the parameters describing corresponding regions in adjacent images do not change significantly. It is unlikely that a fly travels a large distance within a few milliseconds or turns faster than a few $1000\frac{\circ}{s}$. By using the differences between the region parameters as a cost function, it is possible to treat the correspondence search as a minimisation problem.

The cost function c_{r_1,r_2} for a pair of regions r_1 and r_2 is defined as a linear combination of changes in the regional parameters for a pair of regions.

$$c_{r_1,r_2} = \lambda_p|p(r_1) - p(r_2)| + \lambda_o|o(r_1) - o(r_2)| + \lambda_s|s(r_1) - s(r_2)| + \lambda_e|e(r_1) - e(r2)|$$

where $p(r)$ is the position, $o(r)$ the orientation, $s(r)$ the size, and $e(r)$ is the eccentricity of region r. The coefficients λ_x weight the parameter differences. These weights have to be adjusted by the user to match the plausible amounts of change in the different parameters for a certain experimental setup.

When a fly is only visible for the camera in parts of the sequence, or noise regions are generated by the 2D processing, the number of trajectories can change from frame to frame. Thus it is necessary to define costs for the appearance and the disappearance of objects. These costs are independent from the position and the region parameters. An object can disappear or appear anywhere in the image when it is occluded by some fixed object in part of the sequence.

For n trajectories detected in frame t and m objects present in frame $t+1$ many possible continuations have to be considered. Each trajectory from a set of trajectories $T_1, T_2, \ldots T_n$ and the corresponding regions $r_{T_1}, r_{T_2}, \ldots r_{T_n}$ of frame t must be continued with one of the regions $r_1, r_2, \ldots r_m$ detected in frame $t+1$ or terminated at frame t. For the first trajectory $m+1$ continuations are possible, because any of the objects in frame $t+1$ can be the successor of this trajectory or the trajectory can be terminated in frame $t+1$. For the second trajectory m continuations are possible, if the first trajectory has a successor in frame $t+1$, but if it is terminated, again $m+1$ continuations exist for the second. Thus, in the worst case, $n*(m+1)$ possible continuations must be tested. The costs of any of these continuation possibilities is the sum of the pair costs.

The worst case complexity of the search for the cost minimal continuation is $O(n^2)$, because in a typically n and m are of similar size. However, a simple search strategy can reduce the average complexity significantly.

The implementation of the search algorithm iteratively generates the possible continuations for the n trajectories in frame t. In each iteration step one partly generated continuation is extended. Only a fraction of all possible continuations is evaluated by extending only the continuation candidate that is associated with the least costs until the least costs are associated with a complete continuation.

- Calculate the costs for all possible continuations of the first trajectory to initialise a list L of partly generated continuations.

- Repeat:
    - Pick from L the continuation b currently associated with the least costs
    - If this continuation is complete, it is the one with globally least cost. b is the final result.
    - Remove b from the list L
    - Calculate the costs of all possible continuations of b and insert them into L

In the best case, if the costs for the correct continuation are lower than the costs for any other extension of the first trajectory, the complexity of this algorithm is $O(n)$. For the average case, the complexity depends on the choice of the coefficients of the cost function. A general prediction of the average complexity is therefore not possible.

3.1.2 Reconstruction of the 3D trajectory

When two cameras record the behaviour of an animal from at least two views, the trajectory of the animal can be reconstructed in all three dimensions from the 2D trajectories extracted in the image processing.

Precondition of this reconstruction is the knowledge of the camera parameters, namely the position, the viewing direction, and the viewing angle of each camera (C_1, C_2, figure 3.3). Based on this information, the positions of an animal in the camera images (P_1, P_2) gives the direction of two straight lines ($g_1 = C_1 + tR_1$, $g_2 = C_2 + uR_2$) in the 3D coordinate space. These lines should intersect in the position (F) of the fly if the position of the 2D images of the fly could be detected perfectly. Several sources of imperfections in the recording chain and in the detection of the regions in the digitised images inevitably cause a slight deviation of the lines in the real system. These imperfections are caused for example by small errors in the calibration of the camera parameters, optical distortions of the camera optics, noise in the signal path of the image or sampling of binarisation artifacts. The midpoint of the shortest distance between these lines D can be calculated by solving the following 3D set of simultaneous linear equations ($C_1 + tR_1 + D = C_2 + uR_2$) with two unknown variables t and u (Boeddeker et al., 2003).

The orientation of the fly

Having a sufficiently large volume in view of the cameras for the observation of interesting manoeuvres of the fly makes it necessary to work with images which show the fly only in a very small part of the image. Seen at the resulting

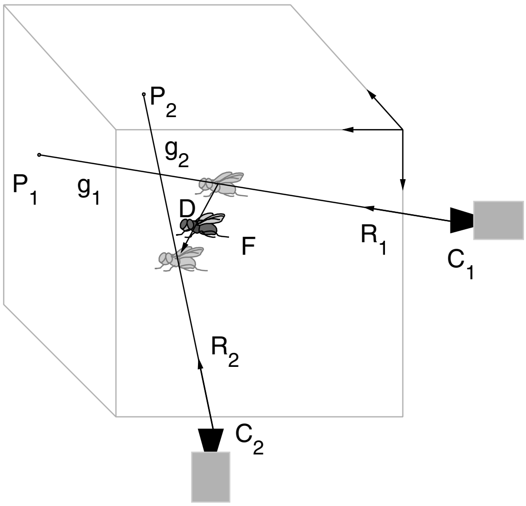

Figure 3.3: Sketch of the calculation of the fly's position F from the 2D image coordinates P_1 and P_2 and the calibrated camera positions C_1 and C_2. See text for details. Figure adapted from Boeddeker et al. (2003).

resolution, a fly appears to be a cigar shaped body. The 2D projections are more or less elongated blobs. If the fly is oriented perpendicular to the optical axis of the camera, the orientation can be reconstructed with high precision. When its main body axis has a small angle to the optical axis, the orientation of the fly cannot be safely reconstructed from the camera image, the projection of the fly's body is more or less circular.

Since flies tend to fly with a more or less horizontally oriented body, the image of a vertically oriented camera viewing the experimental setup from above or below does show the yaw orientation of the fly. However, this image cannot be used to reconstruct the pitch and the roll angle of the fly. A horizontally oriented camera recording a side view of the setup shows the pitch angle only, if the fly's flying course is almost perpendicular to the camera axis.

For the rendering of the retinal images, the yaw, pitch, and the roll angle of the head have to be reconstructed. However, what the cameras record, is the orientation of the body. The head is not discriminable in a useful resolution in images recorded by cameras viewing the whole experimental setup.

From experiments done by van Hateren and Schilstra (1999) it is known, that the roll and pitch components of the body movements are compensated by appropriate head movements almost completely in free flight. Even in so-called "banked turns", the head does almost only do a yaw rotation, while the body does change it's roll orientation by angles of up to 90°. Based on these experiments, it is justified to assume constant pitch and roll orientation of the head during flight. This makes the difficult reconstruction of roll and pitch angles dispensable.

The experiments of Schilstra and van Hateren show also that the time course of the yaw angle of the body and the head is somewhat different in fast turns. In such a turn, the head does a slightly quicker rotation than the body (van Hateren and Schilstra, 1999).

To assume that the head is perfectly aligned with the body in respect to the yaw orientation and perfectly stabilised with respect to the pitch and roll angle, introduces small errors to the reconstructed flight trajectory (For details see Kern et al., 2005a). However, to reconstruct the head orientation directly would make a higher resolution of the fly necessary. This could be done either by recording the behaviour with cameras providing a much higher spatial resolution or by real time tracking of the fly with cameras mounted on pan-tilt motors, which would make a smaller viewing angle possible (see also section 6.1.2).

3.2 Rendering

The retinal images a fly has seen in a behavioural experiment can be reconstructed from the 3D-trajectory and a virtual model of the experimental setup. The virtual construction of the experimental setup is straightforward, since the setups are designed from simple geometric forms covered with computer generated textures that can be directly reused in the virtual setup. Several computer graphics systems are available that allow the reconstruction of such setups.

3.2.1 Computer Graphics

The generation of realistic 2D images from 3D geometrical information and texture images is addressed by the field of computer graphics. The standard algorithms are part of several freely available software libraries. There are two principally different approaches to the generation of 2D images. One approach, called raytracing, is based on modelling the physics of the light rays falling into the camera. For this technique, the light rays falling into a camera are inversely traced back to their origin, a light source. While this technique yields very realistic results, the approach is relatively costly in its computational effort. Another approach is to explicitly calculate the planar perspective projection of flat polygons approximating the 3D model while keeping track of the depth of these polygons relative to the camera in order to create correct occlusions. In a second step called "shading", these projected polygons are filled with colours according to the light- and viewing direction of the 3D segments. One popular implementation of this technique is the *OpenGL* library created by SGI. The computational effort of this technique is less demanding compared to the raytracing algorithm. Furthermore, modern computer graphics hardware accelerates this approach. On top of *OpenGL*, SGI developed the high level object oriented library *Open Inventor* to facilitate the handling of complex three-dimensional scenes.

OpenInventor contains a specification of a high level scene description language.

For the reconstruction of retinal images, this language is used to describe the experimental setup geometrically and to describe the mapping of the texture images to this geometry. The resulting description file is interpreted by *OpenInventor* and transformed to bitmap views of the scene via *OpenGL*. The position and viewing direction of the virtual camera for each time-step is generated from the trajectory.

The trajectory is defined by a $N \times 6$ matrix for N time steps where the first three columns define the x, y and z coordinates of the position of the fly in the setup, the following two columns define the viewing direction of the camera. The sixth column defines the rotation angle of the camera about its optical axis.

For panoramical rendering applications it can be helpful to render the image not with a single camera pointing tangentially to the trajectory, but with a set of cameras with different viewing directions relative to the trajectory (see sections 3.2.2 and 3.3.3). Therefore a projection list defines the camera positions and viewing directions relative to the trajectory positions, the viewing angle of the camera, the size of the rendered image and a filename for the definition of a subsampling grit. Figure 3.4 illustrates the data flow in the renderer.

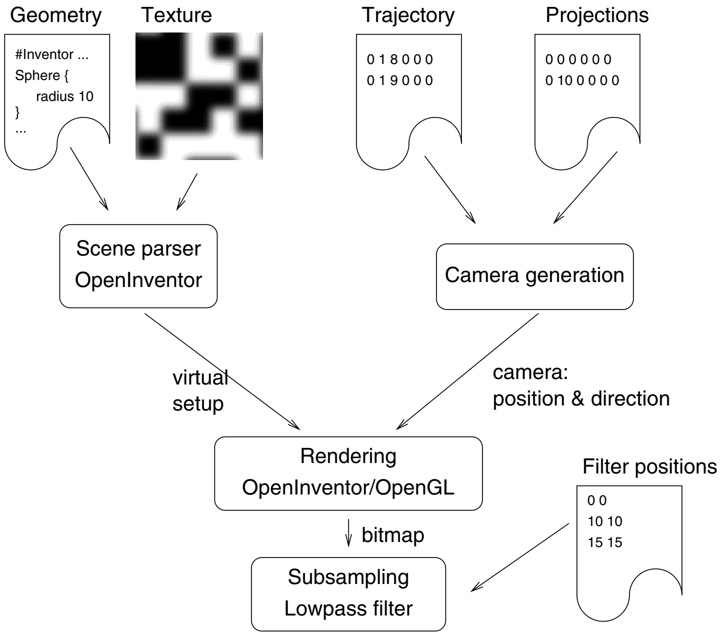

Figure 3.4: The processing done by the rendering component. The geometrical description, the textures, the projection list and a trajectory file are parsed. For each point in the trajectory and each projection a bitmap of the scene is rendered and a set of low pass filters is applied to the bitmap.

3.2.2 Spherical rendering

This section describes in detail the rendering for for the model of the tangential cells described in chapter 4.

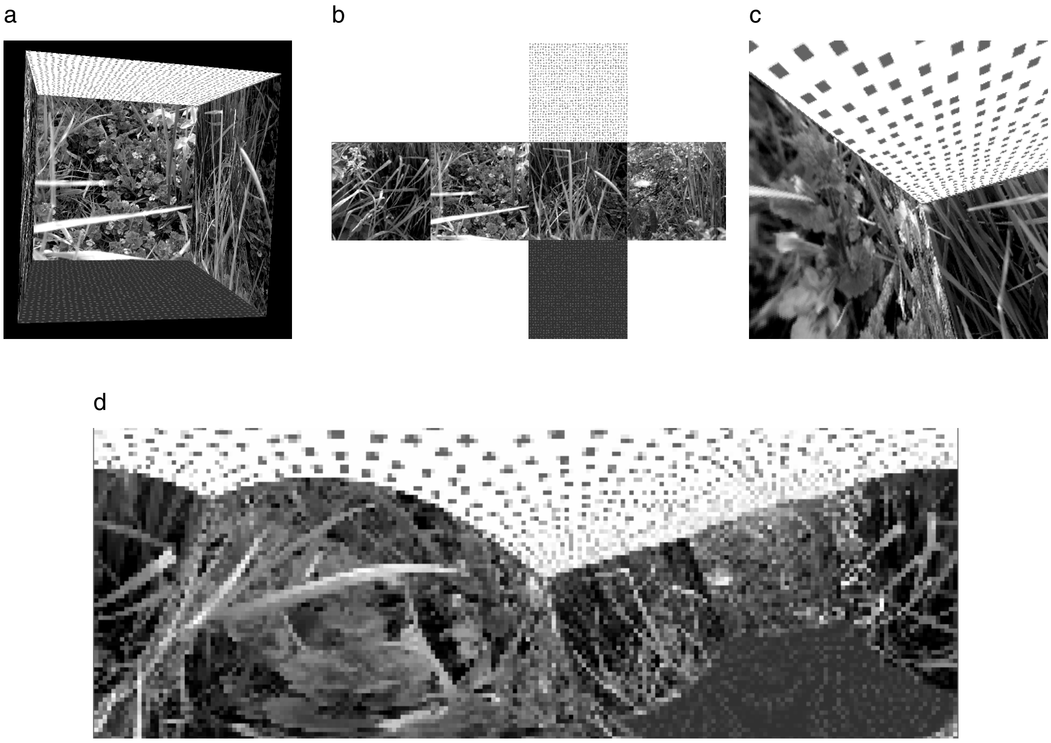

Figure 3.5: Different renderings of the same environment. (a) the box used for flight experiments by Schilstra and van Hateren (Schilstra and van Hateren, 1998b) viewed from outside, back wall removed to show the inside. (b) The six textures forming the renderer input. (c) A frontal view from the cockpit of the fly viewing one corner of the cube. (d) The same view as shown in (c) in a cylindrical projection generated by spherical rendering.

For modelling purposes it is useful to describe the arrangement of input elements by their viewing directions. In a raytracing system, this could be done very directly by generating the traced rays based on a list of viewing directions. However, with a rendering algorithm based on planar perspective projection like *OpenGL*, the spherical projection must be approximated by several planar projections. By calculating 6 views of a scene with orthogonal image planes, the entire environment can be mapped (figure 3.5b). By intersection of the resulting cube formed by the six images with the viewing directions of the simulated ommatidia, a spherical rendering can be achieved (figure 3.5d).

A similar, but independently developed approach to solve the problem of spherical rendering was taken by Neumann for the simulation of a biomorphic helicopter control system (Neumann, 2002, 2004). Neumann points out that for the intersection different from the center of the cube's sides, the circular Gaussian filter needs to be distorted to get a correct mapping of the environment to the input element (figure 3.6, Neumann, 2002).

However, this implies to compute a different filter mask for each position on the planar projection. To keep the rendering system simple, the renderer described in this thesis applies a circular Gaussian filter to the planar image at each intersection point. This leads to a correct result only in the centre of the planar projections, the small error introduced by applying circular filters at each position was accepted here.

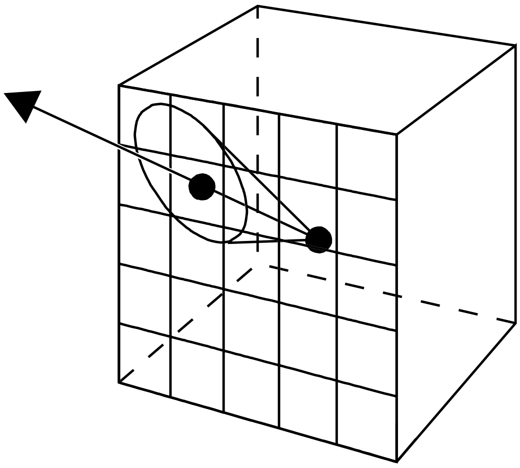

Figure 3.6: Illustration of the distortion of a circular filter by the perspective projection to a cube (cut of a cone by the face of the cube). To get correct subsampling results for all viewing directions, filters have to be distorted appropriately. Figure adapted from Neumann (2002)

3.3 Specialised display device for flies: FliMax

Flying insects see the world through the fastest eyes found in the animal kingdom. The power spectra of light adapted photoreceptors of a blowfly (*Calliphora vicina*) show corner frequencies of up to 119 Hz (Tatler et al., 2000). These photoreceptors show distinct responses to pairs of flashes even if these are separated by only a few milliseconds.

To stimulate these eyes appropriately, a variety of elaborated techniques have been applied. For the first experiments on insect motion vision relatively simple mechanical stimulation equipment was used, mostly rotating drums covered with some regular pattern. This method practically limits the image motion to rotational movements. Translational motion can be presented to the animal only for a short period of time by actually moving the setup. To overcome this drawback,

---

Parts of the Text in section 3.3 was previously published in Lindemann et al. (2003).

mechanical projectors were developed that could be used to present approximations to both rotational and translational patterns to the fly (Götz, 1968). In later experiments, electronic display devices were used. Using special purpose digital image synthesisers and high frequency cathode ray displays, moving patterns could be presented to the fly at appropriately high display refresh rates (Borst and Egelhaaf, 1987).

In replay-experiments which were done using a standard VGA monitor operating at 100Hz for the presentation (Kern et al., 2001b), a time-locking of action potentials to the refresh frequency of the image could be documented, while experiments with simpler stimuli that were presented on a cathode ray tube display operating at 186Hz did not show such effects (Warzecha et al., 1998).

Another challenge for the presentation of naturalistic optic flow is the nearly panoramic vision of the animals. With their large compound eyes they have an almost omni-directional view. Only a small part of the visual environment is masked by the body of the fly. To stimulate large parts of this visual field, several cylindrical devices were developed that display patterns on an array of light emitting diodes (LEDs). These devices present pattern sequences at high temporal resolution, but they are usually limited to a certain set of patterns. The device used by Kimmerle et al. (2000) can show one-directional striped patterns by selectively switching on complete rows of LEDs. A device introduced by Strauss et al. (1997) can present arbitrary patterns constructed from 9 luminance levels.

To be able to replay arbitrary behaviourally generated stimuli to the fly on a panoramical screen and with the appropriate update frequency, FliMax (see figure 3.7) was developed. The hard and the software of this device is described in the following.

3.3.1 Design principles of FliMax

FliMax is able to present arbitrary patterns at a luminance resolution of 256 levels. It covers most of the visual field of a blowfly (see figure 3.8), presenting the image sequence at an update rate of 370Hz.

FliMax displays each frame of an image sequence by the luminance of 7168 light emitting diodes (LED), mounted on the inner surface of the device. A fly placed in the centre of the device thus views the LEDs directly.

Geometric design

An ideal stimulator should present the images on a spherical surface where the image elements would be located at equidistant positions. On the other hand, the most convenient layout for electronic circuits is a flat printed circuit board

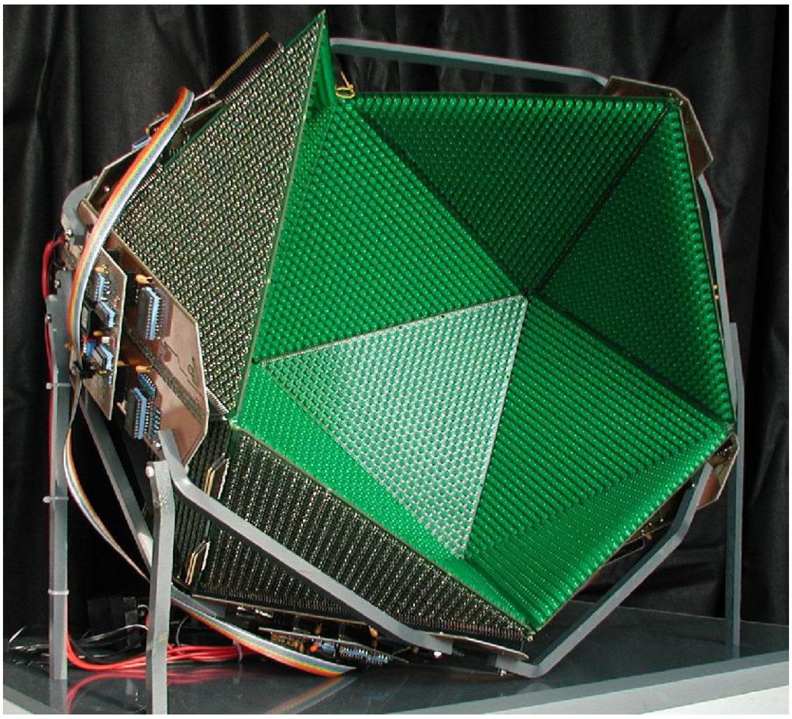

Figure 3.7: Photograph of the FliMax.

(PCB). In FliMax the sphere is approximated by an icosahedron, while 14 of the 20 triangles forming the complete solid are used. The isosceles triangles haven a base length of approximately 30cm, the inscribed sphere of the icosahedron has a diameter of 44.8cm. The diameter of the round LEDs is 5mm, the emitting wavelength is 567nm. The angle of emittance as specified by the manufacturer is $60°$, but measurements on individual LEDs indicate only $35°$ (full width at half maximum) emittance angle. The central LEDs of a triangle are separated spatially by $2.3°$ visual angle seen from the centre of the device, the angular resolution changes to $1.5°$ towards the edges of the triangles. For mechanical reasons, the separation of the LEDs on the edges of neighbouring triangles is different for different pairs of triangles and is larger than the separation within each triangle. This makes the edges of the triangles visible as dark lines. Because these lines are fixed in the visual space, they should not alter the responses of the large field motion sensitive neurons.

Electronical design

For electronic purposes the 14 triangles are combined to 7 pairs (rhomboids) that are identical electronical modules. Electrically, each rhomboid carries a square

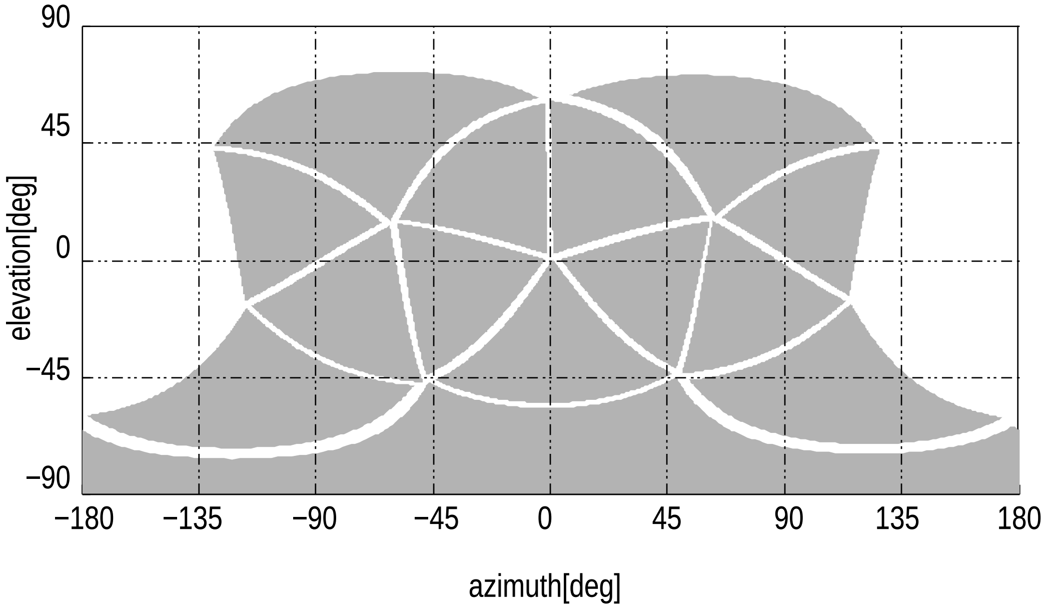

Figure 3.8: Plot (cylindrical projection) of the regions of the visual field covered by the FliMax (grey). The white lines between the grey areas indicate the edges of the triangular modules of the device. Figure adapted from Petereit (2002)

matrix of 1024 LEDs in 32 rows of 32 columns. Figure 3.9 shows the principal schematics of these rhomboids. The rhomboids are identical except from an individual address which is used to control the sequential update.

Electronically, FliMax is designed as a special VGA output device which can be driven by a standard VGA card. The VGA signal is interpreted by the electronics of the device designed and implemented by Paul Meyer and Udo Witte. The VGA signal fed into the electronics is composed of three colour channels (red, green, blue) and two synchronisation signals. The VGA writes an image of 224 rows with 128 pixels each. These are synchronised by one vertical sync impulse per update cycle and 224 horizontal sync impulses within each update cycle. A third synchronisation signal is carried by the blue colour channel, which is toggled between minimal and maximal intensity every 4 pixels. This creates a square wave pixel clock signal on the blue line with sixteen periods in each horizontal sync period. (see also figure 3.10).

The resulting three sync impulses are used by a programmable logic to generate an addressing of individual LEDs on the device given by a rhomboid address $(0..7)$, a row address $(0..32)$ by counting of the hsync pulses and a column address $(0..16)$ by counting pixel clock periods. The whole counting process is reset by the vsync pulse. The rows of each rhomboid are split into two groups of 16 LEDs fed by the red and the green colour signal, respectively. In each clock tick of the

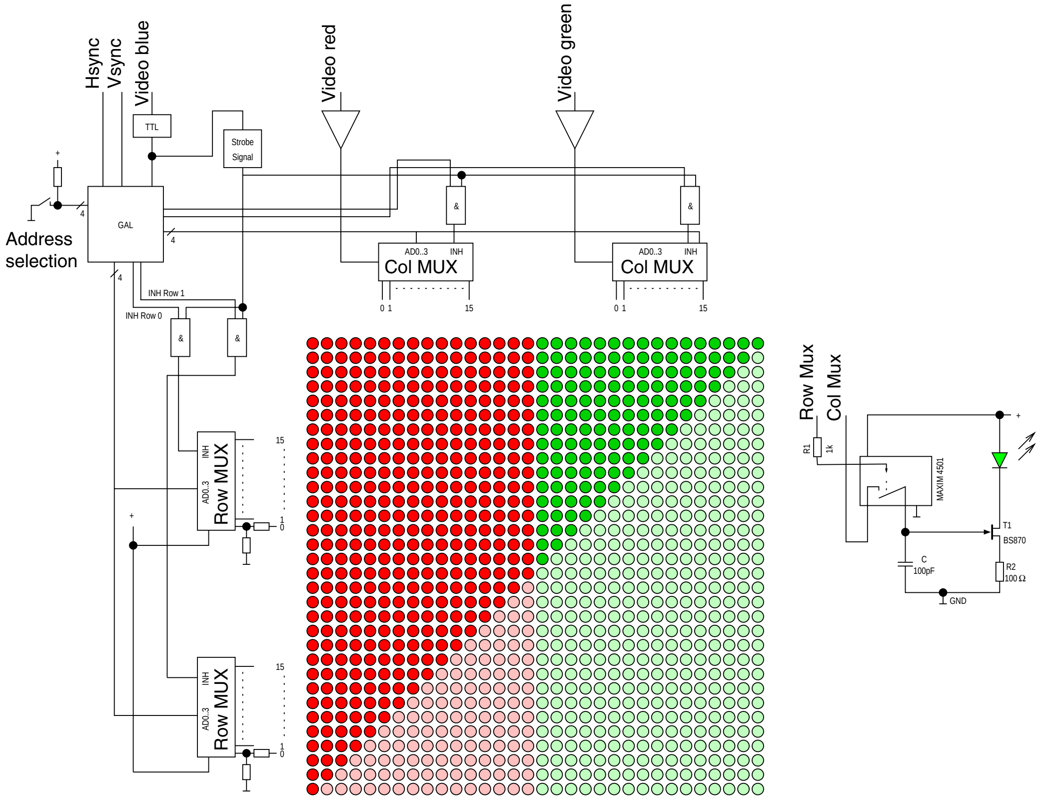

Figure 3.9: The principle schematics of one module of FliMax. The logical circuit drawn left and above of the LED matrix controls the update sequence. The LEDs updated to values coded by the either red and green VGA signal are draw red or green accordingly. The stronger colour is used for LEDs mounted on the first triangle, the lighter colour for the LEDs mounted on the second triangle. Each of the matrix elements in the left part represents a sample and hold circuit as drawn to the right.

pixel clock (blue colour signal), a pair of LEDs is updated according to the voltage present at the red and the green signal lines.

The individual LEDs are each accompanied by a sample and hold circuit that stores the luminance value between updates. In between the updates the luminance of the LEDs is held constant on this stored luminance level. Thus the device is illuminated constantly if the updates are done with identical images, in contrast to the situation found with cathode ray tubes, where each point on the surface is emitting light only for a short time after the update.

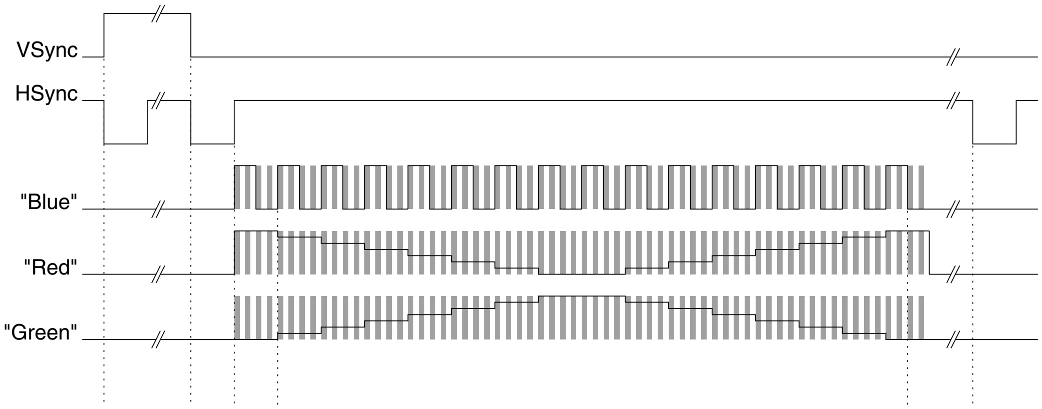

Figure 3.10: A timing diagram for the VGA signals used by FliMax. The “blue” colour signal of the VGA is used as a pixel clock. The “red” and “green” signals encode the luminance levels of a pair of LEDs in an analogous voltage signal. The gray stripes indicate the VGA pixel clock Each LED is associated with 8 pixels in the VGA memory. The VSync pulse initialises an update cycle, the HSync pulse marks the start of a row of LEDs.

3.3.2 Software

The Software driving the FliMax can be separated into two parts. The first component has to initialise the VGA adapter in an appropriate way, the second component has to write the images into the VGA memory synchronously with the Vsync pulses generated by the hardware.

For both parts, different implementations exist. A first implementation of the software was developed as an MS-DOS application. This operating environment has two advantages for this purpose. First, the direct access to the hardware, namely the VGA registers is easy, because MS-DOS does enforce the separation of driver functionality and application code. The second advantage results from the fact that MS-DOS has no preemptive multitasking which eases the development of real time code very much, if the system's interrupts are disabled. To keep the programming effort tolerable, an old fashioned software interface to the VGA hardware was used, which limits the performance of FliMax. As a result, the device cannot display the full 256 luminance levels of the VGA signal but only 8 of these selected by a lookup table. This implementation was used for all experiments described in this thesis. Nevertheless, the system is not described here in detail because a new better implementation exists and will be used for future experiments (For details on the MS-DOS based system see Lindemann et al., 2003).

This second implementation is based on the Linux operating system. This approach has the advantage that existing driver code can be used for the initialisation purpose, which eases the use of the capabilities of modern VGA adapters. Only with these capabilities, the full performance of the FliMax is achievable. The drawback of this approach is the limited real-time capability of the standard Linux kernel.

VGA initialisation

The initialisation is done by defining the same image geometry and timing using the frame buffer special device, a software interface to the video hardware provided by the Linux kernel. The colour mode of the hardware is set to 24bit true colour, allowing to specify the LED's intensity on the green and red colour channel in 256 steps. The displayed image geometry is set to 224 by 1128 pixels at a frame rate of 370Hz resulting in a pixel clock value of 28MHz.

Modern graphics hardware is capable to read from an arbitrary section of the VGA memory when generating the image signals. By changing the pointer to the starting address between two updates, double-buffering can be implemented. For this purpose, the virtual resolution of the image is set to 448 lines of 128 pixels, doubling of the true geometry in the vertical expansion. Thus the code transferring the images has to complete the update of the hidden buffer within the period between two VSync pulses.

The blue colour component of the whole buffer is initialised to create the pixel clock pattern on the associated colour signal.

3.3.3 Rendering for FliMax

For FliMax 14 different camera images are computed for each position in the trajectory, one image for each of the triangles forming the device. The orientation of each camera is calculated from the 3D-coordinates of the triangle corners in the device. The rendered images have to be sub-sampled using a triangular grid of sampling points. This is done by applying a Gaussian filter centred at the according LED position. All filters have the same width which approximates the spatial resolution of the blowfly eye (Petrowitz et al., 2000; Smakman et al., 1984), i.e. their width at half-maximal amplitude is $1.75°$.

Simulations using a model of fly photoreceptors (van Hateren and Snippe, 2001) and a preliminary model of fly LMCs (second order neurons presumably in the motion pathway) indicated that flickering artifacts can be observed at moving edges and textures. To reduce these spatial aliasing and resolution artefacts in the 370 frames presented per second in the FliMax, the trajectory for the replay is sixfold oversampled to this rate in time, having 2220 positions per second.

This oversampling is removed from the generated image sequence by averaging six subsequently rendered frames for each displayed frame, leading to a motion blurring in image positions with large image velocities.

The result of this process is a sequence of 370 images per second prepared for the replay to an animal in an electrophysiological experiment in FliMax. These images contain 24Bit true colour luminance values for each LED position of which only the green channel is further processed. For each reconstructed image the (green) intensity values are converted to the format expected by the replay software.

Replay of rendered images

Following the initialisation, the software has to update the video memory timed by the vertical synchronisation pulses generated by the graphics hardware. In addition to that, the same program has to generate a trigger pulse and a time reference signal for the computer recording the electrophysiolocial data in an experiment (figure 3.11).

The images rendered for the presentation on FliMax are converted into the format of the video memory and stored in a custom file format. This file format stores the 7168 luminance values of each FliMax frame. The redundant format for the video memory is generated on the fly by the replay software. The format is extendable to compress the update sequence by storing only the luminance values of the LEDs changing luminance between two updates, a technique used in simple animation file formats like the so-called “flic file format" (Kent, 1993).

It then iteratively updates the hidden part of the video memory and shifts the pointer referencing the displayed buffer triggered by the VSync pulses signalled by the VGA hardware. For each memory update, a byte code signalled on the parallel port of the computer driving FliMax is incremented as a control signal for the correct timing of the replay.

The least significant bit is recorded alongside the electrophysiological signals and allows to check for the exact relative timing of FliMax updates and neuronal events, on the one hand, and to monitor the timing precision and duration of the update process of FliMax on the other hand.

3.3.4 Experiments with FliMax

This section describes first experiments conducted with FliMax as the stimulation device. They had the purpose to prove that the results obtained with the device are compatible to the knowledge about the neurons collected using simpler

---

The experiments described in section 3.3.4 were done by Dr. Roland Kern and Christian Michaelis.

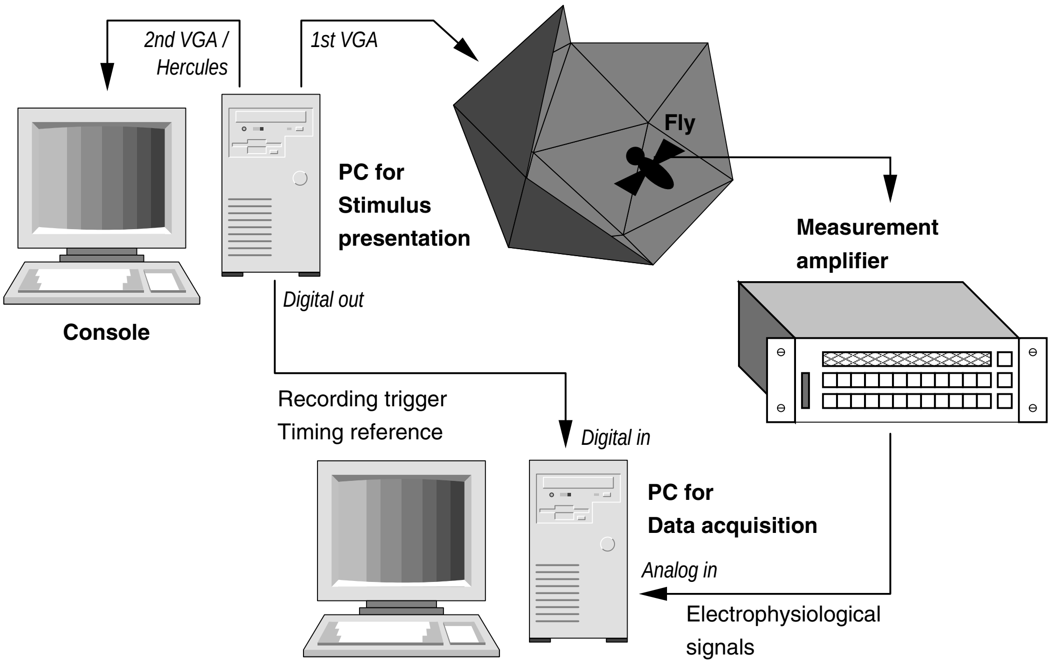

Figure 3.11: The experimental setup with FliMax in an electrophysiological replay experiment. One PC having two display adapters serves for the replay of the stimuli on the FliMax. Via a digital line, it triggers the acquisition of electrophysiological signals on a second PC and provides a timing reference signal to be recorded concurrently for analysis purposes.

stimulation equipment. Furthermore the comparison of the results shows that the high update frequency and the sample and hold properties of FliMax improve the signal quality significantly by almost completely avoiding stimulation-induced frequency peaks in the power spectrum of the neuronal response.

Conventional wide-field gratings

Simulated conventional grating stimuli were used for experimentation to test whether the responses obtained with FliMax differ in any obvious way from those obtained with stimulus devices used in previous studies, such as mechanically moving drums or monitor screens. Figure 3.12 displays a sample record of an HSE-cell response (see section 2.2.3 for a description of HSE cells) to constant velocity motion in the preferred direction and subsequently in its null direction. The record shows the typical features of HSE-cell responses: They are characterised by graded de- and hyperpolarisations relative to the resting potential. On average, the depolarisation during preferred direction motion is 15.2mV (number of average responses $N = 12$) and the hyperpolarisation during null direction motion is 8.4mV ($N = 12$). These values are in the range of responses that were published in earlier accounts (Hausen, 1982b).

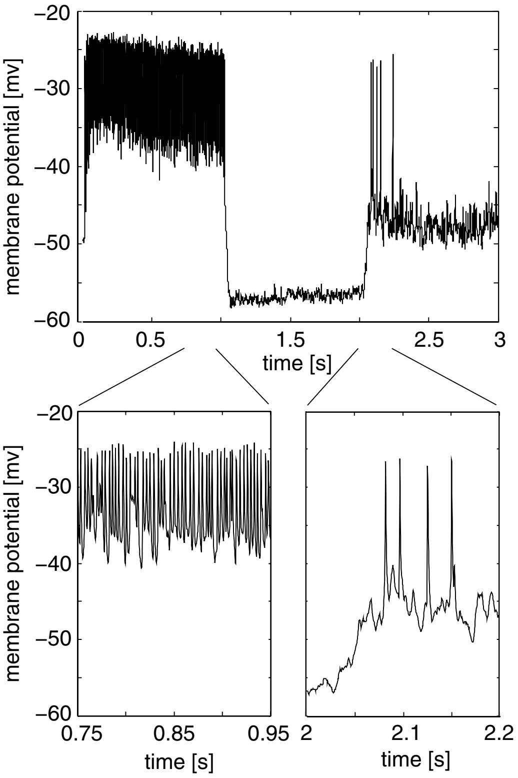

Figure 3.12: Responses of the HSE-cell stimulated by FliMax displaying grating patterns. The pattern moved initially at a constant velocity for one second in the cell's preferred direction and then for another second in the null direction During the last second the pattern is stationary. The graded depolarisations during preferred direction motion are superposed by small-amplitude spike-like depolarisations (see also bottom diagrams). The spike-like depolarisations are large when they are generated as rebound spikes after a hyperpolarisation of the cell (bottom right).

Rapid spike-like depolarisations superimpose the graded depolarisations. These spikelets vary in amplitude to a large extent. They may hardly be discerned in some preparations, but they may also reach amplitudes of full-blown spikes in other preparations. Spikelets superimposed on large graded depolarisations tend to be smaller than those generated at the resting level of the cell as, for instance, just after the release from hyperpolarisation elicited by null direction motion (figure 3.12). These features of spikelets are well documented (Haag and Borst, 1998; Hausen, 1982a) and the consequence of the activation and inactivation properties of voltage-dependent sodium channels (Haag et al., 1997; Hengstenberg, 1977).

In conclusion, as judged by the responses to classical grating patterns FliMax appears to be fully appropriate as a visual stimulation device.

Optic flow generated by walking flies

The membrane potential of HSE-cells fluctuates in a complex manner when the cell is stimulated with image sequences as are seen by a fly walking around in its environment. The characteristics of the membrane potential fluctuations elicited by behaviourally generated optic flow and what they may encode about the animal s self-motion and/or the layout of the surroundings have been analysed in previous accounts. It was concluded that the HSE-cell encodes the direction of turns of the walking animal largely independent of the spatial layout and texture of the environment. Only when the animal is very close to an object, the neuronal responses are affected by it (Kern et al., 2001a,b). These previous analyses were limited by the fact that image sequences were presented on a monitor screen that covered only part (though a large one) of the cell's receptive field. All displays with a cathode ray tube (CRT) do not show a still image but iteratively flash each pixel at the frame rate. In contrast, FliMax presents a constant image between different updates as long as the image does not move. Moreover, for technical reasons stimulation was based in previous studies on a 100 Hz video player (Kern et al., 2001b). Although the frame rate was much higher than that of conventional video players, it led to some time-locking of the neuronal response to the frame rate. With FliMax now was tested whether the responses of HSE-cells may differ when they are elicited by the same image sequences. The responses will be related, as in previous studies (Kern et al., 2001a,b), to the rotational velocity component of the optic flow generated by yaw movements of the fly. Image sequences generated by walking flies were presented to the same set of flies in two alternative ways:

(i) The device operates at an update rate of 370 per second, but the images were exchanged, as in earlier experiments with a computer monitor, at 100 exchanges per second; this procedure implies that each frame was presented 3–4 times.

(ii) The device operates at an exchange rate of 370 per second. The image sequences were linearly interpolated so that image exchanges could be done at a rate of 370 frames per second.

As is obvious from the examples shown in figure 3.13c and d the time course of the responses to both types of image sequence are virtually the same. Moreover, these responses do not differ in any pronounced way from the time course of the responses that were obtained in the previous study with a monitor screen as stimulus device (compare traces in figure 5c with c and d). Only the overall response amplitudes that were obtained with FliMax are somewhat larger than those obtained with a conventional stimulus device. Notwithstanding, this comparison shows that the general results of the previous study are still valid and that the same conclusions as were drawn in the previous study would have been drawn on the basis of the improved visual stimulator.

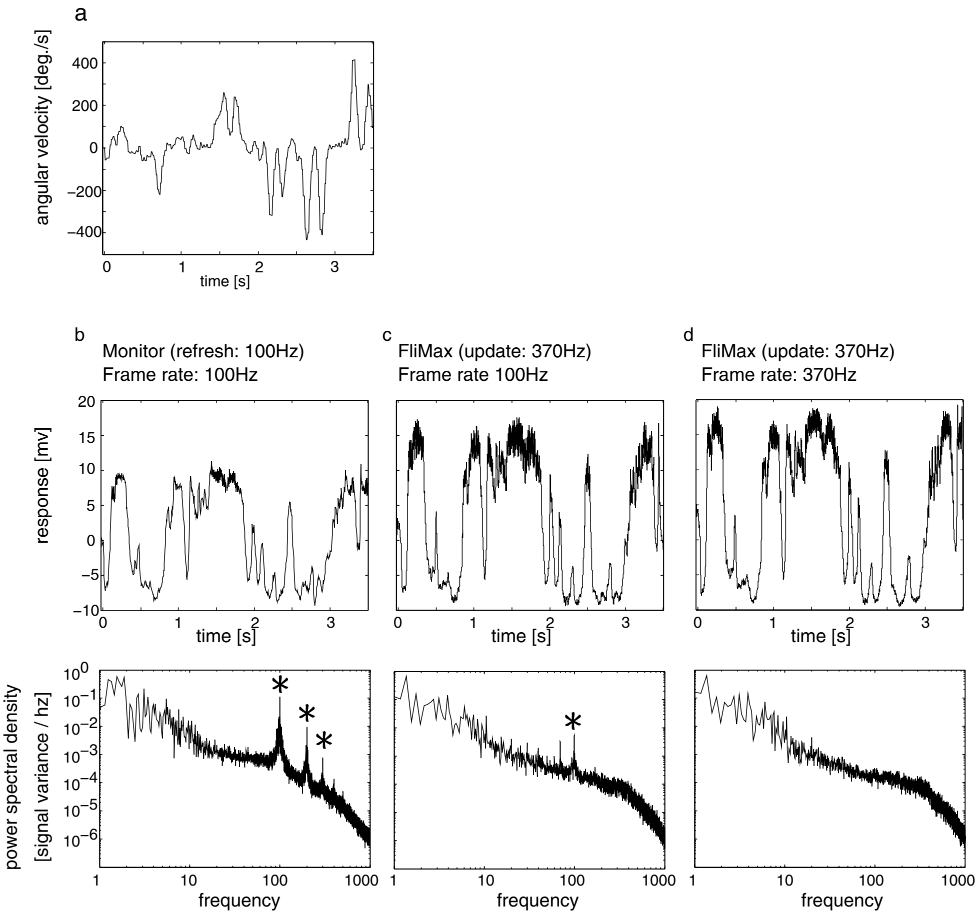

Figure 3.13: Responses of the HSE-cell to behaviourally generated optic flow as experienced by a walking fly. (a) Angular velocity of the fly as a function of time (left) and walking track within the arena (right). The orientation of the fly's body axis is shown only at three instants of time; positive (negative) values denote counter-clockwise (clockwise) turns. (b) Section of the average response of 8 HSE-cells stimulated with a computer monitor at a frame rate of 100 Hz (upper diagram) (Data taken from Kern et al., 2001b). Average power spectrum of individual response traces have a pronounced peak at 100 Hz and at integer multiples of this frequency (see asterisks; bottom diagram). (c) Average response of 15 HSE-cells stimulated by FliMax at a rate of 370 Hz; the effective image exchange rate was 100 Hz (upper diagram). The corresponding average power spectrum of the individual response traces has a peak at 100 Hz which is, however, much smaller than the peak shown in B (bottom diagram). (d) Average response of 11 HSE-cells stimulated by FliMax at a rate of 370 Hz; the image exchange rate was 370 Hz (upper diagram). The corresponding average power spectrum of the individual responses does not show any obvious peak at 100 Hz or 370 Hz (bottom diagram).

Despite these similarities on the time scale at which the responses were analysed in the previous study, the temporal structure of the responses on a time scale of milliseconds depends on the way the image sequences were presented. This feature can be seen in the power spectra of the responses (figure 3.13B D, bottom row). As is characteristic of fly HS neurons (Haag et al., 1997; Warzecha et al., 1998) the responses contain most of their power at frequencies below 10 Hz. The attenuation of high-frequency components is a consequence of time constants that are an inevitable constituent of movement detectors (Egelhaaf and Borst, 1993). However, the power spectrum of the responses obtained in the previous study with stimuli generated on a monitor screen reveals pronounced peaks in the power spectrum at 100 Hz, i.e. at the refresh rate of the monitor as well as the exchange rate of the image frames, and at higher harmonics of this frequency (figure 3.13B, lower panel). These peaks are much reduced when the same image sequences are shown without CRT flashing, but still at an exchange rate of 100 Hz (figure 3.13C, lower panel). This finding suggests that the time-locking of the neuronal responses has to be attributed mainly to the flashing of conventional monitors and not so much to the rate of the image exchange. When the frame exchange rate is increased to 370 Hz, the maximum that is possible with FliMax, no distinct peak is discernible at this frequency in the power spectrum or at half this frequency (figure 3.13D, lower panel), which is the resulting frequency for the least significant bit.

These findings allow to draw the following conclusions. (i) Even if the responses time-lock to the update and/or frame rate of the motion stimulus on a fine time scale, the responses are virtually indistinguishable on a coarser time scale. (ii) Exchange rates of 185/370 Hz as are possible with FliMax are fully appropriate to elicit the illusion of smooth motion in fly motion sensitive neurons.

3.4 Recording stationary flight behaviour: FlyView

For the investigation of optic flow based flight control, analysing the sensory system is essential, but only the first step. The sensory motor coupling can be investigated with the methods of systems analysis, if the behavioural reactions of the animal to certain visual stimuli are known. In a freely behaving fly, the motor system is not only affected by visual inputs, but also by signals from various other sensory modalities that are fused with the visual information. For a systems analysis, it is useful to be able to record the behavioural responses to only one of these modalities, i.e. to the visual stimulation. In open-loop experiments the input-output organisation of the sensory motor coupling can then be studied. Assuming that the main input to the sensory-motor interface are the tangential cells (see section 2.2.3 for details), this could lead to hypothesis of the further processing of the tangential cell output.

Fly behaviour was successfully analysed in open-loop experiments previously. If the animals are tethered by attaching their thorax to a support, they usually start to flap the wings if their legs are free. In such a situation, the fly does not get mechanical or visual feedback of the forces generated by the flapping wings or the neck muscles, if the head is fixed in relation to the thorax. However, when a tethered flying fly is confronted with visual motion stimuli, it responds to these motions by characteristic changes in the flight forces.

A method for recording these flight forces is to attach the fly to a electromechanical device measuring one component of the flight force, either torque about one axis or one translatory force component, while actively compensating for this force. Such devices were built in the 1960s to record forces generated by a tethered fly. Figure 3.14 shows the functional principal of an electromechanical torque compensator. Several studies with such setups characterised the responses of a tethered fly to moving patterns simulating rotational or translational optic flow (Götz, 1983; Reichardt and Poggio, 1976). In other studies the movement of the patterns were controlled in a simulated closed-loop by the forces measured by the compensator (Kimmerle et al., 1997; Reichardt and Poggio, 1976; Warzecha and Egelhaaf, 1996).

A second approach to quantify the behavioural response of a tethered flying fly to optic flow stimuli is to record the wingbeats directly. Such a technique was established for the fruit fly (*Drosophila melanogaster*). The device works by illuminating the flapping wings with infrared spotlights from above the fly. The light is received by specifically masked photodiodes beneath the fly. Depending on its position relative to the mask, the wing occludes differently sized parts of the mask. The modulation in the intensity registered by the photodiodes thus encodes the positional change of the wing (Götz, 1987). Amplitude and frequency of the wingbeat can easily be extracted from the signal. These parameters were found to covary systematically with the yaw force generated by the tethered flying fruit fly (Lehmann and Dickinson, 1997).

This section describes an implementation of a wingbeat analyser based on a digital highspeed camera and the adaptation of the method to the behavioural analysis of blowflies.

3.4.1 Implementation of a wingbeat analyser

The fly was viewed from below with a camera. Instead of the standard CCD sensors used in most video cameras, this camera uses a CMOS image sensor (FUGA 15d, C-Cam Technologies). This CMOS image sensor implements a randomly addressable array of photo diodes. The chip basically behaves like a 256KByte memory chip. When the computer interface applies a row- and column-address, the chip converts the analog signal of the respective photodiode with it's on-chip

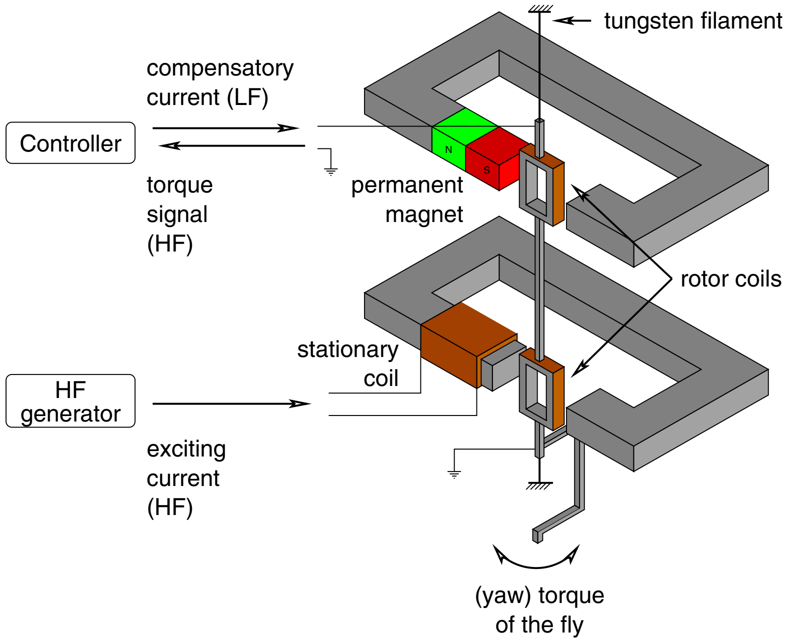

Figure 3.14: Functional principal of the torque compensator. The main functional unit is a rotor constructed from two coils attached to two tungsten filaments. For small rotations, these filaments form a very good bearing for the rotor. The system senses and actively compensates for the torque generated by the fly in the following way: A high frequency (HF) current causes and alternating magnetic field. This induces a HF current in the sensing coil depending in phase and amplitude on the orientation of the coil relative to the field (lower part of the system). Based on this current, a controller circuit generates a low frequency (LF) compensatory current which stabilises the coils relative to a permanent magnet (upper part of the system). (Figure adapted from Götz, 1964)

A/D converter to an 8-Bit digital value transfered to the computer.

Because address changes can only be applied with a limited frequency, the transfer of a full frame is relatively slow compared to standard cameras; the typical frame rate for full frame transfers is below 20 Hz. However, if only a small subset of the pixels needs to be transfered for an application, the transfer rate for these image parts is extremely high.

For the application discussed here, only a ring of a few pixels needs to be inspected to reconstruct the position of the wings over time. With 50-100 pixels forming the sampled ring, transfer rates of 2kHz are no problem.

To get a reliable reconstruction of the wing trajectory, the transfer of the individ-

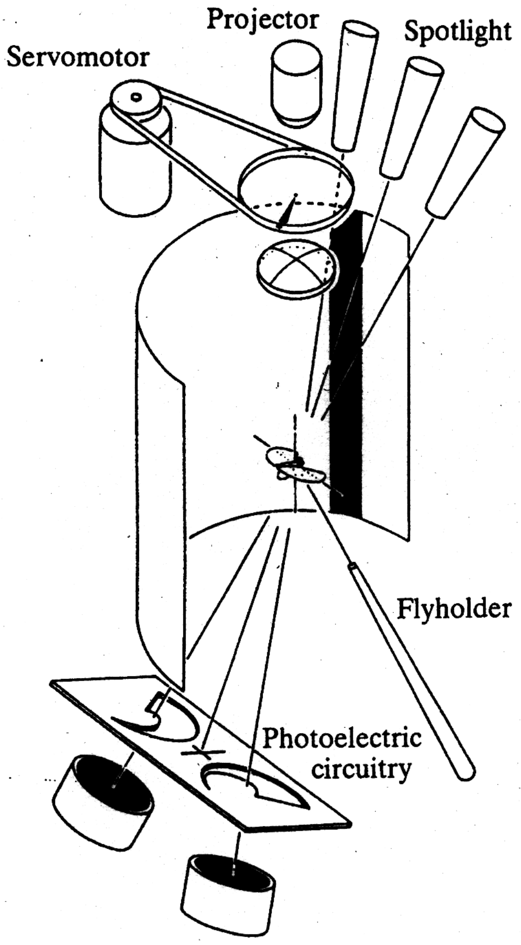

Figure 3.15: Design of the wingbeat analyser previously used for the recording of fruit fly wingbeat amplitude and frequency. The fly is illuminated by infrared spotlights. The light is received by photodiodes beneath the fly. The flapping wing covers part of a specifically designed mask, causing different degrees of occlusion depending on the wing position. The visual stimulus is generated by a special purpose projector, the angular position of the stimulus is controlled by the servo motor. Figure redrawn from Götz (1987).

ual samples must be timed precisely. To get a sample rate of 2kHz, a transfer of the pixels must be initiated every 0.5ms. To achieve reliably a constant sampling frequency, the time-critical part of the software is implemented as a hard real-time thread in the rtLinux extension of the Linux operating system (see figure 3.16).

A circular sampling grid for the data recording was defined by the experimenter. For both wings, the centre point of a semi-circle was defined manually on the image of the fly's thorax, the number of samples and the radius of the sampling circle was chosen identically for both wings (figure 3.17).

Data processing

The data recorded by the CMOS camera can be stored in an image showing the samples of the two semicircles in a row for each time-step. An example for such a 2D image is shown in figure 3.18.

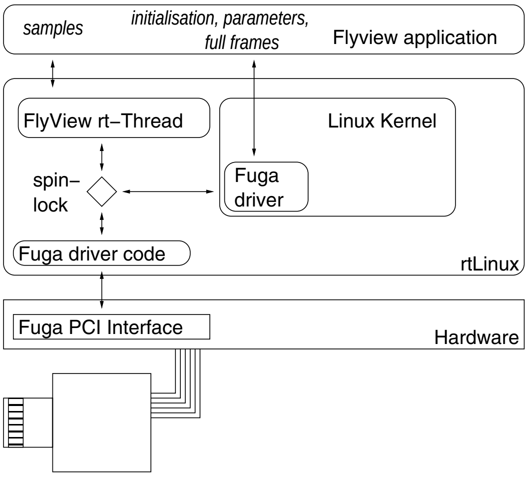

Figure 3.16: Software architecture of the wingbeat recording system. A reliable fixed frequency of acquisitions is achieved by running the time-critical part of the software as a real-time thread in the rtLinux operating system. For initialisation, full frame acquisition and the user interface, the standard Linux kernel interface is used.

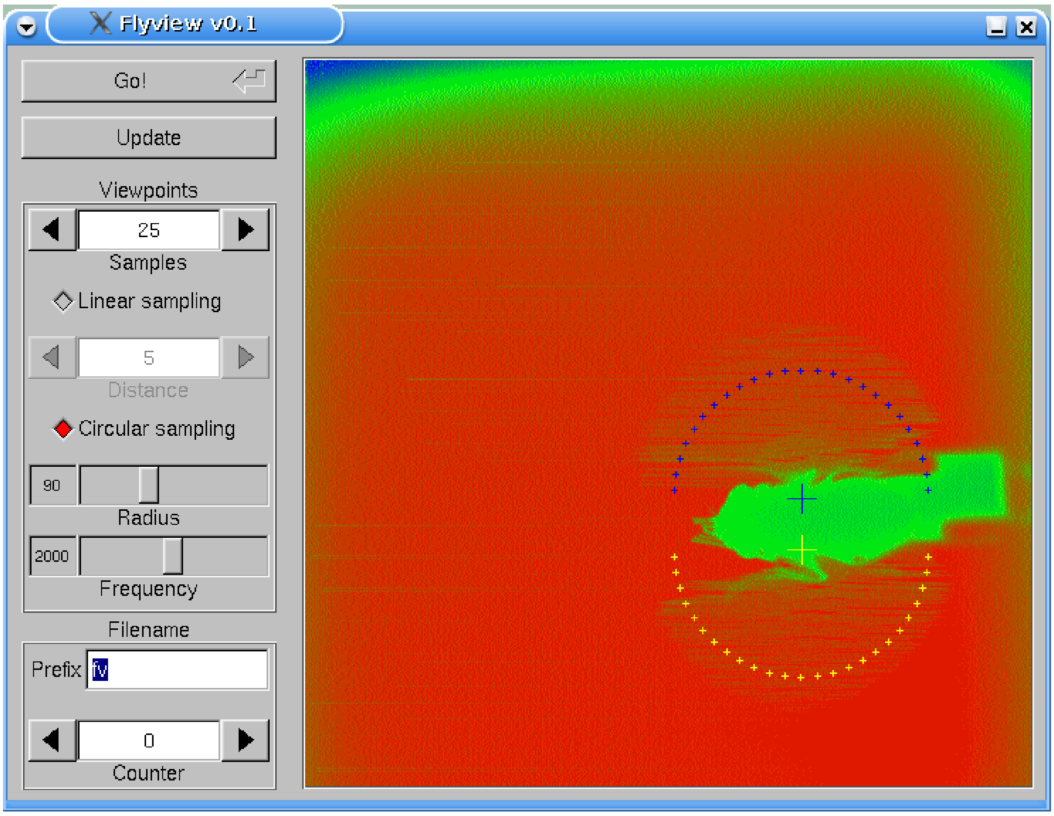

Viewpoints
Samples: 25
○ Linear sampling
Distance: 5
● Circular sampling
Radius: 90
Frequency: 2000
Filename
Prefix: fv
Counter: 0

Figure 3.17: Screen-shot of the user interface: The fly is visualised in false colour in front of the bright (red) background. The user has to place the semicircular sampling grit (yellow and blue crosses). The samples are acquired at the chosen frequency and stored to sequentially numbered files.

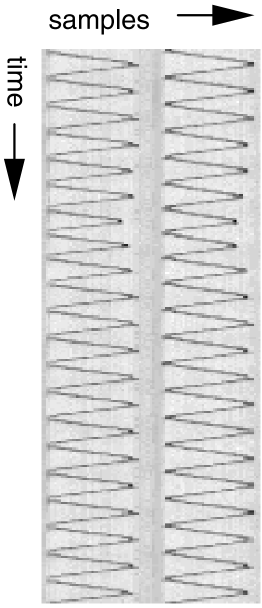

Figure 3.18: An example of the data recorded by the CMOS camera. The image contains the 2D sampling for each time-step in one row, adjacent time-steps in consecutive rows. The trace of both wings is clearly visible as a sinusoidal dark line. The image was normalised in contrast for printing purposes.

To reconstruct the wing trajectory from the recorded data, the position of the wing on the circular sampling grid must be extracted from the image. This is done for the two wings individually. This process involves five steps:

1. 2D-Blurring to reduce the pixel noise in the data
2. Threshold binarisation
3. Row by row segmentation
4. Interpolation of missing data points
5. Calculation of wingbeat frequency and amplitudes

The blurring of the input data was done using a 3×3 Gaussian convolution filter to reduce the effect of single noise pixels. For the edge pixels, the image was extended by one pixel of medium gray level (128).

For thresholding, a fixed threshold of 125 was used. This is a possible approach in this system, because prior to data recording the parameters for the on-chip A/D conversion were set so that the background intensity had a constant value across experiments.

In the segmentation step, the centre of each group of "black" pixels in the binary image was computed. For lines with more than one region, a simple heuristic was applied to select the correct one. To detect the correct region in the presence of noise regions, a linear prediction calculated from the two prior time steps was successful.

Additional regions can appear in the binary image either as noise pixels or when the fly extends one leg into the view of the camera. In the case of a leg in the camera view, this approach has a clear drawback. The position of the leg is typically kept constant by the fly over several wingbeats. Thus, if the algorithm mistakenly selects the leg region in at least two images, the linear prediction is close also to the leg region, trapping the heuristic as long as the leg is visible for the camera. To avoid this situation, the prediction needs to favour the moving wing region in the presence of an additional region at a fixed position. The very simple heuristic of calculating the prediction to lie between the prior position of the wing and the central pixel in the semicircle was chosen.

A more sophisticated approach would be to dynamically fit the data to a sine function. This would favour the correct region both in the presence of noise pixels or when a leg is visible to the camera. This was not implemented, because the simpler heuristic worked sufficiently well on the inspected data samples.

In the interpolation step, the wing position was linearly interpolated for time steps in which no regions were detected, if for the nearest neighbours the positions were detected.

For the calculation of wingbeat frequency and amplitudes, the local maxima and minima of each trajectory were detected. The frequency was computed for each period from the temporal distance of the maxima. The difference of the minimum and the maximum in each period was interpreted as the amplitude. For both values, an acceptance range was defined for off-line detection of mistakes in the trajectory reconstruction.

3.4.2 Torque compensator versus FlyView

To test, whether the yaw forces of blowflies can be estimated on the basis of the wingbeat amplitude, the wingbeat analyser was combined with an electromechanical torque compensator in a classical optomotor experiment.

The flies were attached to the torque compensator in the centre of a cylindrical setup carrying vertical rows of LEDs, displaying a binary coded horizontal pattern. By continuously updating this LED array with a stripe pattern, a rotating drum can be simulated (Kimmerle et al., 2000). This simulated drum rotated with constant velocity into different directions in subsequent 5 second periods. The optomotor response to this movement causes the fly to generate on average constant yaw force in the direction following the movement.

Figure 3.19 shows exemplarily the results obtained from the wing tracking. The amplitude difference of the two wings shows opposing constant values for segments of 5 seconds each, the pattern expected for the yaw torque. The synchronously recorded signal of a yaw torque compensator shows that this differential amplitude signal has qualitatively the same time-course as the yaw torque (figure 3.20). Numerous such experiments co-recording the yaw force and the amplitude difference of several different animals revealed that the amplitude difference is proportional to the yaw force in any recording, even if the animal generates yaw forces not obviously coupled to the stimulus.

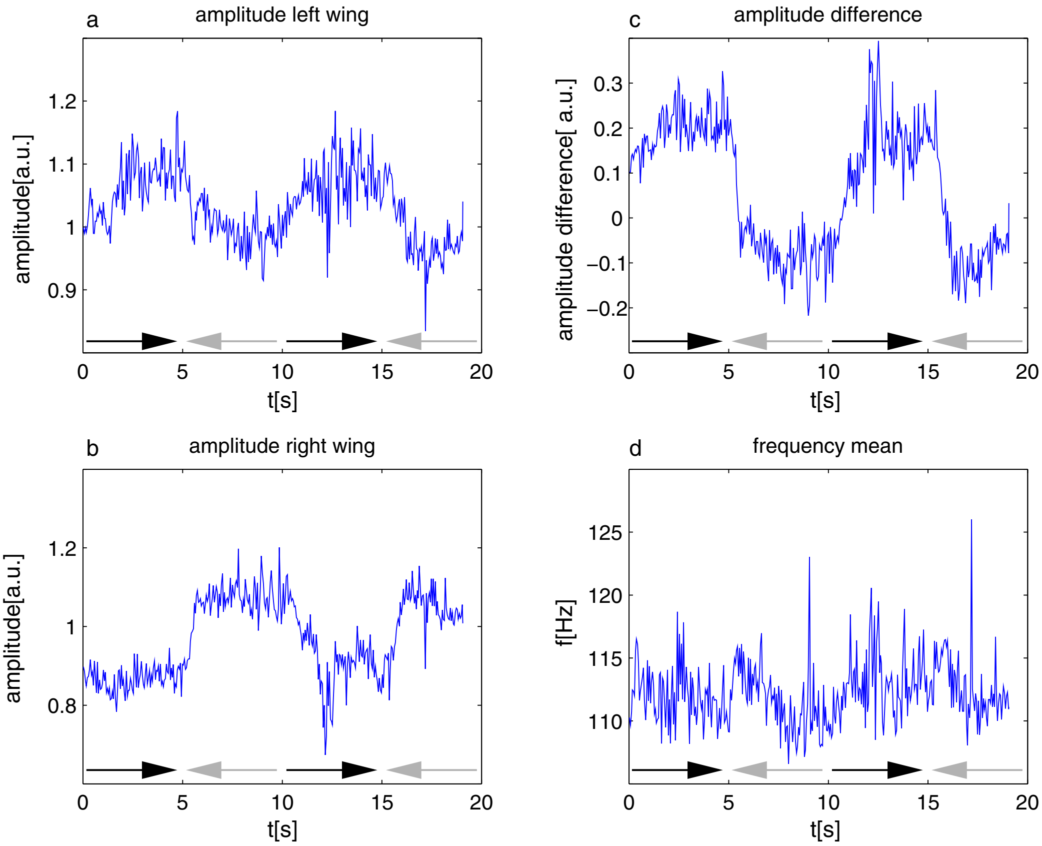

Figure 3.19: Example of the signals recorded in a wing-tracking experiment. The amplitudes of the two wings (a, b) and especially the amplitude difference (c) is coupled to the stimulus (movement direction indicated by arrows on the x-axis). The frequency is almost constant over the recording time. Amplitudes in a,b were normalised for plotting. The raw data was averaged over segments of 5ms.

3.4.3 Wingbeats in simulated translatory flight

To characterise the sensory-motor coupling of the fly in a situation different from the simple optomotor test stimulus of the rotating drum, the wingbeat analyser was mounted within FliMax and the wingbeats of the fly during simulated trans-

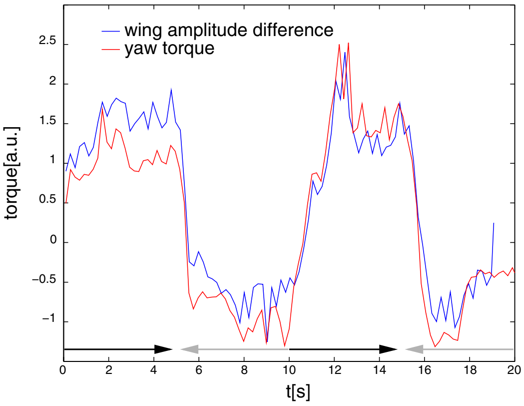

Figure 3.20: The amplitude difference in comparison to the simultaneously recorded yaw torque. Both signals were normalised for plotting.

latory flight in a flight tunnel were recorded. The tunnel was a realistic model of a flight arena used in behavioural experiments. In these experiments, the flies cruised freely in the same environment at velocities around $1\frac{\text{m}}{\text{s}}$, which was the simulated speed presented in the FliMax (Kern, personal communication).

These experiments were unsuccessful basically in three respects.

1. No obviously stimulus-coupled component of the wingbeat pattern was detected in the data collected in these experiments. Neither the frequency, nor the amplitudes showed consistent patterns coupled to the stimuli.
2. The flies reacted to the situation of the simulated translation in an unexpected way: Most of the animals simply stopped to flap their wings stationary when translational optic flow started. Another frequent observation was that the flies extend their legs in response translatory motion, a movement pattern previously interpreted to be a landing response (Borst, 1986). Several changes in the stimulus did not stop the flies from showing these responses. The velocity of the simulated translation was varied over a wide range of speeds and different dynamics for the onset of movement were used (e.g. ramp or step functions). Furthermore, air was blown in flight direction on the fly to stimulate the mechanosensory system in addition to the visual system.
3. Although the wingbeat analysis is principally capable to record the yaw forces generated by each single flapping of the wings, no pattern was found that indicated the saccadic rotations.

The absence of saccade-like events in the wingbeat signals is most likely the basic problem of this approach. The movement pattern of a saccadic turn is resulting in a yaw turn on the whole, but the fly does not steer a yaw turn, but steers a banked turn (Schilstra and van Hateren, 1999). Such a turn can be viewed as a combination of rotations: Initially, the fly rolls towards the inner side of the intended turn. Following this roll, the fly has to steer a combination of yaw and pitch to change the flight direction. If the roll has an amplitude close to 90°, the yaw component in this movement is zero in fly body coordinates. After steering the turn, the body rolls back into the normal horizontal flight orientation.

Like in the wingbeat analysis, saccadic events were never observed in blowflies flying tethered to a yaw torque compensator (Martin Egelhaaf, personal communication). In contrast, such events were detected in both the yaw torque and the wingbeats recorded in fruit flies (Heisenberg and Wolf, 1984) suggesting that these flies steer the saccadic turns in a different way.

Principally, all six degrees of freedom of the flight forces should be predictable from the wingbeats. While it should in principle be possible to reconstruct more parameters from the camera images obtained in the setup described above, the analysis of the complex aerodynamical mechanisms in fruit flies (Dickinson et al., 1999; Lehmann and Dickinson, 2001) suggest that a prediction of the resulting forces is by no means trivial. A first attempt to predict flight forces of fruit flies from the movement pattern of their wings based on a quantitative analysis of the force generation in aerodynamically scaled experiments was described by Schenato et al. (2001).

3.5 Closed loop simulation of a virtual blowfly

Hypotheses how the responses of motion sensitive neurons are coupled to the behavioural output can be evaluated in a closed loop simulation. Therefore the rendering process and the simulation model of the sensory neuronal system need to be coupled to a module implementing the formalised hypothesis for the behavioural control. A physical model of the fly can then calculate the movements of the animal resulting from the forces generated by the neuronal system. To close the loop, the new position is passed to the renderer for the generation of a new retinal image. Figure 3.21 sketches such a simulation loop.

While this loop could principally be implemented in a single simulation application, it has several advantages to split the loop into separate software modules. First, this separation allows to reuse parts of the loop for other purposes. The rendering, for example, is needed to generate stimuli for electrophysiological experiments and for the sensory model under open loop conditions. Second, the separation of modules makes it easy to experiment with different variants of the individual parts of the loop. Third, a modularised simulation software is better maintainable.

In the system described here, the different modules of the loop are implemented as separate Linux processes. These processes are designed to read their input from the standard input and writing their results to standard output. This allows

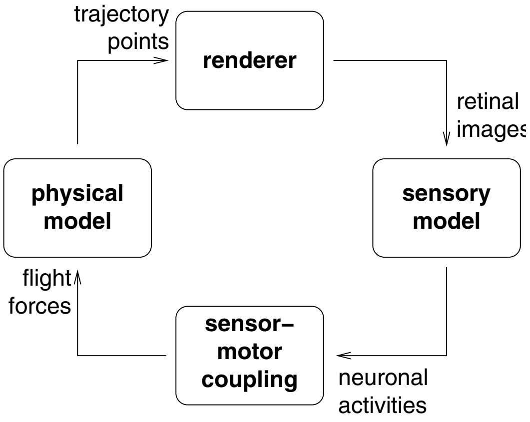

Figure 3.21: Modules of the closed loop simulation system.

the coupling of the modules using simple Unix-pipes[2] This design separates the different modules perfectly, but it also introduces additional computational effort by creating the necessity of continuous process switching during a simulation run. Passing the intermediate results from one module to the next via the operating system is costly, too.

The Unix shell[3] allows to concatenate several commands using pipes, but it does not provide a mechanism to close a loop of processes. A special file type, the so-called named pipes or FIFOs, provided by most modern Unix systems can be used to close the loop: The input for the first module in the loop (i.e. the renderer) is taken from the FIFO, while the last module of the loop writes its output to the FIFO. To initialise such a loop, either the first process must generate the initial output without input, or the last module must generate the first output without input.

Details on the implementation of the sensory-motor interface module and results for experiments with this software framework are presented in chapter 5.

3.6 Summary

The tools presented in this chapter enable the analysis of the visual behavioural control of the blowfly using naturalistic stimuli. The work flow starts by analysing a video recording of a behavioural experiment quantitatively using the described computer vision system. The resulting trajectory can be used to reconstruct what the fly has seen during the behaviour with the computer graphics module. By the FliMax stimulation device the reconstructed image sequence is displayed to

---

[2] Unix-pipes are a operating system concept: When processes A is coupled to process B via a pipe, the standard output of process A is used as the standard input of process B by the operating system.

[3] The command-line interfaces to the Unix operating system is called "shell".

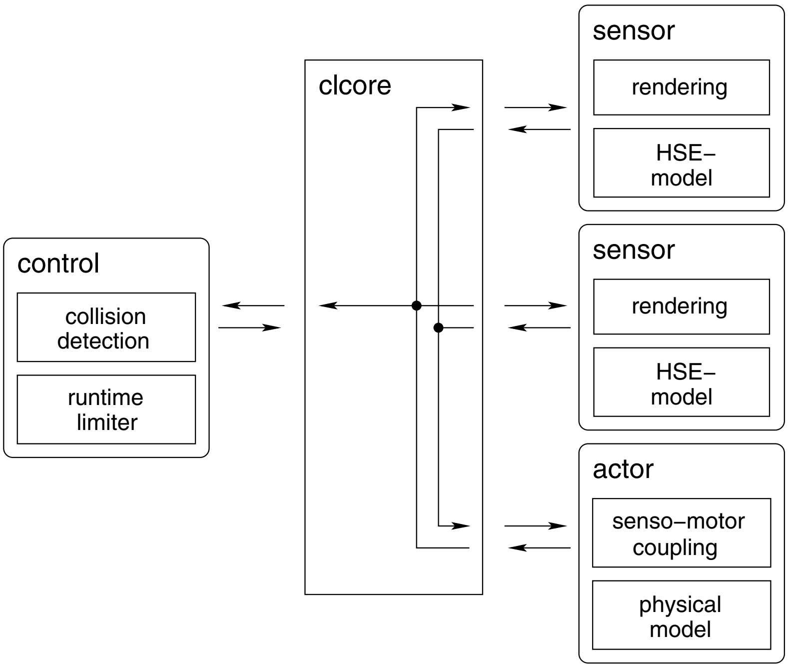

Figure 3.22: The structure of the clcore-program implementing a framework for closed loop simulation of a sensor/actor loop. Clcore initialises the system by starting several child processes and controls the data flow between these processes. In each time-step, several sensors get the momentary position in the simulated environment. Based on this, the sensor signals are computed by external processes, collected by clcore, and passed to an actor process and a control process. The actor updates the environmental position while the control process checks for stop conditions like collisions with the environment or time out events. Comuncation between the processes is done via Unix pipes.

another fly while the neuronal responses are recorded and can be analysed later on. Alternatively, the wingbeats of a tethered flying fly in response to these images can be recorded by the described wingbeat analyser with the current limitations discussed above. Hypotheses derived from this analysis can then be tested for sustainability by closed-loop simulation of a virtual fly in the closed-loop simulation framework.

Recent results obtained by replay of behaviourally generated optic flow in the FliMax were already cited in section 2.4. Another experimental study using the computer vision system described above to analyse free flight behaviour under open-air conditions and the FliMax for replay of the stimuli was published by Boeddeker et al. (2005). Results from a closed-loop simulation experiment are discussed in chapter 5. The experiments using the wingbeat analyser were unsuccessful for reasons discussed above. However, they showed that the technique is generally applicable to blowflies and no principle problem arose that would prevent further refinement of this approach.

4 Model

For many animals including humans the optic flow generated on the eyes during locomotion is an important source of information about self motion and the structure of the environment. The blowfly has been used frequently as a model system for experimental analysis of optic flow processing at the micro-circuit level. This chapter describes a model of the computational mechanisms implemented by these circuits in the blowfly motion vision pathway. While this model was originally proposed on the basis of simple experimenter-designed stimuli, it is shown below that it is also capable to quantitatively predict the responses to the complex dynamic stimuli a blowfly encounters in free flight. In particular, the model visual system exploits the active saccadic gaze and flight strategy of blowflies in a similar way as does its neuronal counterpart (see section 2.4). The model circuit extracts information about translation velocity in the inter-saccadic intervals and thus, indirectly, about the three-dimensional layout of the environment. Stepwise dissection of the model circuit reveals, which of its components are essential for these remarkable features. When accounting for the responses to complex natural stimuli the model is much more robust against parameter changes than when explaining the neuronal responses to simple experimenter-defined stimuli. In contrast to conclusions drawn from experiments with simple stimuli, optimisation of the parameter set for different segments of natural optic flow stimuli do not indicate pronounced adaptational changes of these parameters during long-lasting stimulation.

Locomotion generates complex patterns of retinal image movements, the so-called optic flow (see section 2.1). In blowflies, the neuronal computations underlying optic flow processing have been analysed in great detail: The outputs of local motion sensitive elements are spatially pooled by large-field neurons, the so-called tangential cells (TCs) that respond best to different patterns of optic flow (reviews: Borst and Haag, 2002; Egelhaaf et al., 2002; Egelhaaf and Warzecha, 1999; Hausen, 1984; Krapp et al., 2001). One particular TC, the HSE-cell, is commonly assumed to encode yaw rotations of the animal and to be involved in the control of visually guided behaviour (Haag et al., 1997; Hausen, 1982a,b; Horstmann et al., 2000; Krapp et al., 2001).

In free flight blowflies execute series of saccadic turns with angular velocity peaks of up to several thousand degrees per second; between saccades the gaze is

---

Text and figures of this chapter were previously published in similar form in Lindemann et al. (2005).

kept rather stable (Schilstra and van Hateren, 1999, 1998b; van Hateren and Schilstra, 1999). As a consequence of this saccadic gaze strategy the rotational optic flow component is essentially squeezed into the saccades and can thus be separated from the translational component. Hence, if HSE would act also for natural stimuli as a sensor for yaw-rotations, it should encode mainly the time course of saccadic turns.

Using behaviourally generated optic flow as visual stimuli, recent electrophysiological experiments showed that during saccades the system operates far beyond this linear range. The angular velocity of retinal image motion nevertheless can be reconstructed faithfully from the responses of TCs if the velocities and velocity changes are relatively small (Bialek et al., 1991; Egelhaaf and Reichardt, 1987; Haag and Borst, 1997). Moreover, HSE was concluded to encode behaviourally relevant information between saccades where the translational optic flow dominates at low frequencies (Kern et al., 2005b). In the inter-saccadic intervals HSE provides rich information about translational optic flow and thus, indirectly, about the spatial layout of the animal's surroundings. These results stress that the functional significance of neuronal mechanisms can only be assessed when the system is analysed under natural operating conditions.

The mechanisms underlying visual motion computation have been accounted for by an algorithmic model. Local motion detectors of the correlation type are spatially pooled by integrating elements meant to represent the motion sensitive TCs, such as HSE (reviews: Borst and Egelhaaf, 1989, 1993a; Egelhaaf and Borst, 1993). Although various elaborations of the basic model of the blowfly motion pathway can explain the neuronal responses to conventional experimenter-defined motion stimuli (Borst et al., 1995; Harris and O'Carroll, 2002; Reisenman et al., 2003), it is not obvious, whether these models are also sufficient to explain the neuronal responses to complex natural optic flow. The properties of blowfly TCs were shown to change as a result of stimulus history (Borst et al., 2003; Harris et al., 1999a,b; Maddess and Laughlin, 1985; Reisenman et al., 2003), which further complicates the analysis of responses to natural optic flow.

As a new challenge for the model of blowfly motion vision, natural optic flow is used as stimulus for this analysis. The intention is to find out whether the model still can be regarded as a viable basis for explaining visual motion computation.

4.1 Model structure and analysis methods

The following sections introduce the algorithmic structure of the model and discuss the relevant parameters and their initial setting. Methods for the analysis of the simulated data and the comparison to their electrophysiological measured counterparts are also described below.

4.1.1 Spatial eye model

The input images of the visual motion pathway are sampled by Gaussian shaped spatial low-pass filters ($\sigma = 2^\circ$). The output of these filters form the input to the photoreceptors that are equally spaced at 2° along the elevation and azimuth[1] of the eye. The array of photoreceptors forms a rectangular grid in the cylindrical projection with 51 rows and 86 columns. The model visual field covers $-50^\circ \leq \varphi \leq 120^\circ$ in azimuth and $-50^\circ \leq \theta \leq 50^\circ$ in elevation for the right HSE. For the left HSE the mirrored input field covers $-120^\circ \leq \varphi \leq 50^\circ$ in the azimuth. Zero degrees correspond to the frontal equatorial direction. Receptive fields of HSEs include contralateral input conveyed by spiking TCs (Hausen, 1984). This geometry of the receptor array represents only a rough approximation to the retinal mosaic found in flies (Petrowitz et al., 2000).

4.1.2 Model of the spatio-temporal processing

The model of the spatio-temporal processing done by the blowfly motion vision pathway can be subdivided into three functional modules. The first module pre-processes luminance changes at the input by elements corresponding to the photoreceptors and their postsynaptic elements. The second module is built by local elementary motion detectors that are fed by the pre-processed luminance signals. In the third module, the motion detector outputs are weighted and spatially pooled by elements corresponding to the dendrites of TCs. For each of these modules, several different model elaborations were proposed in the literature or will be proposed here.

Peripheral pre-processing

The temporal properties of the peripheral elements are modelled in two different ways (figure 4.1a,b).

In the basic model, the photoreceptors and the second-order neurons, the so-called Large Monopolar Cells (LMCs), are jointly modelled as a single first-order linear low-pass filter with a fixed time constant of $\tau_p = 8$ms, approximating the corner frequency measured for the response of blowfly photoreceptors to white noise luminance fluctuations (Juusola et al., 1995; van Hateren and Snippe, 2001). The output of this low-pass filter is inverted to account for a sign inversion observed between the signals of photoreceptor and LMC (Laughlin, 1994).

---

[1] The position of a point on a sphere can be described by giving two angles and the radius of the sphere (spherical coordinates). In the biological literature these angles are the called elevation (vertical angular deviation in the from the equator of the sphere) and azimuth (horizontal position in projection on the equator).

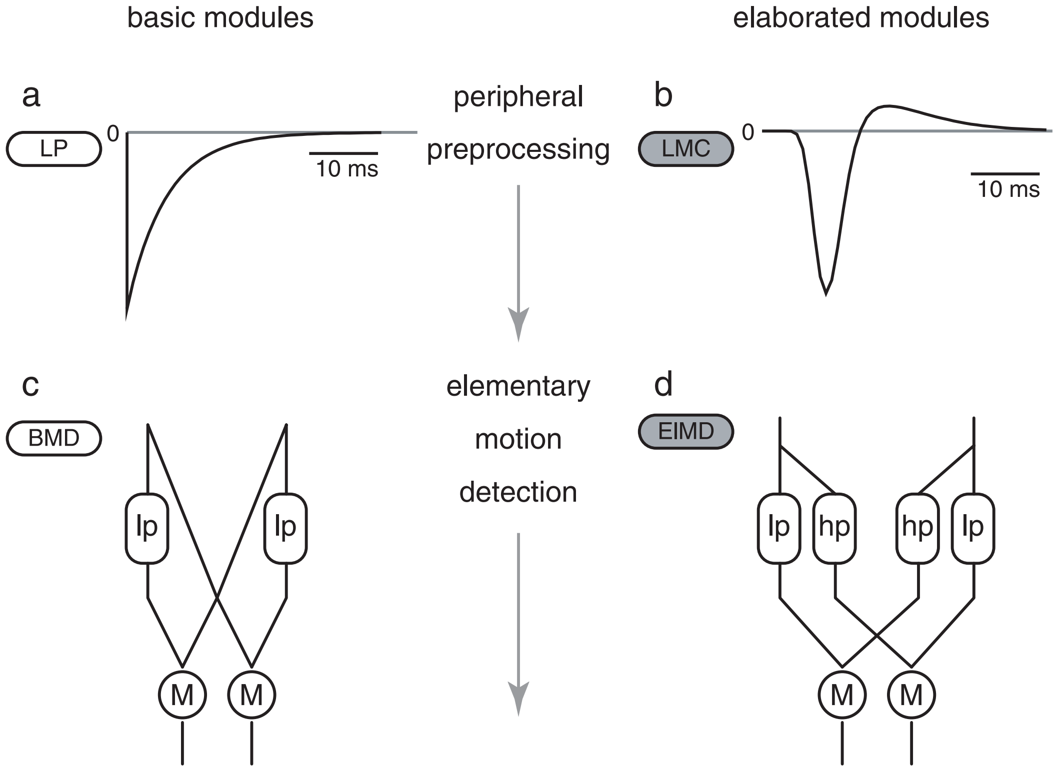

Figure 4.1: Schematic of the model of the peripheral parts of the visual motion pathway of the blowfly in the basic and elaborated variation. The basic modules are labelled by white boxes, their elaborated counter parts by grey ones. (a) Impulse response of the low-pass filter approximating the dynamical properties of the photoreceptors, (b) impulse response of the LMC/photoreceptor linear filter, (c) the basic correlation type motion detector (lp: first-order linear low-pass filter, M: algebraic multiplication), (d) the high-pass filter elaboration of the motion detector (hp: first-order high-pass filter).

Figure 4.1a shows the impulse response of this filter:

$$h_p(t) = -\frac{1}{\tau_p} e^{\frac{-t}{\tau_p}} \tag{4.1}$$

This peripheral module will be called "LP" throughout this paper. All linear filters were modelled by stepwise discrete integration of the differential equations describing their temporal properties. For the low-pass filter this leads to the recursive implementation

$$l(x_t) = l(x_{t-1}) + \frac{1}{\tau}(x_t - l(x_{t-1})) \tag{4.2}$$

with l the output of the filter, x_t the input at timestep t. $l(x_0) = 0$ is used as initial value.

As an elaboration of the peripheral temporal filtering, a linear filter kernel derived from a white-noise analysis of the LMCs of the fly was applied (module called "LMC" below and in figures). The filter kernel shown in figure 4.1b was defined by (James, 1990) as

$$h_{lmc}(t) = a_1 \exp(\frac{-(ln(\frac{t}{\tau_1}))^2}{2\sigma_1^2}) + a_2 \exp(\frac{-(ln(\frac{t}{\tau_2}))^2}{2\sigma_2^2}), \tag{4.3}$$

where $a_1 = 1.06, \tau_1 = 12$ms$, \sigma_1 = 0.197, a_2 = 0.167, \tau_2 = 21ms, \sigma_2 = 0.345$. For these values the function qualitatively fits the linear component of the blowfly LMC response as measured by (Juusola et al., 1995) at approximately the brightness conditions of the electrophysiological analysis (Kern et al., 2005b). In the model implementation, the first 50ms of this kernel were sampled with a sampling frequency of 1kHz and applied to the brightness values by discrete convolution.

Elementary motion detectors

For the basic model, the elementary motion detectors are simple correlation-type motion detectors composed of a first-order linear low-pass filter and an arithmetic multiplication of the low-pass filtered signal originating from one photoreceptor and the unfiltered signal originating from a neighbouring horizontally displaced photoreceptor. The motion detector consists of two mirror symmetrical subunits (basic motion detector "BMD", see figure 4.1c). The time constant of the temporal low-pass filter in the basic motion detector was set initially to $\tau_{lp} = 35$ms to get a steady-state velocity tuning of the simulated TC with an optimum at 5Hz temporal frequency (the quotient of angular velocity and spatial wavelength of the stimulus pattern), matching the previously described steady-state properties of HSE (Hausen, 1982a).

An elaborated version of the motion detector circuit (elaborated motion detector "ElMD") incorporates a first-order linear high-pass filter (impulse response

$$h(t) = \delta(t) - \frac{1}{\tau_{hp}} e^{\frac{-t}{\tau_{hp}}}), \tag{4.4}$$

with $\delta(t)$ a Dirac pulse at $t = 0$) into the second input branch of the multiplier O'Carroll et al. (figure 4.1d, 1997). The discrete implementation of the high-pass filter is

$$h(x_t) = x_t - l(x_{t-1}) \tag{4.5}$$

with h the filtered signal, x_t the filter input at timestep t, and $l(x_t)$ the lowpass filter defined in equation 4.2.

This elaboration was previously shown to account for a better fit of transient responses to a motion step. It also allows for an elegant mechanism of adaptation by dynamically adjusting the high-pass time constant (Borst et al., 2003).

Local sensitivities

The weights of the different movement detectors that subserve the visual field are set according to the spatial sensitivity distribution of the HSE-cell. More precisely, the weight field for the spatial integration is determined by a two-dimensional Gaussian function (equation 4.6; figure 4.2a, shown for the right HSE only) fitted to the local sensitivity distribution of HSE (Krapp et al., 2001). For the retinal positions given by the eye model, the sensitivity weights are computed as

$$w(\varphi,\theta) = \begin{cases} e^{-(\frac{1}{\sigma_\theta}\theta)^2} e^{-(\frac{1}{\sigma_{\varphi+}}(\varphi-\varphi_c))^2} & \text{if} \quad \varphi > \varphi_c, \\ e^{-(\frac{1}{\sigma_\theta}\theta)^2} e^{-(\frac{1}{\sigma_{\varphi-}}(\varphi-\varphi_c))^2} & \text{otherwise,} \end{cases} \tag{4.6}$$

where φ denotes the azimuth and θ the elevation angle. The receptive field centre is on the eye's equator ($\theta = 0$) at $\varphi_c = 15°$ for the right and at $\varphi_c = -15°$ for the left HSE. The angular width of the receptive field is defined for the elevation by $\sigma_\theta = 33°$ and for the azimuth by $\sigma_{\varphi+} = 102°, \sigma_{\varphi-} = 45°$ for the right HSE. For the left cell the values are interchanged ($\sigma_{\varphi+} = 45°, \sigma_{\varphi-} = 102°$). Note that the contralateral input is conveyed to HSE via spiking TCs from the contralateral eye (Hausen, 1984). Calculating the contralateral input in the way described here, is a simplification of this circuit, ignoring the nonlinearities introduced by the spike generation. Since the contralateral input of HSE is much weaker than the ipsilateral one (Hausen, 1982a; Krapp et al., 2001) this simplification is regarded appropriate for the current purposes.

Spatial pooling

In the basic model, the spatial pooling corresponding to the dendritic tree of the HSE-neuron is modelled as a linear weighted summation of the elementary motion detector outputs (linear integration "LIN", figure 4.2b). The outputs of

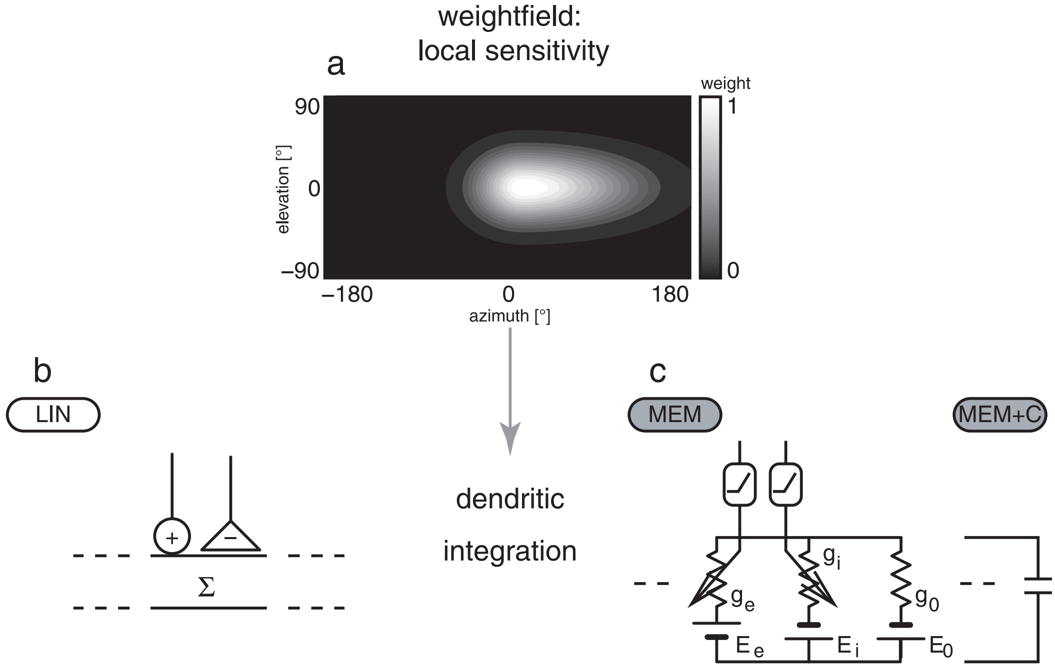

Figure 4.2: Schematic of the spatial integration modules of the model. (a) The weight field of the local sensitivity distribution of the right model HSE (contour plot in cylindrical projection; brighter areas indicated greater sensitivities) is the same for all model variations; left HSE mirror symmetric, (b) linear dendritic summation of positive and negative detector output, (c) circuit representation of the more elaborated passive membrane model (g_0:leak conductance of the pooling neuron, g_e, g_i: excitatory and inhibitory synaptic conductances driven by the output of the multiplication after rectification, E_0, E_e, E_i: corresponding reversal potentials).

the mirror symmetrical subunits of the movement detectors are subtracted from each other.

$$V_m^{LIN} = s_e - s_i \tag{4.7}$$

where

$$s_x = \sum_{\varphi,\theta} w(\varphi,\theta) m_x(\varphi,\theta) \tag{4.8}$$

are the weighted sums of the outputs m_e, m_i of the motion detector subunits.

As an elaboration, the summation of the outputs of the two types of motion detector subunits are interpreted as the conductances of excitatory and inhibitory synapses on the integrating cell (Borst et al., 1995). The resulting membrane potential of the integrating element is calculated by the electrical equivalent circuit of a one-compartment passive membrane patch ("MEM", figure 4.2c).

$$V_m^{MEM} = \frac{g_0 E_0 + g_e E_e + g_i E_i}{g_0 + g_e + g_i} \tag{4.9}$$

E_0 denotes the resting potential of the cell, E_e, E_i denote the reversal potentials of the excitatory and inhibitory synapses, respectively, g_0 indicates the leak conductance of the membrane, g_e, g_i indicate the conductances of the excitatory and inhibitory synapses (figure 4.2c).

For further simplification of equation 4.9, the resting potential of the model neuron is set to $E_0 = 0$mV. This setting does not change the relative fluctuations of the membrane potential. g_e, g_i are given by the summated outputs of the two types of motion detector subunits after weighting them according to spatial sensitivity distribution of HSE (see above). The leak conductance g_0 and the ratio of the synaptic reversal potentials $\frac{E_i}{E_e}$ are free parameters of the model. These two parameters were determined by an optimisation procedure (see section 4.1.2).

A further type of nonlinearity is introduced to the model (system) by the transfer characteristics of the synapses between movement detector output and integrating element. The postsynaptic conductances are calculated as

$$g_x = \sum_{\varphi,\theta} w(\varphi,\theta) r(m_x(\varphi,\theta)), \tag{4.10}$$

where $r(x)$ is the synaptic transfer function. For the present analysis, the synapses are assumed to have rectifying characteristics:

$$r(x) = \begin{cases} x, & \text{if} \quad x > 0 \\ 0, & \text{otherwise.} \end{cases} \tag{4.11}$$

The multiplication stage of the detector subunits of the elaborated version of the motion detector (ElMD) can have both positive and negative outputs, because the high-pass filter removes the constant positive offset of the input signals resulting from the mean luminance of the stimulus. Thus, both positive and negative values are present at the input of the multiplier. As a consequence of the rectification nonlinearity (equation 4.11) these negative values cannot lead to negative postsynaptic conductances g_e, g_i in the postsynaptic neuron, too. Negative values would cause numerical problems if the denominator of equation 4.9 gets close to zero.

The integrating neuron has also temporal filtering properties (MEM+C). The membrane capacitance C_m of the neuron and the input resistance

$$R_{in} = \frac{1}{g_{in}} = \frac{1}{g_0 + g_e + g_i} \tag{4.12}$$

form a low-pass filter which can be approximated by a first-order linear low-pass filter (Koch, 1999). g_{in} represents the overall input conductance of the integrating model cell, g_0 the leak conductance, g_e and g_i the conductances controlled by the excitatory and the inhibitory detector subunits, respectively. The corner frequency of this low-pass filter depends on the input resistance and the membrane capacitance of the cell. The input resistance is the sum of the leak conductance of the cell and the synaptic conductances. With the synaptic conductances varying in time, the input conductance and thus also the corner frequency

$$f_{TC} = \frac{1}{\tau_{TC}} = \frac{1}{R_{in} C_m} \tag{4.13}$$

depends on the presynaptic input. Without synaptic input, the corner frequency is minimal, the input resistance drops for any synaptic input. The lower bound for the corner frequency is

$$f_0 = \frac{1}{\tau_0} = \frac{g_0}{C_m} \tag{4.14}$$

The membrane capacitance can thus be calculated from the minimal corner frequency as

$$C_m = \tau_0 g_0 \tag{4.15}$$

Thus, the corner frequency of the neuron with a given synaptic input (equation 4.13) can be rewritten to

$$f_{TC} = \frac{1}{\tau_{TC}} = \frac{g_0 + g_e + g_i}{\tau_0 g_0}, \tag{4.16}$$

eliminating the explicit occurrence of C_m from equation 4.13.

Optimisation of both parameters with respect to the difference function d_{rms} (defined in section 4.1.6) by systematic variation leads to $\tau_0 = 30ms$ and $g_0 = 1100$ (dimensionless for reasons discussed below). The average difference between model and experimental data is $d_{rms} = 2.83$mV. During stimulation with behaviourally generated optic flow the corner frequency is much lower, however varies only little as a function of the input resistance ($\tau_{TC} = 12.1 \pm 5.9$ms, mean standard deviation). The value of the corner frequency during motion stimulation has the same order of magnitude as the for time constant of 1.82ms measured for the HSE neuron by (Borst and Haag, 1996). Note, however, that the cell is modelled here as a one-compartment neuron, although the cell may have different passive properties in the dendritic and the axonal regions.

Since the model performance improves only slightly by introducing a variable corner frequency, the properties of this filter are for convenience approximated by applying to the integrated signal a first-order low-pass filter with a constant corner frequency.

Parameter settings

For all model versions, several parameters were optimised by stepwise variation to fit the model HSE response to the natural, i.e. behaviourally generated stimuli. The time constants of the temporal filters in the motion detector ($\tau_{lp}, \tau hp$) were optimised first. For the optimal parameterisation of the motion detectors, the leak conductance (g_0) and the ratio of the synaptic reversal potentials ($\frac{E_i}{E_e}$) of the nonlinear spatial integration model, as well as the time constant of the low-pass filter of the integrating element (τ_{TC}) were subsequently optimised. Because neither the number nor the typical conductance change of the input synapses are easily measurable, the leak conductance g_0 can be parameterised only with arbitrary units, the values given below depend on the scaling of the input conductances and the number of modelled input channels chosen. However, the input resistance of HSE typically measured in electrophysiological experiments lies in the range of 5MΩ (Borst and Haag, 1996).

The optimal parameter settings for the elaborated model are $\tau_{lp} = 10$ms, $\tau_{hp} = 60$ms, $g_0 = 500$, $\frac{E_i}{E_e} = -0.95$, $\tau_{TC} = 8$ms. Here a parameter set is regarded optimal when it minimises the difference measure defined below. It was also counterchecked that the optimal setting for the time constants does not depend on the parameterisation of the integrating neuron.

4.1.3 Stimuli

Free-flight data recorded by (Schilstra and van Hateren, 1999; van Hateren and Schilstra, 1999) were used to generate the optic flow stimuli used in this analysis. The data were recorded using miniature coils attached to the head of a blowfly flying in a cubic flight arena. Based on these data, on the spatial layout of the flight arena and on the textures covering the arena walls, the retinal image sequences were reconstructed by computer graphics at a temporal resolution of 1000Hz for the model simulations and 370 Hz for the electrophysiological experiments (for details on stimulus generation see chapter 3).

4.1.4 Electrophysiological Data

The reconstructed optic flow was replayed to flies using th high-speed panoramic display device FliMax (for details see section 3.3) and the resulting neuronal responses of HSE-neurons were recorded intracellulary. Three different flight trajectories were used. The input of the mirror symmetrical contralateral HSE-cell was simulated by presentation of mirrored versions of the stimuli. For the resulting 6 stimuli, between 12 and 35 sweeps of data were recorded.

The HSE-neuron responds to image motion with graded membrane potential changes superimposed by action potentials (Haag et al., 1997; Hausen, 1982a,b). The graded potentials are thought to represent the postsynaptic signals in the HSE-cell as corresponding to the pooled outputs of the local motion detectors in the model. Therefore, the action potentials were attenuated in the electrophysiological data - which are not generated by the model - by applying a Gaussian convolution mask ($\sigma = 2$ms) to the individually recorded signals. From the resulting low-pass filtered responses an average over sweeps was calculated for each stimulus (example for the averaged data shown in figure 4.3). The model in its current version does not include neuronal noise. Therefore the model responses will be compared to the averaged neuronal responses, because these reflect best the stimulus-induced response component by averaging out signal components that are not related to the stimulus.

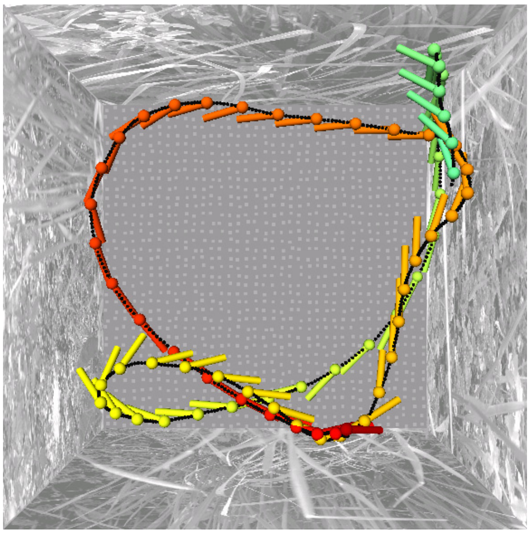

Figure 4.3: Example flight path and 3D-model of the experimental setup of a behavioural recording, from which the optic flow was reconstructed. Colour code of flight time: red (start) to green (finish). The model-texture was reduced in contrast for printing. Figure from Kern et al. (2005b).

4.1.5 Steady-state stimuli

To evaluate the model responses to classical stimuli, constant velocity stimuli were generated by virtually rotating the model for one second at a constant velocity in a cylindrical setup covered with a sinusoidal pattern (spatial wavelength $10°$). Like the HSE-cell, the model responds to such a stimulus with a transient response followed by a mostly constant reaction. The level of this so-called steady-state was computed as the mean over the last 500ms of this period.

4.1.6 Difference measure

To quantify the difference between neuronal and model responses, the root mean squared difference of the signals was used.

The model does not contain all latencies present in the neuronal system but mostly the phase shifts introduced by the various temporal filters. Only the filter kernel used for the simulation of the temporal properties of photoreceptor and LMC introduces a true latency. Therefore, a temporal shift of the model response was introduced to correct for the latency. The size of this shift was determined for each model variant by cross-correlation of the neuronal and model signal.

Since the model response is not automatically scaled to the physiological range of membrane potentials, it was scaled by a factor f that minimises the mean squared difference between the temporally shifted model responses $m(t)$ and the electrophysiological signals $e(t)$.

$$d_{rms} = \sqrt{\frac{1}{N}\sum_{i=1}^{N}(e(t_i) - fm(t_i))^2}, \tag{4.17}$$

where

$$f = \frac{\sum_{i_1} Ne(t_i)m(t_i)}{\sum_{i_1} Nm(t_i)^2}. \tag{4.18}$$

For a given combination of model parameters, typically f varies by approximately 10% of its value across the responses to different stimuli.

To assess the inter-trial variability of the cellular responses, the square-root of the squared difference between the individual response traces (with spikes removed as described above) and the average electrophysiological response is calculated. This inter-trial difference is on average $d_{rms} = 2.6 \pm 0.8$mV (mean ± standard deviation).

4.1.7 Saccade-triggered average responses

An interesting qualitative feature of the behavioural data are the sharp saccadic changes in gaze approximately every 100ms (Schilstra and van Hateren, 1999; van Hateren and Schilstra, 1999). Therefore, the prototypic responses of both the electrophysiological and the model data to the saccadic yaw velocity was calculated. To do that, local maxima and minima above a threshold of $400°$s^{-1} in the yaw velocity trace were localised. Segments lasting from 50ms before and 100ms after the maximum were aligned with respect to their maxima and averaged across trials. These prototypic event-triggered average responses serve as a qualitative benchmark for the model performance.

4.1.8 Coherence analysis

The coherence between two signals is a frequency-dependent measure of the linearity of the relation between these signals. A coherence of $\gamma^2 = 1$ means that one signal can be constructed perfectly from the other signal with a linear filter. Lower values indicate noise or a nonlinear relationship between the signals. As in the experimental analysis by Kern et al. (2005b), the coherence for the model and the neuronal data for the inter-saccadic segments of the responses was calculated.

Masking out saccades

Masks selecting saccadic segments in stimulus and response were obtained by gating a region surrounding saccades. Like the segments used for the saccade triggered averages the masks were centred on the peaks in the total angular velocity of the head during a saccade. The region was large enough to include all parts of both saccadic stimulus and corresponding response. Saccades that were close together were merged to reduce boundary effects. Edges of the masks were tapered with a 12.5ms $\cos^2$-taper to reduce spectral leakage biasing the coherence estimate at high frequencies. The inter-saccadic mask, used for suppressing the saccadic stimulus and response, equals one minus the saccadic mask. Masked data consisted of gated data intermitted with blocks of zeroes. Although the mask shapes the power and cross spectra of the masked data, this shaping occurs in a similar way for all spectra in the numerator and denominator of the definition of coherence. Consequently, the mask by itself does not generate coherence for uncorrelated data, as was checked in control computations with uncorrelated noise. The coherence of masked data include the zero blocks, and therefore should be regarded as belonging to the entire masked signal, not just to its inter-saccadic part (gated signal).

Calculation of the coherence function

Coherence between a stimulus parameter (e.g. yaw velocity) and model response was calculated according to the previous experimental study (Kern et al., 2005b) as

$$\gamma_b^2 = \frac{|P_{sr}|^2}{(P_{ss}P_{rr})}, \tag{4.19}$$

with P_{sr} the cross spectral density of stimulus and response, P_{ss} the power spectral density of the stimulus, and P_{rr} that of the response. Spectra were calculated by periodogram averaging of 50% overlapping data segments, with each periodogram the discrete Fourier transform of a $\cos^2$-tapered zero-mean data segment of 256ms, extended by zero-padding to 512ms. Results were not strongly dependent on segment length. Segments from all flights used as a stimulus for a particular cell were included in the periodogram averaging. Bias in the coherence estimate was corrected (van Hateren et al., 2002) by

$$\gamma^2 = \frac{n}{n-1}\gamma^2 - \frac{1}{n-1}, \tag{4.20}$$

with n the total number of segments.

For calculation of the model coherence, additive noise with a power density of $0.03\frac{\mathsf{mV}^2}{\mathsf{Hz}}$ was assumed, similar to the densities measured in HSE (see also Warzecha et al., 1998).

4.2 Simulation results

The model described above was evaluated to answer different questions. First, is the model response to behaviourally generated stimuli comparable to the response of the neurons? If so, which components of the model are essential? What are the optimal settings for the parameters? How critical is the choice of parameter values and how do these values compare to the parameters used to emulate the responses simpler stimulation? Finally, can the recent results on the information content of the HSE responses be reproduced by the model?

4.2.1 Performance of the model of the blowfly visual motion pathway

The responses of the basic model (modules LP-BMD-LIN) to behaviourally generated optic flow fit qualitatively the time course of the experimentally determined neuronal signals (figure 4.4a). For segments dominated by saccadic turns inducing null-direction motion (null-direction saccades; see figure 4.4a, left zoom box), the neuronal response is matched quite well by the model. The deviations of the model from the neuronal response are more pronounced in segments characterised by a more constant activation of the HSE-cell, as observed during sequences with saccades inducing preferred-direction motion (preferred-direction saccades), (figure 4.4a, right zoom box). This characteristic can be found consistently for all analysed motion sequences. The overall difference between model and neuronal responses is $d_{rms} = 5.6 \pm 0.8$mV on average. For the example segment governed by null direction saccades, the difference drops to$d_{rms} = 4.3$mV; for the example segment governed by preferred-direction saccades, the difference between model and neuronal responses goes up to $d_{rms} = 5.6$mV.

For the most elaborated model (modules LMC – ElMD – MEM+C) with an optimised parameter set for natural, behaviourally generated stimuli, the model performance is considerably better compared to the performance of the basic model (figure 4.4b). The time course of the neuronal responses is matched more closely and the overall difference between model and neuronal response drops to $d_{rms} = 2.9 \pm 0.3$mV. The most prominent improvement can be observed for segments dominated by preferred-direction saccades. The difference for the example segment shown in figure 4.4b (right zoom box) drops to $d_{rms} = 2.3$mV. For segments characterised by null direction saccades, the improvement in performance is less. For the example segment shown in figure 4.4b (left zoom box) the difference is reduced to $d_{rms} = 2.4$mV. In other response segments the fit is slightly worse resulting in the higher average d_{rms}.

In conclusion, the model of the fly visual motion pathway can account quite well for the complex time course of the neuronal responses to behaviourally generated optic flow, though fidelity depends on the model version. For the elaborated model the rms difference between model and neuronal responses is in the order of the inter-trial difference between experimentally determined neuronal responses which amounts to $d_{rms} = 2.6 \pm 0.8$mV.

4.2.2 Steady state tuning of the model

Conventionally, the steady-state velocity tuning is regarded as an important characteristic of the fly motion detection system. If the fly motion detection system is stimulated with a sinusoidal pattern moving at constant velocity, the output gets almost constant after an initial transient response (Egelhaaf and Borst, 1989; Hausen, 1982a,b). The steady-state response amplitude was found to depend on the temporal frequency of the input (the ratio of angular velocity and spatial wavelength of the stimulus pattern). It increases with increasing temporal frequency, reaches an optimum around 5Hz and then decreases again (Hausen, 1982b).

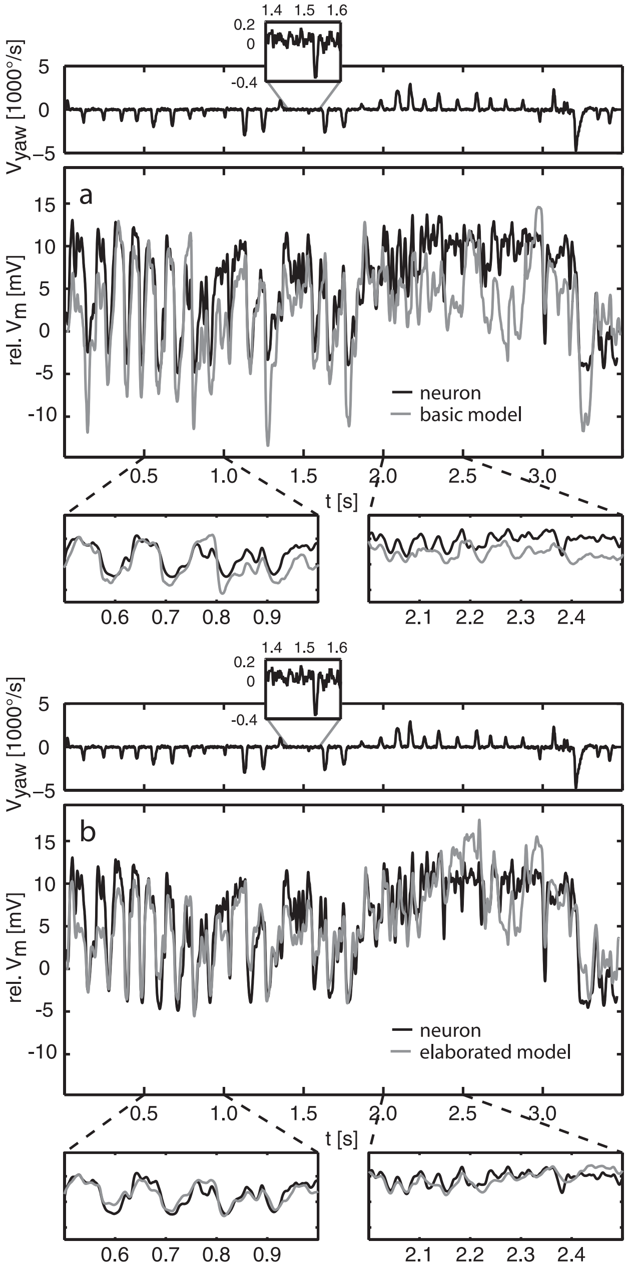

Figure 4.4: Example of a model response (grey lines) of the basic (a) and the elaborated (b) model in comparison to the neuronal response (black lines). Zoomed from the response traces are segments dominated by saccades inducing preferred (right boxes) and null direction motion (left boxes), respectively. The yaw velocity of the fly's head is shown in the traces above the response. The model response was shifted in time by 22.5 ms to correct for neuronal delays not present in the model.

Since most of the elaborations of the model of the visual motion pathway discussed below affect the steady-state velocity tuning, these effects are discussed here in some detail before looking at the results obtained for natural stimulation.

While the bell shape of the tuning curve is an inherent feature of the mechanism of motion detection, the position of the optimum of the curve is determined by the systems parameters. For the basic detector, the tuning can be computed analytically (Borst et al., 2003). Without an additional filter in the input channels, a time constant of 35ms has to be chosen to get an optimum at 5Hz (figure 4.5, black line). Additional filters in the input channels shift the optimum. A low-pass filter used for pre-filtering the retinal input shifts the optimum towards lower frequencies, a band-pass filter, such as an LMC, has the opposite effect (figure 4.5a). To recalibrate the response to a peak at 5Hz with the LMC as peripheral element, the time constant of the low-pass filter in the movement detector has to be larger than without LMC (approx. 55ms vs. 35ms). The additional high-pass filter in the elaborated detector (ElMD) has no effect on the temporal frequency optimum, if the time constants of the high-pass and the low-pass filters are equal (Borst et al., 2003). If the time constant of the high-pass filter is larger than that of the low-pass, the tuning gets broader and becomes double peaked for very large time constant differences (i.e. $\tau_{hp} >> 6\tau_{lp}$). The experimentally determined steady-state tuning of TCs is also broader than the tuning of the basic motion detector (Hausen, 1982b). In contrast, the optimal time constants found for natural optic flow in all variants of the model cause a steady-state tuning with a peak at much higher frequencies (figure 4.5b). This finding indicates that either the system properties change with the stimulus dynamics, or that some system component shaping the steady state tuning is not covered in the present model. It should be noted, however, that the difference between model and neuronal responses to behaviourally generated optic flow increases by only approximately 10-15% when the movement detector time constants is changed from the optimal values to values that also fit the experimentally determined steady-state velocity tuning (see below; figures 4.6 and 4.7c).

4.2.3 Significance of the model components

To assess which of the model elaborations are the main determinants of the model performance in response to behaviourally generated optic flow, the basic model was elaborated in various steps, eventually resulting in the most elaborated LMC – ElMD – MEM+C model. The consequences of the different model elaborations on the model performance are cumulated in figure 4.6.

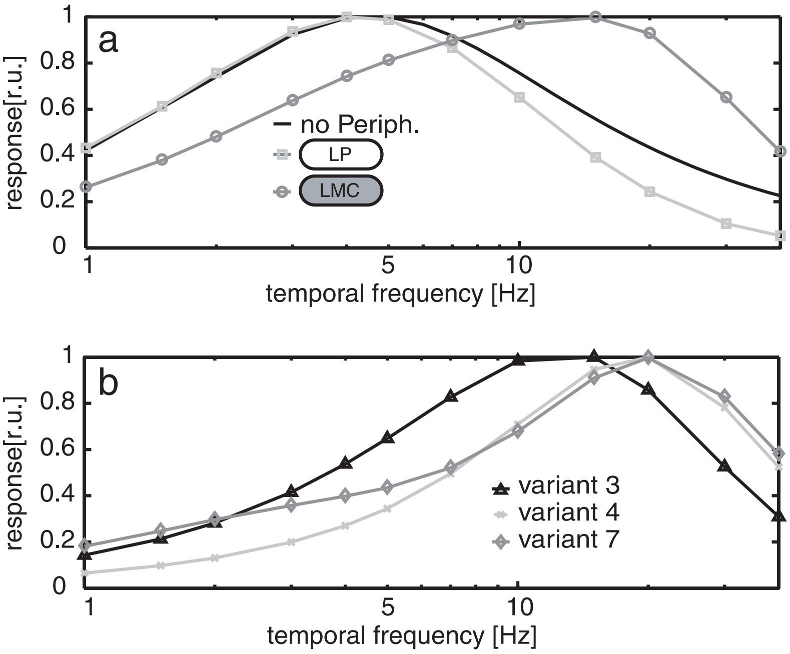

Figure 4.5: Responses of the model of the blowfly visual motion pathway to constant velocity motion and to behaviourally generated optic flow. (a) The theoretical steady-state tuning for constant velocity motion of the basic motion detector (BMD) without peripheral elements (black line), with a peripheral low-pass filter in the input line of the movement detector (LP, dark grey squares) and the LMC kernel (light grey circles). (b) The steady state tuning of optimal parameterised model variants 3 (black triangles), 4 (dark grey crosses), and 7 (light grey diamonds).

Motion detector and peripheral variants

Elaborating the motion detector with a high-pass filter does not change the model performance (ElMD) compared to the basic model, if the same filter time constants (here $\tau_{lp} = \tau_{hp} = 35$ms) are used for both filters as has been proposed previously (Borst et al., 2003) (figure 4.6, variants 1 and 2).

Optimising the low-pass filter time constant of the basic motion detector to fit the responses to natural optic flow leads to a time constant value smaller than expected from the steady-state responses (compare variants 3 ($\tau_{lp} = 10$ms) and 1 ($\tau_{lp} = 35$ms) in figure 4.6). Note that this time constant value may not strictly be the optimal one because no clear minimum in the root mean squared difference of the signals is found within the variation range (figure 4.7). Smaller values however would result in numerical problems by getting too close to the sampling interval of the simulation.

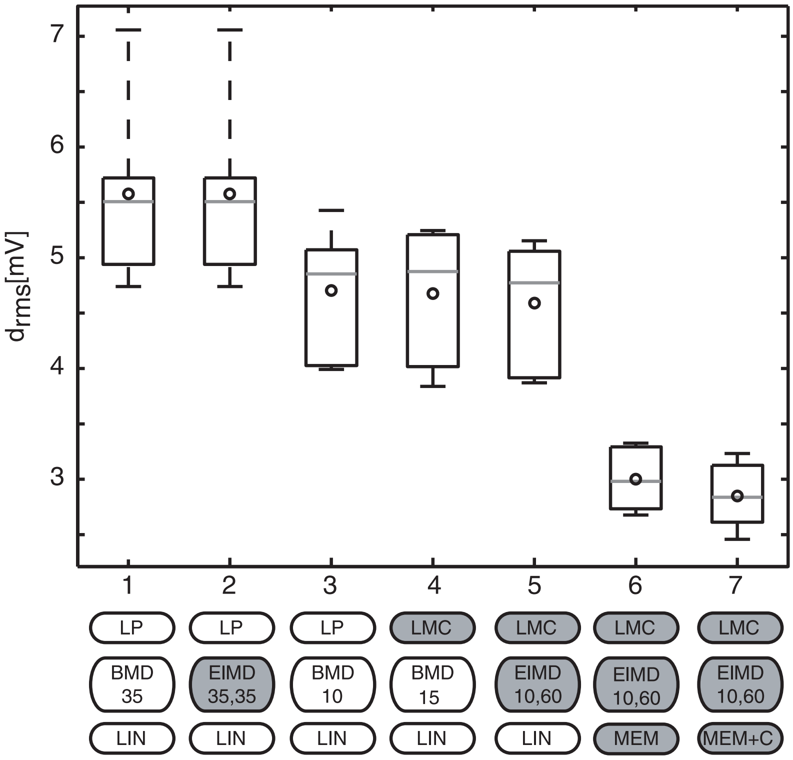

Figure 4.6: Average differences between the neuronal and the model responses for the various variants of the model. Variants shown are (using the labels from figures 4.1, 4.2, extended by the parameter(s) for the motion detector time constant(s)): (1) LP – BMD – LIN, (2)LP – ElMD – LIN, parameters match the steady-state tuning of the cell; same time constant for the motion detector low-pass and high-pass filters ($\tau_{lp} = 35$ms, $\tau_{hp} = 35$ms), (3) LP – BMD – LIN ($\tau_{lp} = 10$ms), (4) LMC – BMD – LIN ($\tau_{lp} = 15$ms), (5) LMC – ElMD – LIN, different time constants of motion detector low-pass and high-pass filter ($\tau_{lp} = 10$ms, $\tau_{hp} = 60ms$), (6) LMC – ElMD – MEM, (7)LMC – ElMD – MEM+C. For each variant, the circle indicates the mean, the horizontal lines show the median, the box includes the upper and lower quartiles, and dashed lines show maximum and minimum rms of the responses to 6 stimuli.

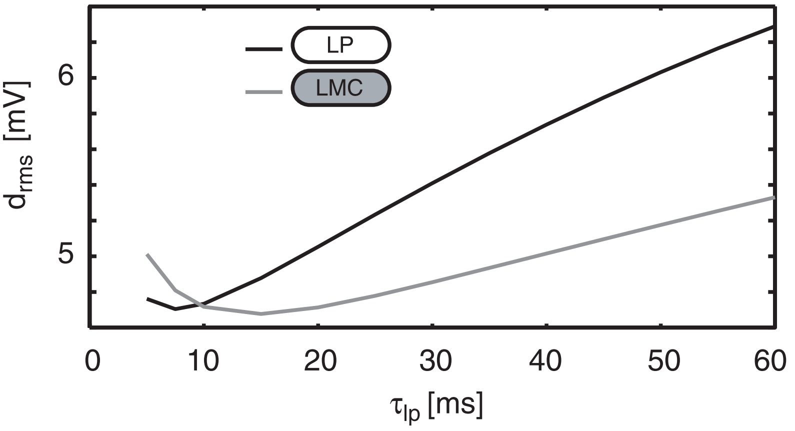

Figure 4.7: Dependency of the d_{rms} difference between model and neuronal responses on the time constant of the basic model with a low-pass in the input lines to the motion detectors (black line; variant 1 in figure 4.6) and a LMC kernel (grey line; variant 4 in figure 4.6) as peripheral element. Note the ordinate scale, indicating that within a realistic range the rms error does not depend much on the time constants.

An optimal time constant shorter than the expected one for the steady-state tuning is also obtained if the retinal input is pre-processed by the LMC filter (variant 4 in figure 4.6). Then, however, the optimal time constant of the low-pass filter in the elementary motion detector shifts to $\tau_{lp} = 15$ms consistent with the effect of the LMC bandpass characteristics observed in the steady-state case. With the optimised time constants of the movement detector low-pass filter the performance of the model improves compared to the initial parameterisation (figure 4.6, compare variants 3, 4 with variants 1,2).

Interestingly, the nature of peripheral pre-processing (i.e. simple low-pass filter or LMC) does not much affect the model performance for natural optic flow, as long as the movement detector low-pass filter is optimised for the respective type of pre-processing. However, even deviations from the respective optimal time constants by more than a factor of two affect the performance of either model only slightly (figure 4.7).

Figure 4.8 shows the dependence of the rms difference between the model and the experimentally determined responses on both the low- and the high-pass filter time constants of the elaborated detector (ElMD; average rms difference for all behaviourally generated stimulus sequences). The smallest difference is located at $\tau_{lp} \approx 10$ms and $\tau_{hp} \approx 100$ms. However, this parameter setting would lead to double-peaked steady-state velocity tuning curves of the detector. Since double-peaked steady-state velocity tuning curves have never been described for the HSE-neuron of the blowfly, although the velocity optimum is relatively broad and the temporal frequency tuning almost flat between 1Hz and 10Hz (Hausen, 1982b), we used $\tau_{lp} = 10$ms and $\tau_{hp} = 60$ms for the model response plotted in figure 4.4b. These settings lead to only an insignificantly larger difference value as compared to the combination of optimal time constants (figure 4.8).

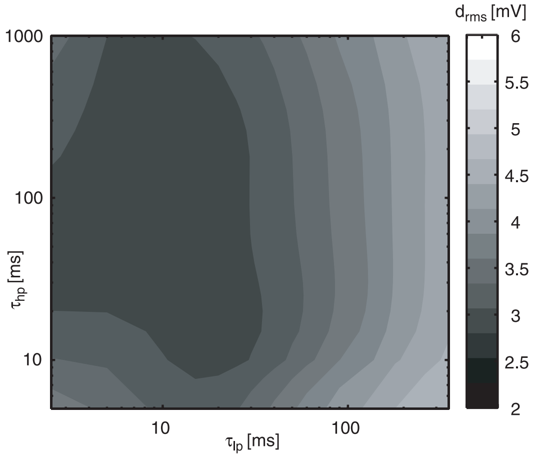

Figure 4.8: Dependency of the d_{rms} difference between model and neuronal responses on the two time constants of the elaborated motion detector. Average rms for all 6 stimuli is plotted as a contour plot.

Spatial integration

All improvements gained from elaborations in the peripheral elements and the detector time constants are small compared to the performance increments achieved by introducing into the model the non-linear spatial pooling of TCs (figure 4.6, variant 6). Introduction of this non-linearity reduces the difference between model and neuronal response to about 2/3 (figure 4.6 compare variants 5 and 6).

The optimal parameterisation of the non-linear spatial pooling was determined by systematic variation of the parameters g_0, the leak conductance of the cell, and the ratio of the reversal potentials of the negative and the positive inputs of the cell $\frac{E_i}{E_e}$ (figure 4.9). Whereas the model performance does not much depend on the leak conductance g_0, the ratio of the reversal potentials E_e and E_i has a prominent effect. The optimal ratio is $E_i = -0.95E_e$ largely irrespective of the leak conductance g_0.

For any value of $g_0 < 10^3$ the performance does not change much, but has a weak minimum at $g_0 = 500$ (figure 4.10). For this value also the dependency of the steady-state response of the model on the pattern size fits corresponding experimental results (Egelhaaf, 1985; Haag et al., 1992; Hausen, 1982b) reasonably well (figure 4.11), ensuring that the responses are relatively invariant against changes in pattern size and density. It should be noted that this gain control relies critically on the increase of the input conductance of the neuron with increasing number of activated input channels and, thus, on the relationship of the leak con-

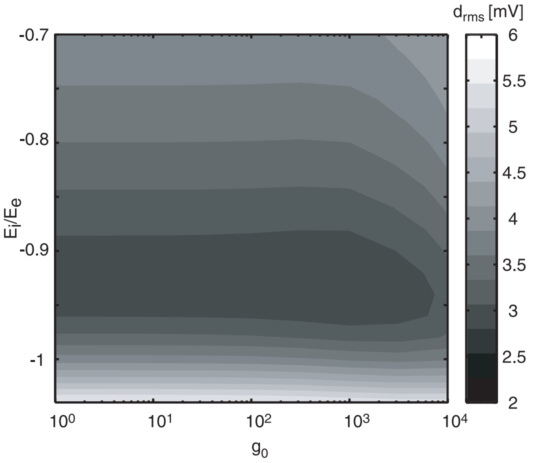

Figure 4.9: Consequences of systematic parameter variation of the membrane model of the pooling neuron. Contour plot of the rms difference between model and neuronal responses depending on g_0, $\frac{E_i}{E_e}$. Average rms of 6 stimuli is coded in grey levels.

ductance and the synaptically controlled conductances of the cells. This feature requires that the movement detector output is largely independent of the background luminance, because otherwise the background luminance dominates the synaptic conductances irrespective of whether the stimulus pattern is stationary or moving. Elimination of the effects of background luminance is accomplished in the model by either a band-pass filter in the peripheral visual system (LMC in figure 4.1) and/or a high-pass filter in one branch of the movement detector (ElMD in figure 4.1). Hence, although these two elaborations of the model of the visual motion pathway do not directly affect the model performance under natural stimulus conditions, they are necessary for the nonlinear integration at the level of the model output cell to become operative.

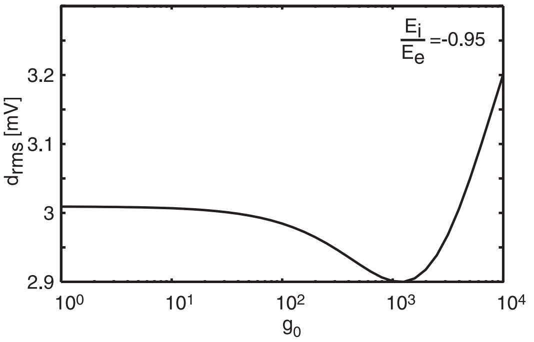

Figure 4.10: Rms difference between model and neuronal responses as a function of g_0 only, $\frac{E_i}{E_e} = -0.95$.

Temporal properties of the TCs

Post-processing of the model response by a low-pass filter improves the model performance only slightly (figure 4.6, compare variants 6 and 7). For the coherence analysis, this model component was even disadvantageous (see below).

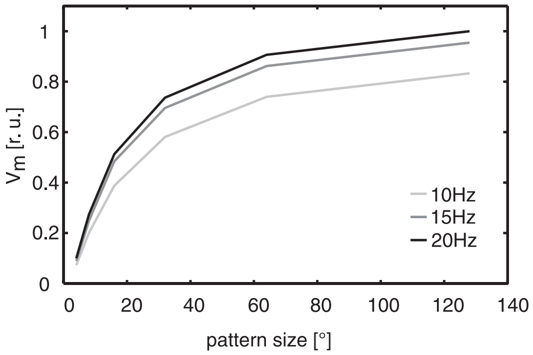

Figure 4.11: Steady-state response of the elaborated model (variant 7 in figure 4.6) as a function of pattern size hinting at the gain control properties of the model neuron (see text). Pattern modulated sinusoidally at 10, 15, and 20Hz temporal frequency, leak conductance set to $g_0 = 500$.

4.2.4 Adaptation of the visual motion pathway during stimulation with natural optic flow?

The blowfly visual motion pathway has been concluded in several studies to adapt to the prevailing stimulus conditions. This conclusion is based on experiments demonstrating that the responses to particular test stimuli, such as an instantaneous retinal image displacement, are affected by stimulus history. Part of the adaptational changes described for the neuronal responses could be explained by assuming activity-dependent changes of several model parameters (Borst et al., 2003). If motion adaptation takes place within some hundreds of milliseconds, the optimal parameter set of the model HSE-cell should change during ongoing motion stimulation. Adaptive changes during stimulation with behaviourally generated optic flow, would lead to a different optimal parameter set for the beginning and the end of neuronal responses to a stimulus trace. To check this potential consequence of motion adaptation, the parameter set of the model was optimised separately to match the initial and a later segment of the neuronal responses.

The optimal sets of filter time constants for the initial 0.5s and the last 1.5s of the 3.5s response trace did not reveal any consistent difference across stimuli. Figure 4.12a shows the average difference for all stimuli between model and neuronal response in dependence of the low- and high-pass time constants for the initial response segment, figure 4.12b displays this difference for the late response segment. Direct comparison of the optimal parameters found for segments of the individual responses to the six stimulus sequences did not reveal a consistent tendency, either (figure 4.12c). This graph only suggests a weak tendency for the low-pass filter time constant towards shorter values in the later segment.

Another adaptational effect found in TCs is a change in the response gain during ongoing stimulation (Harris et al., 2000). This effect is reflected in the model responses by an increase of the optimal scaling factor f (see section 4.1.6) between the initial and the late response segment. For an optimal fit, this factor has to be on average 20% larger for the later stimulus segment than for the first 500ms of

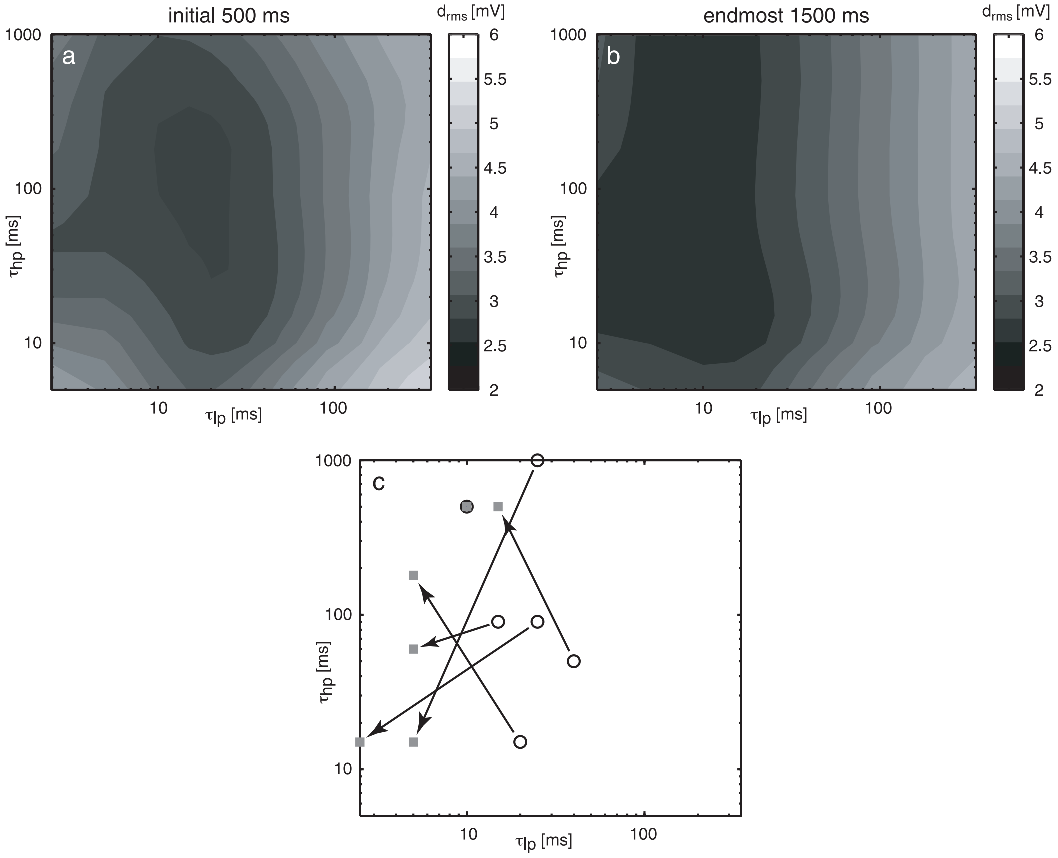

Figure 4.12: Consequences of variations of for the elaborated model (variant 7 in figure 4.6) for an early and a late segment of the stimulus trace. Average rms difference between the model and the neuronal responses to 6 stimuli is coded in grey levels for the first 0.5s (a), and the last 1.5s (b) of each stimulus. (c) Optima for the time constants obtained when the model is parameterised separately for the different stimulus sequences. Circles show the optima for the first 0.5s, crosses those for the last 1.5s of the stimulus duration. The optima for a common stimulus are connected by arrows.

the presentation. However, the fit quality for the initial segment is slightly worse than for the later segment for all stimuli even with this lower scaling factor.

4.2.5 Coding properties of the model HSE-neuron

The quantitative difference measure that was used to relate the model and the experimentally determined neuronal responses facilitates the comparison of the different model variants. A difference between the model response and the average neuronal response almost as small as the inter-trial difference of individual neuronal responses indicates a good fit of the model to the electrophysiological responses. However, even such small residual deviations between model and original responses do not necessarily imply that the model covers the important coding properties of the neuronal response. In particular, it is not clear, whether the remaining deviations are relevant with respect to what is encoded by the neuron about the animal's self-motion or the spatial relation between the fly and objects in the outside world. Therefore, two particularly relevant coding properties of the HSE-cells were selected that were recently inferred from electrophysiological responses to behaviourally generated optic flow (Kern et al., 2005b) and try to reproduce these characteristics from the model responses.

4.2.6 Responses to saccades

The first characteristic pertains to the responses of the HSE-cells to the optic flow evoked by saccades, i.e. the abrupt changes in gaze. Figure 4.13a shows the average responses of the HSE-neuron to saccadic turns into the preferred and null directions that occur during free flight. HSE responds with a transient hyperpolarisation to saccades inducing null direction motion on the retina as would be expected from a neuron encoding yaw rotations of the animal. In contrast to expectations, it does not respond with a strong depolarisation to saccades inducing preferred direction motion, but with a small drop in membrane potential following a small transient depolarisation. This behaviour is also found in the responses of the model (figure 4.13b). The responses of the elaborated model to saccades inducing null direction and preferred direction motion are remarkably similar to the corresponding neuronal response. Interestingly, already the responses of the basic model to saccades (figure 4.13c) lead to the same conclusions as the neuronal responses, although the similarity of the model to the neuronal response is slightly smaller than for the elaborated model. This finding suggests that the main reason for HSE-cells not encoding faithfully the time course of yaw rotations during saccades is the non-linear velocity encoding of the local movement detectors, rather than of the non-linear spatial pooling at the level of the tangential cells.

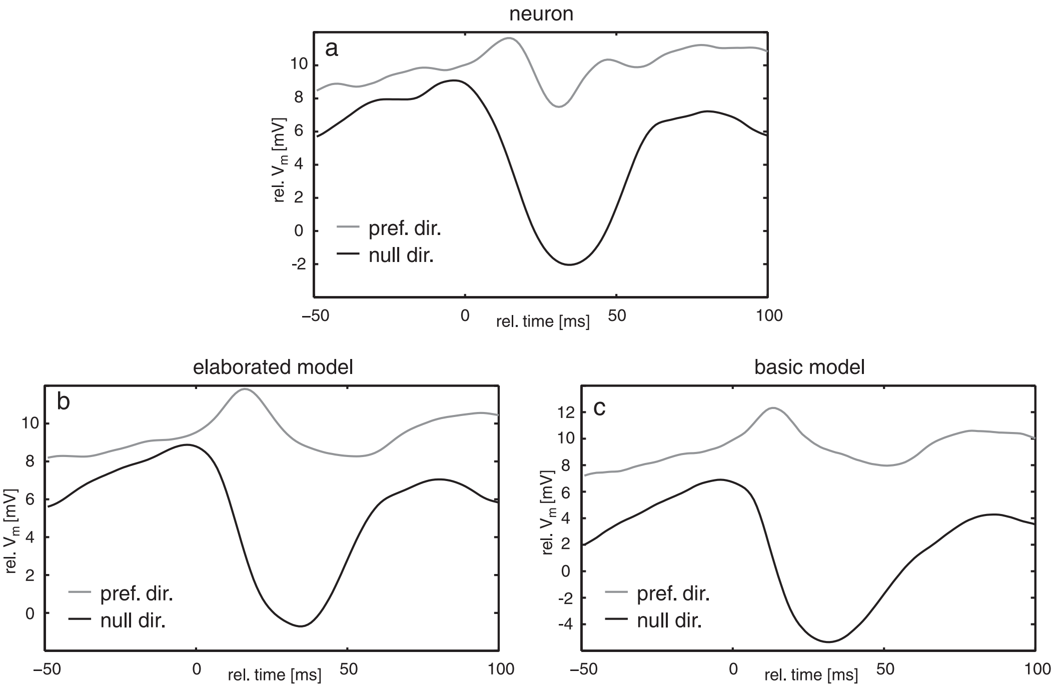

Figure 4.13: Saccade triggered averages of the neuronal data (a) in comparison to responses of the elaborated model (b) and the basic model (c). Responses to saccades inducing preferred (null) direction motion are plotted in grey (black). Experimental data taken from Kern et al. (2005b).

Coherence of the model response with self-motion parameters

The HSE-neuron shows pronounced depolarisations between saccades, although then the optic flow experienced by the eyes is much smaller than during saccades. Therefore, HSE has been concluded to encode behaviourally relevant information especially between saccades (Kern et al., 2005b). Between saccades blowflies keep their gaze stable apart from small-amplitude, broad-band yaw rotations and may thus gather useful information about the outside world from the translational optic flow components that dominate at low frequencies of the response in the inter-saccadic intervals. Indeed, this could be shown for the sideward translation by determining the optimal linear filter to estimate the time-dependent sideward velocity from the neuronal responses. How well the real sideward velocity of the blowfly corresponds to the estimated one and, thus, is reflected in the neuronal responses, is quantified by the coherence function which varies between 0 (i.e. both signals are unrelated) and 1 (i.e. perfect reconstruction). There is considerable coherence between sideward velocity and the neuronal inter-saccadic responses at low frequencies up to about 20Hz. This coherence is even enhanced when the difference signal between HSE-neurons in the right and left halves of the brain is taken into account (figure 4.14). The coherence between the inter-saccadic yaw velocity and the neuronal response is significant only at frequencies between approximately 20Hz and 60Hz (for details see Kern et al., 2005b). Applying the same analysis to the responses of the elaborated model (LMC – ElMD – MEM) leads to similar results (figure 4.14c). Since the coherence of individual neuronal responses and the different self-motion parameters was calculated in the experimental study (Kern et al., 2005b) the noise in their membrane potential fluctuations was approximated by adding to the model response individual noise traces with the variance of the noise corresponding to the experimentally determined values (see section 4.1.8). At low frequencies, the coherence between the sideward velocity and the difference response of the right and left model HSE-neuron is similar to the coherence found for the neuronal response. The coherence between yaw velocity and model response is also significant in a frequency range above 20 Hz, although it is somewhat smaller than the coherence found in the neuronal data. Hence, the elaborated model can account well for one of the most decisive coding features of real HSE-cells.

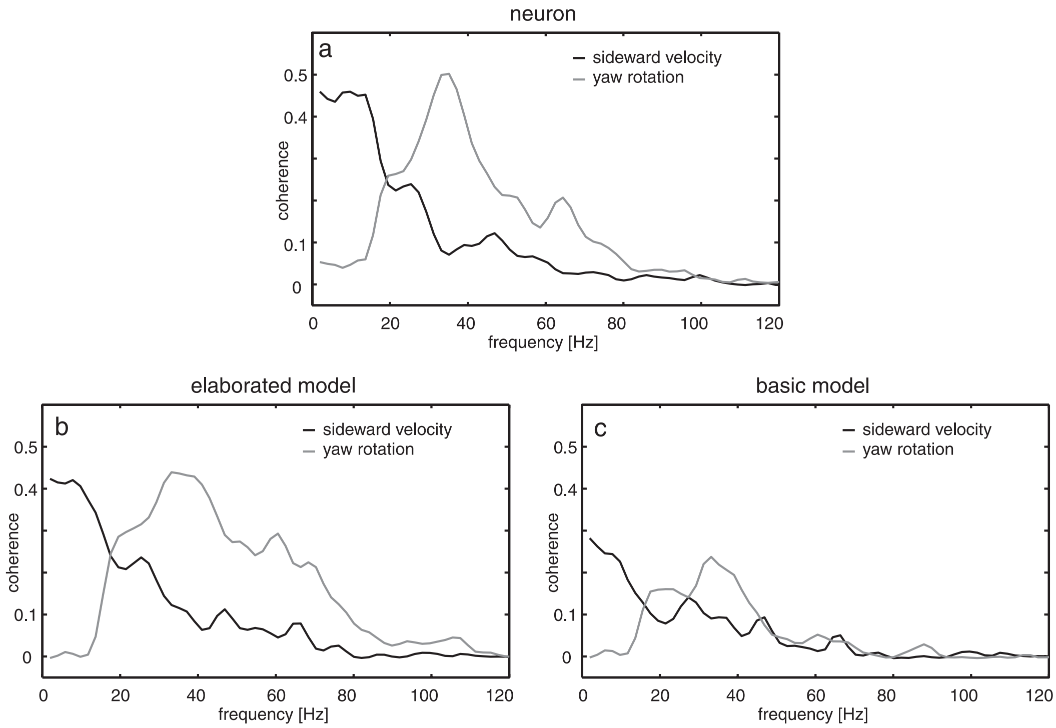

Figure 4.14: Coherence between the inter-saccadic segments of the neuronal responses (a), the responses of the elaborated model without the TC lowpass (b), and the responses of the basic model (c) to the yaw velocity[r3] (grey) and the sideward velocity (black). For the computation of the coherence, noise was added to the model responses (details see text).

The basic model generally shows significantly smaller coherences (figure 4.14b) than the elaborated model (figure 4.14c). Nonetheless, the coherences have similar frequency dependence for both model versions. Hence, the model of the fly visual motion pathway reveals, in a similar way as the experimentally determined responses, that the pair of HSE-cells represents information on both sideward and yaw velocity at the same time in adjacent frequency bands. This characteristic is rendered possible because the inter-saccadic yaw velocities are smaller by an order of magnitude than the yaw velocity during saccades. Hence, both the experimental results and the model simulations suggest that saccades should be viewed primarily as a specialisation in steering behaviour that enables the fly to extract translatory optic flow amidst rotatory optic flow. If only smooth yaw-rotations, instead of saccadic turns, were used for steering the latter would dominate stimulus and response all the time. Since the translational optic flow component depends on the distance to objects in the environment, the HSE-neurons and their model counterpart, thus, provide indirectly information about the three-dimensional layout of the environment.

4.2.7 Texture independent responses

The motion sequences that were used for the electrophysiological experiments (Kern et al., 2005b) and the model simulations shown so far are characterised by the dynamical features as are characteristic of retinal image displacements in free flight. Moreover, they were obtained in a flight arena covered with the images of natural scenes. To test how relevant the textural properties of the environment are for shaping the responses to motion sequences with natural dynamics, the textural properties of the flight arena were changed, when reconstructing the image sequences, while leaving the dynamics of optic flow unaltered. The textures on the arena walls were replaced by random dot patterns (composed of black and white squares of 1.6cm x 1.6cm) and vertical sinusoidal gratings (3.64cm per period). This analysis was motivated by the pronounced texture dependence of the steady-state responses of blowfly TCs (Eckert and Hamdorf, 1981).

The average difference between the responses of the elaborated model and the HSE-cell obtained with the natural texture and those obtained with the random dot texture are very similar. Moreover, the difference between the different model responses obtained with either wall texture is also in the same range. For sinusoidal gratings the differences are slightly larger. A noticeable qualitative difference between the response to the sinusoidal grating and to the original texture is a double peaked response to null direction saccades, similar to what was previously described for sinusoidal variation of high-velocity simple stimuli (Egelhaaf and Reichardt, 1987).

The numerical values for the comparison of HSE and model counterpart for different wall textures are given in table 4.1.

Table 4.1: Difference values for responses to differently textured stimuli

	model original	model random dot	model sine-wave
neuron original	2.9 ± 0.3mV	2.9 ± 0.4mV	4.5 ± 1.9mV
model original	–	2.6 ± 0.3mV	3.8 ± 0.9mV

The robustness of the HSE response to variations of the environmental texture was also tested in an electrophysiological control experiment where the natural texture covering the flight arena was exchanged between the different walls (Kern, personal communication). However, the predictions of the model indicate that this robustness might extend to much more pronounced changes in the textural patterns.

Taking into account that the difference measure ignores differences is scaling a small difference value may hide a pronounced difference in amplitude. However, such differences could be reduced by incorporating saturation nonlinearities in the model.

4.3 Summary and Discussion

The optic flow generated on the eyes of blowflies in free flight is characterised by peculiar dynamical properties. These are the consequence of the saccadic gaze strategy, i.e. a flight style that is characterised by rapid saccadic turns of head and body interspersed with segments of basically straight gaze (Schilstra and van Hateren, 1999; van Hateren and Schilstra, 1999). By this active vision strategy the main rotational components of the optic flow are separated from the translational components. In recent electrophysiological experiments on the motion-sensitive wide-field HSE-neuron of the blowfly it could be shown that the visual motion pathway seems to exploit the saccadic gaze strategy by extracting information about the translational optic flow components and thus about the three-dimensional layout of the environment from the inter-saccadic intervals (Kern et al., 2005b). This finding was surprising, since on the basis of experiments with conventional experimenter-designed stimuli HSE had been concluded to be a detector of yaw-rotation of the animal. This chapter shows by model simulations that the relevant features of the responses of the HSE-neuron to natural optic flow can be reproduced on the basis of relatively simple computations. In particular, the model does not encode the time course of the yaw velocity during saccades in a linear way, in contrast to the hypothesis that the HSE-cell acts as a yaw detector. Moreover, in the inter-saccadic intervals the model provides, in a similar way as the HSE-cell, information about translational optic flow. This finding suggests that the saccadic gaze strategy may facilitate the encoding of behaviourally relevant information about the spatial structure of the surrounding.

The model of the blowfly's visual motion pathway is an elaborated version of a model already proposed before on the basis of systems analysis with conventional experimenter-designed stimuli (Borst et al., 1995, 2003; Egelhaaf and Borst, 1989; Egelhaaf et al., 1989; Kern et al., 2000, 2001a). It is composed of many retinotopically arranged motion detectors extracting local motion information and the subsequent spatial pooling of their outputs. The spatial pooling stage is thought to correspond to the dendritic tree of the HSE-neuron. Starting from a basic model, various model elaborations were introduced and the consequences of these elaborations on the response to behaviourally generated stimuli were documented.

Already a very basic version of the model that linearly summates the outputs of simple versions of correlation-type movement detectors reproduces, at least qualitatively, essential features of the neuronal responses to natural optic flow. Elaborations of the basic model improve the performance. However, only small improvements are gained by introducing temporal filters in each input channel of the model to approximate the dynamical properties of the peripheral visual system. Even the introduction of an additional temporal filter into the motion detector which changes the model dynamics in response to conventional motion stimuli considerably (Borst et al., 2003) leads to only a small improvement of the response to behaviourally generated motion stimuli. In contrast, implementing the nonlinear spatial integrating properties of the HSE-neuron improves tremendously the fit of the model response to its experimental counterpart. These nonlinearities of spatial pooling, together with the opponent organisation of the output of local motion detectors, were previously discussed as the basis of a gain control mechanism that makes the responses of HSE and other blowfly motion sensitive tangential cells (TCs) relatively invariant against changes in texture size (Borst et al., 1995) and texture density (Kern et al., 2001a), while still allowing them to encode changes in pattern velocity. This gain control mechanism requires that the movement detector output is largely independent of the background luminance as is accomplished in the model by either a band-pass filter in the peripheral visual system and/or a high-pass filter in one branch of the movement detector. Hence, although these two temporal filters on their own do not directly affect the model performance under the natural stimulus conditions tested here, they are necessary for the nonlinear integration at the level of TCs to become operative.

In contrast to expectations based on results with conventional motion stimuli that the HSE-cell represents a detector for self-rotation, both the HSE-cell and its model counterpart do not represent the yaw velocity during saccades in a linear and not even in a monotonic way. In particular, saccades leading to preferred direction motion do not depolarise the cell. This characteristic feature was obtained already with the basic model and, thus, can be concluded to be a consequence of the nonlinear encoding of pattern velocity inherent to the local motion detectors when pattern velocity and accelerations get large (Egelhaaf and Reichardt, 1987; Haag and Borst, 1997). Rather than interpreting this feature as a limitation of the fly motion detection system, it can be interpreted as advantageous in the context of encoding of natural optic flow. Since during saccades the motion vision system operates beyond its linear range, it can resolve the much smaller translational optic flow component between saccades and thus provide information about the spatial layout of the environment. If the motion vision system would encode the entire angular velocity range in a linear way, the translational responses would be negligible and could hardly be resolved given the limited operating range of neurons and the noisiness of neuronal signals (review: Warzecha and Egelhaaf, 2001).

Surprisingly, the performance of the model is much less sensitive to parameter changes if confronted with complex behaviourally generated optic flow than if the much simpler experimenter-designed stimuli are employed. This leads us to the somewhat paradoxical conclusion that simple experimenter-defined stimuli may facilitate the precise estimation of system parameters, whereas, on the other hand, the precision of these parameters apparently does not matter much to account for the responses to behaviourally relevant stimulus features. This general conclusion appears to pertain to two additional aspects that are important from a functional point of view discussed subsequently.

1. Whereas the encoding properties of the model rely largely on the specific dynamical features of behaviourally generated optic flow, it could be shown that it is relatively invariant to changes in the environmental texture. This finding may be surprising, given the fact that for simple constant-velocity stimuli the responses of blowfly TCs are known to depend strongly on the textural properties (Dror et al., 2001; Eckert and Hamdorf, 1981). However, from a functional point of view it appears to be appropriate that the neuronal encoding of self-motion and of the spatial relationship of the animal to its environment is as independent as possible from the accidental textural properties of the environment.

2. It is generally agreed that many features of TC responses depend on stimulus history and that the resulting changes in neuronal response properties may be regarded as adaptive. However, neither the underlying mechanisms nor the functional significance of most of these phenomena have yet been clarified. Adaptive processes have been studied by very different stimulus paradigms and conceptual approaches. Adaptive changes to motion stimulation are suggested by experiments using brief displacements of the stimulus pattern or constant velocity stimulation (Borst and Egelhaaf, 1987;

de Ruyter van Steveninck and Bialek, 1988; Harris et al., 1999a,b, 2000; Kurtz et al., 2000; Maddess and Laughlin, 1985), but also time-varying velocity fluctuations (Brenner et al., 2000; Fairhall et al., 2001). Here that the optimal motion detector time constants required for explaining the neuronal responses to natural optic flow were found to be smaller than the time-constants estimated on the basis of the steady-state velocity tuning. However, the optimal time-constants were almost identical for the initial segment and later segments of the responses to natural optic flow. This finding would either imply a very quick adaptation to the dynamical stimulation (see e.g. Fairhall et al., 2001) or could hint at additional filters in the neuronal system that are missing in the current model. It should be noted, however, that the model performance in explaining the neuronal responses to behaviourally generated optic flow changes only little by shifting the movement detector time constants from the optimal values to values that also fit the experimentally determined steady-state velocity tuning (see figures 4.6, 4.7 and 4.8). In contrast to the time constants in the visual motion pathway, the gain of the system decreases slightly during prolonged stimulation with behaviourally generated optic flow. This finding is in accordance with experimental evidence for changes in contrast sensitivity of the visual motion pathway (Harris et al., 2000).

The information about distances to objects in the environment is not represented very explicitly in both the responses of the HSE-cell and its model counterpart. Can this information be used in a simple way for controlling visually guided behaviour? Since, for methodological reasons, it is hard to answer this question experimentally, it will be one next step of the model analysis to incorporate the model of the visual motion pathway into a closed-loop system and to assess different strategies of decoding the HSE responses.

The following chapter describes the "Virtual Fly" tested in the behavioural task of obstacle avoidance in 3D environments. In this way, the interpretation that the HSE-cell extracts behaviourally relevant information about the three-dimensional layout of the environment was challenged under closed-loop conditions.

5 Simulating the virtual fly

To simulate the behaviour of a fly, the signals of the sensory neurons must be transformed into motor signals to generate a behavioural reaction to the sensory input. The physical properties of the motor elements and of the environment determine, how these motor signals are transformed into movements of the fly. To close the control loop, the sensory signals of a simulated system must then be recalculated for the new position and orientation in the virtual environment.

By simulating the system in a closed control loop, hypotheses for the interpretation of the functional significance of the responses of sensory neurons can be tested. The ultimate goal of such an approach could be that the simulated system behaves like the modelled animal. Note however, that even an almost perfect emulation of natural fly behaviour would not be an evidence for similarities in the computational structure of the systems. The simulations of a virtual fly thus only show that the hypotheses implemented in the controller are sustainable. Other approaches have to be taken to get deeper insights in the computational structure of the neuronal circuits controlling the behaviour of the animal.

This chapter describes closed loop simulations of the flying virtual blowfly for basic orientation behaviour. Some simple sensory-motor transformation circuits are investigated in a simple wall-avoidance task.

5.1 Related work

Two basic behaviours are very likely controlled by the optic flow processing neurons. One of these behaviours is the so-called optomotor response, observed throughout the whole animal kingdom. When an animal is confronted with global visual motion, it responds by a movement following this motion either with its eyes, the head, or the entire body. This behaviour is usually interpreted to help the animal to stabilise its retinal image, but may also play a role to maintain a straight path. In the latter functional context the brain is assumed to balance the optic flow on both eyes (Götz, 1975a).

Another task that can be accomplished using optic flow information is the avoidance of walls or objects. Like the optomotor response, this task can be solved by balancing the optic flow on both sides of the animal. However, the correct compensatory response to an asymmetry is inversed in both situations. While the optomotor response is to turn towards the side of the larger progressive velocity, the obstacle avoidance requires the avoidance of the large translatory flow generated by a nearby object.

The fly seems to be able to resolve the apparent conflict between these tasks. A good hypothesis for the sensory-motor coupling thus should also be able to solve both tasks simultaneously.

5.1.1 Consequences of the nonlinear velocity encoding in tangential cells

The inherently nonlinear encoding of image velocities by correlation-type motion detectors and thus in the responses of the fly tangential cells has important consequences for the behavioural control based on these signals.

The bell-shaped response profile of the tangential cells causes differently signed difference signals if a pair of cells is confronted with preferred direction motion of different velocities. If the velocities are low, the cell confronted with the faster movement will respond with a larger signal than the cell facing the slower image movement. The sign of the difference is inversed if both velocities are super-optimal for the elementary motion detectors. In this case, the response of the cell encoding the faster movement will be lower than the response of the cell stimulated with slower motion (Götz, 1975b). If a behaviour is coupled to the difference of two tangential cell signals, the sign of the response thus can change implicitly: A response following the direction of motion can turn into an avoidance response by simply increasing the stimulus velocity. Because of this inherent change in behaviour a further analysis of the optomotor control system also in the context of the obstacle avoidance task seems to be interesting.

Figure 5.1: Implicit sign-reversal of the differential motion detector response resulting from the bell-shaped steady-state velocity tuning of correlation-type motion detectors. A positive relative difference in velocity may cause a positive (blue, dashed arrows) or a negative difference in the response (red arrows) depending on the absolute velocity value.

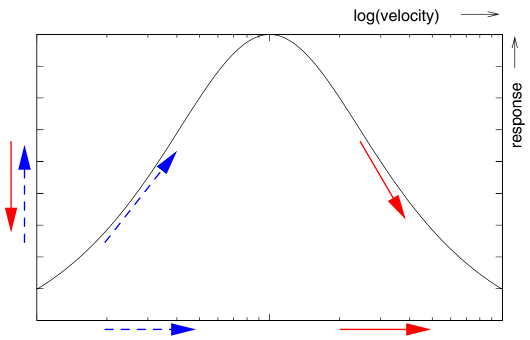

Another consequence of the detector properties is an inherent stability of control systems based on these signals. If an instability occurs, the sensor signals of the tangential cell increase to the cell's maximum response leading to an acceleration. Beyond that point, however, the response amplitude is are automatically reduced despite further acceleration of the movement. In effect, this stabilises the system at a high but constant velocity (Warzecha and Egelhaaf, 1996).

5.1.2 Previous robots and simulations

In several studies fly-inspired optic flow algorithms were implemented in simulation and on robotic platforms. Most of these systems use optic flow information mainly to stabilise straight movement paths. This approach is inspired by the very basic optomotor behaviour observed in many animals. By implementing a fly-inspired motion vision system in analog VLSI (Harrison and Koch, 1999) and integrating this circuit with a mobile robot, Webb et al. (2004) showed that such a system can indeed make the robots course control robust against asymmetries in its motor system. Huber et al. (1999) implemented a simulation model of the fly visual system which reproduces the optomotor behaviour. In a real-world test using a small robot (Khepera) and a panorama camera, the system additionally shows an emergent fixation behaviour, similar to a behaviour also observed in flies. Neumann (2004) designed and implemented a flight control system for a simulated helicopter. Major parts of this controller are inspired by the fly motion vision system, but the system is not thought to be a model of behaviour control of flies.

Other systems use the distance information present in translatory optic flow to implement obstacle avoidance. Franceschini et al. (1992) implemented a fly-inspired motion vision system in analog hardware to create obstacle avoidance behaviour of a robot. Interestingly, this robot was programmed to create straight forward movements interleaved with short turns, a strategy similar to the saccadic flight behaviour observed in free flying flies. In another robot experiment Lewis (1998) also used a saccadic movement strategy, in this case called "zig-zag behaviour", to avoid obstacles while stabilising the gaze of the robot by an optomotor response of the camera.

Starting from hypotheses drawn from quantitative behavioural experiments with *Drosophila*, Reiser and Dickinson (2003) implemented a saccadic movement strategy on a robotic system also exploiting optic flow information. This system was shown to be able to avoid the walls of a cylindrical environment on the basis of fronto-lateral looming sensors.

None of the systems mentioned above implements obstacle avoidance and the optomotoric response jointly by continuously balancing the optic flow. Only a few of these studies implemented both behaviours in one system. Both, Webb et al. (2004) and Neumann (2004), use a continuous balancing of optic flow to stabilise a straight course of their systems, but implement a frontal looming detector to create an obstacle avoidance behaviour as an immediate sharp reaction if a criterion indicating a nearby obstacle is met. Lewis (1998) also combines a optomotor response with obstacle avoidance. In his model, the saccadic obstacle avoidance is controlled by the temporal derivative of the image sequence, giving an non-directional selective estimate of the absolute optic flow.

The system described in the following sections implements a saccadic obstacle avoidance response and a continuous optomotor behaviour based on the signals of the HSE model neurons described in chapter 4.

5.2 Simulation system

The basic software architecture of the simulation system used for the virtual experiments is outlined in section 3.5. The generation and processing of the images is done by the same software modules as for the replay analysis described in chapter 4. In the following, two additional modules are introduced. The simulated neuronal response has to be transformed to flight forces in a sensory-motor coupling module. These flight forces must then be transformed to updates of the system's position and attitude in the virtual environment by a simplified physical model of flight dynamics.

5.2.1 Sensory-motor interface

Two different types of sensory-motor coupling were used for the simulation experiments. The first controller is a continuous coupling of the HSE signals to the turning response of the virtual fly. This type of controller implements the classical hypotheses drawn from the optomotor experiments with a fly turning on the spot in response to a purely rotating environment. The second controller implements the saccadic flight mode observed in freely flying flies. This type of controller generates short straight flight segments interleaved with sharp fast turns mimicking the body saccades observed in flies.

Both controllers and their performance are described in detail in the following sections.

5.2.2 Simulation of the physical environment

The neural motor commands of a flying fly are input to the wing beat controlling muscles. For simulations with a model structure close to biology, these muscle signals could be represented explicitly. The muscle activity then would control the movement of the wing in the air and an aerodynamical model could determine the resulting forces. Such an approach requires not only detailed knowledge on the exact anatomical structure of the wing-beat apparatus, but also a quantitative model of the aerodynamics of a beating wing at low Reynolds numbers. For the simulation of *Drosophila* flight, such a system was implemented by Schenato et al. (2001). It predicts the forces generated by the beating wings. The wing beat pattern is thereby specified using abstract parameters instead of control muscle activity.

To keep the model simple, the simulation can use a short-cut by calculating not muscle activity from sensory signals, but the resulting forces more directly. The output of such a sensory-motor transformation and thus the input to the module calculating the motions of the system is a six-dimensional vector for each time step specifying the three translational and three rotational force components.

The movements of the virtual fly resulting from the generated forces are constrained by the physical properties of the environment. For a flying insect, the forces actively generated by the animal add up with forces from gravity, air drag, and inertia to the effective forces accelerating the animal at a given point in time (figure 5.2). These forces have to be computed approximately to create realistic motion dynamics for the virtual fly, especially taking inertia into account. It is known from behavioural studies that after a sharp turn a fly drifts into the old direction of flight for some tens of milliseconds. The optic flow resulting from this sideward translation is supposed to be exploited by sensory neurons (see section 2.4).

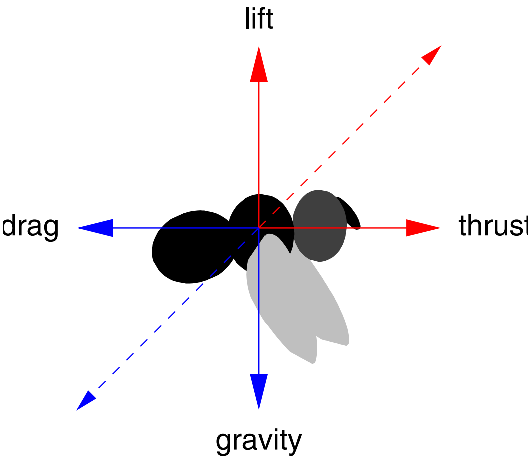

Figure 5.2: The translatory forces relevant to a flying fly. The forces generated by the fly, lift and thrust are necessary to compensate for the drag and the gravitational force. To fly at a constant velocity, the resulting generated force (red dashed vector) must be equal to the force resulting from drag and gravitation (blue dashed vector).

Details on the modelling of the physical environment are given below in the descriptions of the different experiments.

5.3 Optomotor behaviour

One of the basic behavioural reflexes observed in many insects is the optomotor turning response. This behaviour is interpreted to stabilise a straight path of movement by compensating rotations either caused by external disturbance or by internal asymmetries in the motor system.

For the horizontal plane, this behaviour can be achieved by levelling out the image velocity the animal observes on both sides.

5.3.1 Controller: Optomotoric response

A simple optomotor controller couples the difference of two simulated HSE-cells to the yaw moment generated by the system. Classical optomotor experiments revealed a lowpass filter with a long timeconstant to be present in this control loop (Egelhaaf, 1987; Warzecha and Egelhaaf, 1996). This is implemented in the model by lowpass filtering the difference signal with the recursive filter defined already in equation 4.2 for the sensory module.

The simplest way of coupling this signal to the yaw torque is a linear coupling defined by a motor gain factor. To avoid possible problems with aliasing caused by the time discretisation, the output yaw velocity of the system is limited to a torque resulting in a rotational velocity of $\pm 3000 \frac{^\circ}{s}$. However, for reasonable values of the motor gain, this yaw velocity is far beyond the dynamic range of the transformed HSE signals.

Physics: Friction and inertia of a rotating fly

The coupling of the yaw moment to the angular yaw velocity of the virtual fly must obey the principle physical constraints of friction and inertia a fly has to deal with.

For the rotation, the frictional moment caused by air drag is commonly assumed to depend linearly on the rotational velocity (Fry et al., 2003; Reichardt, 1973). The consequence of a (yaw) torque can thus be described by the equation

$$T = I\dot{\omega} + F\omega \tag{5.1}$$

where T is the torque moment, I the moment of inertia and F the frictional damping constant. ω is the angular velocity and $\dot{\omega}$ is the angular acceleration.

If the moment of inertia I is very small compared to the frictional constant F, the system is dominated by friction, which means that the rotational velocity

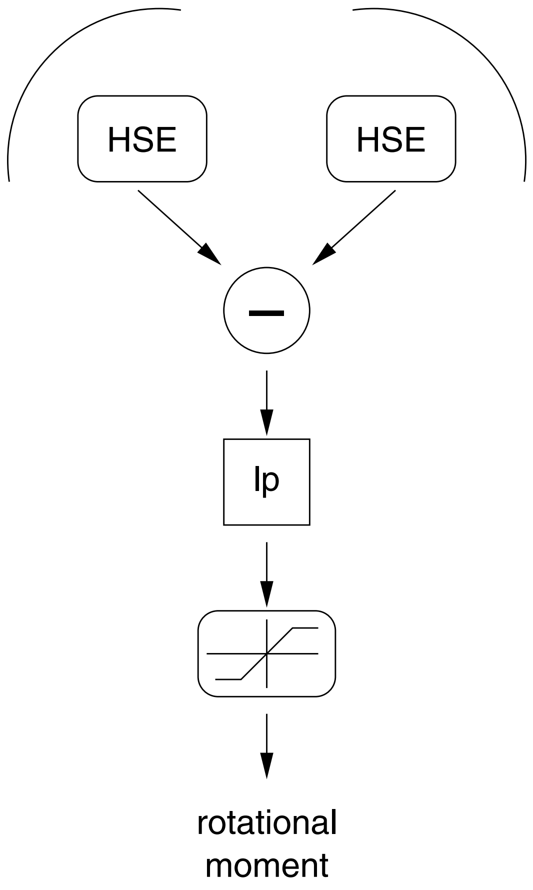

Figure 5.3: Controller circuit implementing the optomotor response: The differential signal of the simulated HSE neurons of both hemispheres is filtered by a lowpass filter. The yaw moment is proportional to the filtered signal. To avoid numerical problems, the velocity signal is limited.

of the system gets proportional to the yaw torque after a very short time after a change in torque. This was in fact concluded from the measurement of the moment of inertia and the estimation of the frictional constant by Reichardt and Poggio (1976). They estimated the time constant of the resulting lowpass filter, determined by the ratio I/F, as $\tau = 8$ms. Consequently, in later experiments simulating the flight of a tethered flapping fly the measured yaw torque of a tethered flying fly was coupled proportionally to the rotational velocity of the stimulation pattern (e.g. Warzecha and Egelhaaf, 1996) assuming that the acceleration phases are short enough to be safely neglectable. In these closed-loop experiments the flies were able to control the stimulus, suggesting that the dynamical situation was close enough to real flight.

More recent estimations based on experiments with a scaled model of the wings of *Drosophila melanogaster* beating in an oil tank suggest that the system is not dominated by friction. In contrast to the older assumptions, the time constant was estimated to be much larger (500ms $< \tau < 1$s, Fry et al. (2003)).

For the optomotor system of the virtual fly, a neuronal lowpass filter with a time-constant of $\tau = 750$ms is assumed (Warzecha and Egelhaaf, 1996). Thus the dominant time constant in the system is this neuronal lowpass and thus this constant is the relevant one for the dynamics irrespective of what the mechanical constraints really are. To keep the simulation simple, the angular velocity is coupled linearly to the output signal of the optomotor controller.

5.3.2 Results: Optomotor Controller

The optomotor controller was tested in two simulations. The classical experiment is to observe the tracking behaviour in a system reduced to one rotational degree of freedom. Additional to this, the behaviour of the system with constant forward velocity was analysed.

Classical optomotor experiment

The optomotor controller (figure 5.3) was calibrated in the test situation of the classical optomotor situation of a system in the centre of a rotating drum. In such a situation, the system is able to control its rotational speed while being fixed in position.

The virtual cylinder used for this experiment has a diameter of 930mm and a height of 900mm. The axis of the cylinder is parallel to the yaw axis of the virtual fly, the vertical position of the fly is at half height of the cylinder. If not stated otherwise, the same cylinder is used for all simulations described below.

The optomotor controller has two parameters. These are the time constant of the lowpass filter processing of the differential HSE signal, and the constant coupling gain which determines the slope of the coupling function.

The time constant of the lowpass filter was set to 750ms. This value for the time constant of the optomotor controller can be predicted from behavioural experiments (Warzecha and Egelhaaf, 1996). This time constant is not very critical in the case of steady state stimulation of the system with a constant velocity.

The coupling gain was varied systematically. As expected, this variation showed, that the system is not able to compensate for the rotation of the stimulus if the gain is very small (figure 5.4a, b). The system follows the movement of the drum with a lower rotational velocity, which leads to a reduction of the relative rotation of the drum with respect to the system. Beyond a critical value of the gain, the system is able to compensate the rotation almost perfectly (figure 5.4c, d). If the gain is much larger than this critical value, the system overcompensates and shows oscillations in the relative velocity with a close to zero average (5.4e, f).

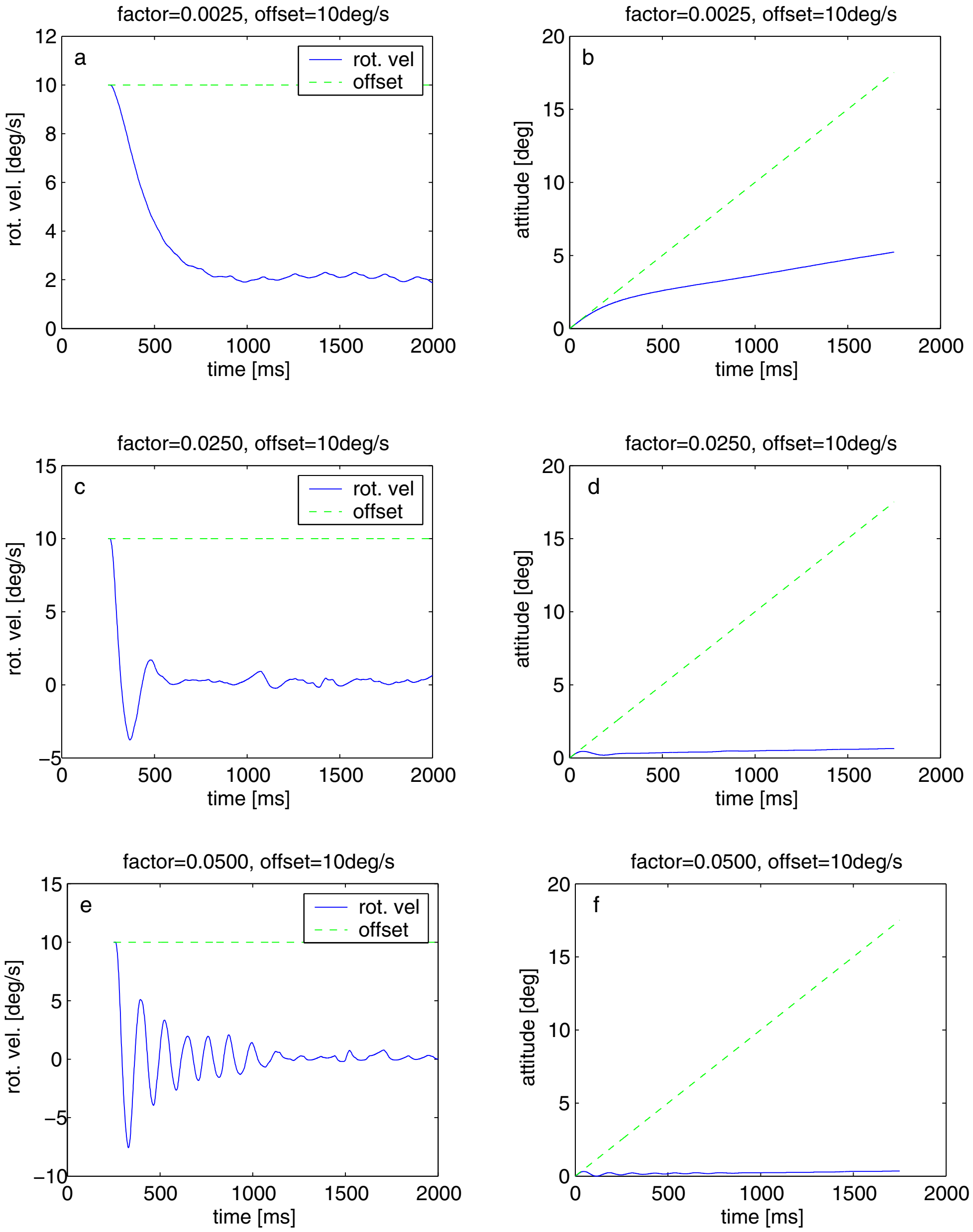

Figure 5.4: Closed-loop performance of the optomotor controller shown in figure 5.3. The system has only one degree of freedom, yaw rotation. The plots show the yaw velocity (left panel) and the resulting attitude (right panel) of the system relative to the rotating environment ($\dot{\omega} = 10^\circ s^{-1}$) With a low coupling factor (a,b) the system is not able to fully compensate the environmental rotation. With an increased factor (c,d), the compensation performance gets better. For a high factor (e,f) the system shows significant ringing in the compensatory response.

Optomotoric coupling for wall avoidance

When moving forward at a constant velocity, the optomotor circuit inherently leads to a tendency to avoid an approaching wall in a cylindrical test environment. This can be explained by the implicit sign reversal of the response caused by the velocity offset present in translational optic flow in the vicinity of objects and the bell shaped tuning of the motion detection system.

However, the response is much too weak to generate a stable wall avoidance. Figure 5.5 shows an example of this behaviour. For this simulation experiment, the system was moved with a constant velocity of $1\frac{\mathrm{m}}{\mathrm{s}}$.

If the coupling is inversed, the optomotor response drives the system on a circular trajectory, because the turning response to a small asymmetry in the input increases the asymmetry in this situation. Although the nonlinear characteristics of the motion detection system prevents an infinite angular acceleration, the system is trapped in the circular movement. With such a movement pattern, the translational components of the optic flow are masked by the large rotational velocities, preventing a meaningful response to close objects. Once rotating, the depth information present in the optic flow is practically not detectable.

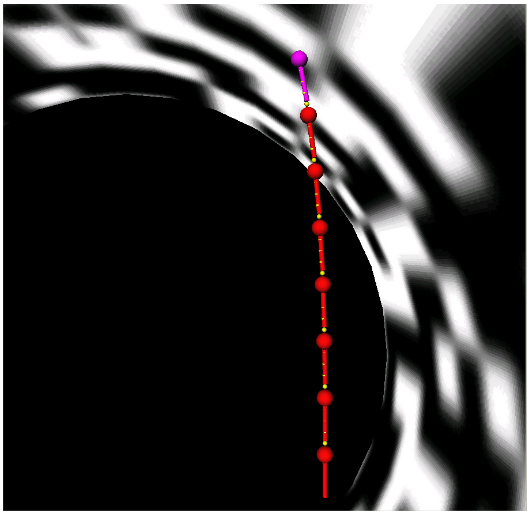

Figure 5.5: Example of the small wall avoidance tendency observed in closed-loop simulation of the optomotor system with a constant forward velocity of $1\frac{\mathrm{m}}{\mathrm{s}}$.

Compensation of motor asymmetries

The optomotor response is supposed to serve the stabilisation of a straight translatory movement and to correct for external rotatory disturbances and asymmetries in the flight motor or walking apparatus. Consistent with other technical implementations the system is able to correct for a motor bias in a combination of translatory and rotatory self motion. For the example shown in figure 5.6 the system was translated with a constant forward velocity of $1\frac{\mathrm{m}}{\mathrm{s}}$. A superimposed rotatory offset of $100\frac{\circ}{s}$ simulated the motor bias. The system compensates for the rotatory offset to some extent, which leads to a larger radius in the resulting trajectory than would result from the uncorrected bias. However, the compensation is not perfect and the compensatory effect is combined with the wall avoidance tendency also observed in unbiased systems.

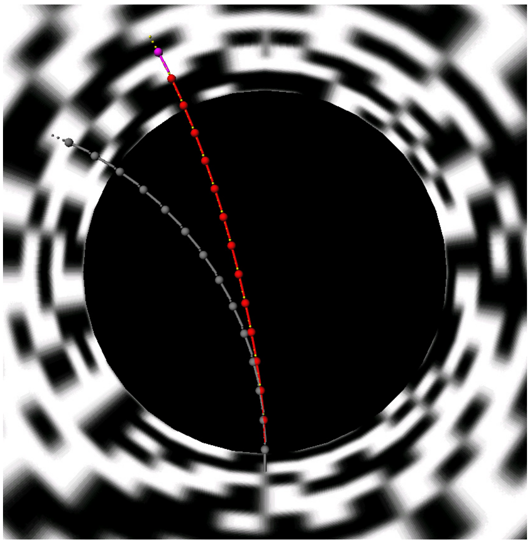

Figure 5.6: Trajectory of virtual fly with optomotor response (coloured) in comparison with the trajectory of a fly without this response (gray). This example illustrated the stabilising effect of the optomotor behaviour. The system compensates partly for a rotatory velocity of $100\frac{\circ}{s}$.

5.4 Saccadic behaviour

By introducing a saccadic motion pattern as observed in freely flying blowflies, the system obtains wall avoidance behaviour. During the short saccadic turns the optic flow is dominated by the rotational component while it mostly reflects the translational movements of the fly and the distance to the environment in the straight flight segments between saccades. Thus the behaviour effectively separates the translational from the rotational components of the optic flow. Balancing the flow observed by the animal in the intersaccadic parts of the flight leads to an equalisation of distance to the environment.

For this part of the analysis, the properties of the saccadic system were evaluated without the optomotor controller to investigate the performance of each system separately.

5.4.1 Physics of the flight dynamics

Depending on which estimation of the mechanical time constant is correct for the larger blowflies, the forces needed to steer a saccadic turn are different.

If, on the one hand, the system is dominated by inertia, as suggested by Fry et al. (2003), the flies would need to generate a large torque spike to initiate a saccade and they would need to stop the turn actively by another opposing torque transient. On the other hand, if friction dominates, as initially suggested by Reichardt and Poggio (1976), the system would need to produce an almost constant force during the whole turn.

To avoid the need to solve this problem, the forces are not modelled explicitly, but the change in head orientation is implemented by application of a template derived from measurements. For the generation of saccades, a fixed motor program is assumed that generates a stereotypical velocity time course for the head in every saccade. Indeed, the measurements done by van Hateren and Schilstra (1999) show that the time course of the saccades are very constant over many saccades. By generating rotations from a template mimicking the average time course observed in these experiments, the rotatory movements are realistic irrespective of the question what forces need to be generated to create such movements.

Figure 5.7 shows the template used for the saccades of the virtual fly in comparison to the average behavioural data. The velocity template is a simple Gaussian function ($\sigma = 10.5$ms) scaled to lead to a turning angle of $68°$. The data of van Hateren and Schilstra (1999) show that the fly modulates both the duration (σ) and the amplitude of the velocity time course to achieve different turning angles. To keep the simulations described here simple, only a small range of turning angles is used and for this range only the amplitude of the template is changed. However, for larger variations the template should also be scaled with respect to its duration.

5.4.2 Controller: Saccadic object avoidance

The controller implementing the saccadic flight mode is an adapted version of the controller described by Reiser and Dickinson (2003). While their original controller uses the signals of hypothetical fronto-lateral looming detectors as an input, the version described here generates saccades based on the signals of the model of HSE-neurons as described in chapter 4.

The controller is based on a state-machine with three distinct states (see figure 5.8).

In the first state, no yaw moment is generated. During the resulting straight flight, a lowpass filtered response of both HSE signals is calculated separately and a thresholding is applied to these signals. If one of the lowpass filtered HSE signals hits the threshold, the controller switches to the second state, initiating the saccadic turn. The threshold value, originally modelled constant by Reiser and Dickinson (2003), exponentially declines over time for the described

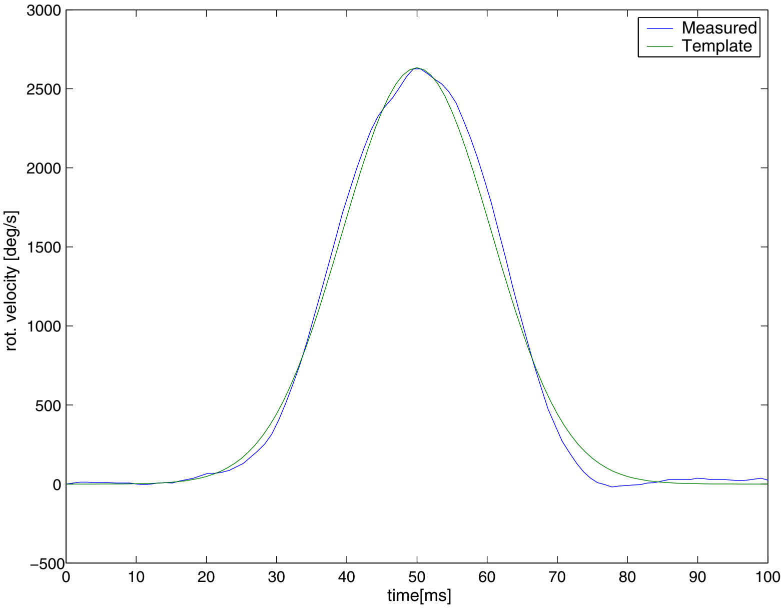

Figure 5.7: Velocity template used for the rotational velocity during a saccade. The template is a Gaussian velocity time-course fitted to the mean head trajectory for ≈ 70°-turns observed in coil-tracking experiments. Experimental data redrawn from van Hateren and Schilstra (1999).

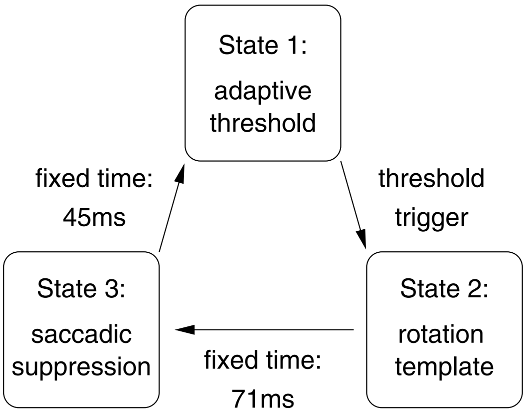

Figure 5.8: The controller circuit generating saccadic turns has three distinct states. The saccade is triggered by a threshold operation (state 1). To initiate the saccade, a rotational velocity according to the template shown in figure 5.7 is generated (state 2). The system suppresses new saccades for a fixed time immediately after a saccade (sate 3).

controller. Starting from a value above the dynamic range of the HSE signals it asymptotically reaches a value below the typical depolarisation of HSE observed in straight flight. This exponential decay modulates the probability of the generation of the next saccade: The longer the intersaccadic interval lasts, the more probable gets the generation of the next saccade. For a given distance to objects or walls, this also leads to regular generation of saccades within similar intervals, as observed in free blowfly flight, without explicitly modelling an internal clock for saccade generation.

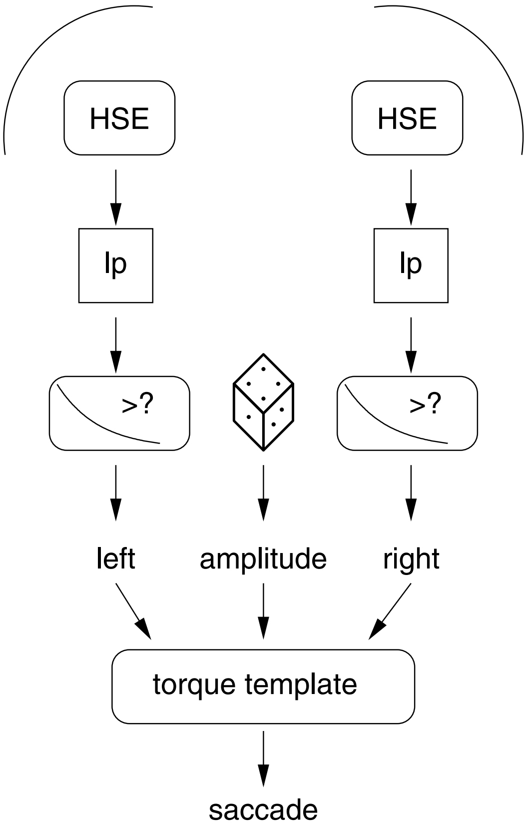

Figure 5.9: Circuit controlling state 1 of the saccadic controller: The low-pass filtered signal of each simulated HSE neuron is compared to a threshold value decreasing in time (see text). The saccade is directed away from the side reaching the threshold.

During the second state, the controller generates the yaw velocity of the saccadic turn from the Gaussian template. The turning direction is determined by the side of the HSE cell crossing the threshold. The sign of the turning direction (towards or away from the triggering HSE) has to be clarified in a first simulation experiment. To avoid nearby objects, the fly should avoid large image flows. But due to the inherent ambiguities of the motion detection system this may mean that the fly has to avoid the side of the HSE with the smaller response amplitude.

A scale factor s determining the amplitude of the Gaussian turn template is chosen randomly from a range of $0.7 < s < 1.3$. This results in saccadic angles from the range of $68 \pm 20°$. The second state has a fixed duration of 71ms.

In the following third state, no new saccade can be generated. The duration of this state is fixed to 45ms. A further function of this state is described in section 5.4.5

Blowflies fly their saccades not by turning around the yaw body axis, but by a combination of roll and pitch (Schilstra and van Hateren, 1999; van Hateren and Schilstra, 1999), leading to a banking like aeroplanes do in a sharp turn. This directs the upward thrust generated by the wings towards the outer side of the turn. At the end of a 90° saccade, the upward thrust thus is directed against the prior flight direction counteracting the movement into the old flight direction driven by inertia, now causing sideward drift. Immediately after the turn, the fly rolls back into level flight. This behaviour is mimicked by the virtual fly by generating sideward thrust directed to the outer side of the preceding turn during the third state of the controller.

During all states, a constant forward thrust is generated by the virtual fly. The thrust value is chosen to result in a maximum forward velocity of $1\frac{\text{m}}{\text{s}}$ in straight flight.

To evaluate the properties of this controller it was combined with different physical modules and parametrised differently. Three variations of the simulation are described in the following sections.

5.4.3 Simulation without inertia

In a first simulation experiment, the physical module does not model inertia and friction explicitly, but generates a constant forward velocity tangential to the system's flight path and proportional to the forward thrust generated by the controller. This variation may be close to the situation observed in Drosophila by Tammero and Dickinson (2002b). These very small flies seem to be dominated by friction so much that they can fly narrow turns without noticeably drifting into the old flight direction. Consequently, this dynamical model is similar to the physical model of Reiser and Dickinson (2003) which was intended to simulate the experiments of Tammero and Dickinson (2002b).

The drift-free situation also fits almost perfectly the dynamics of a robotic vehicle driving at constant speed. Such a system compensates for the drift movements by the high drag forces generated by the wheels against lateral movements. However, this situation is clearly not a valid model for a flying blowfly which has to deal with considerable drift movements following the saccadic changes in flight direction.

Results

Without inertial drift effects modelled in the trajectory generation, the saccadic flight mode leads to a reliable avoidance of the cylinder walls in the test environment when the fly turns towards the side of the HSE cell that is more depolarised indicating that the system operates in the super-optimal part of the velocity tuning curve. Simulation experiments with different saccade directions clearly show that this turn direction is crucial for the performance of the system.

Although the amplitude of the saccades is drawn from a pseudo-random distribution, such a system can successfully navigate for more than 4.75 seconds in the test cylinder in 90% of the flights when the turn is directed towards the side of the more depolarised HSE cell. Note that each run of the simulation results in an individual flight path caused by the random selection of saccade amplitudes.

As a control, the saccadic controller was replaced by a module generating saccades to random directions with the same average saccade frequency as observed in the simulation experiments. Such a random walk is on average much shorter (see gray histogram in figure 5.10) and can serve as a benchmark for the controller.

To test whether the system performance is stable over different initial conditions, the starting position within the cylindrical arena was varied. The rate of success is almost invariant with respect to the starting position within the cylinder. Figure 5.10 shows histograms of the duration of the simulated flights.

If the turn direction is inversed, i.e. if the controller avoids the side of the more depolarised HSE cell, the system is completely unable to avoid the walls of the cylinder. In this case all simulated flights are shorter than the average random flight generated as a control (see figure 5.11).

Figure 5.12 shows an example for the trajectory and the signals generated by the system. Note that the system generates different trajectories for a given starting position because the saccade amplitude is chosen pseudo-randomly. The turn directions, in this example approaching the side of larger HSE depolarisation, lead to an avoidance of the closer wall for almost all saccades.

Compared to the response to behaviourally generated optic flow (see section 2.4) the simulated HSE neurons show a more distinct response to the saccadic turns (dashed lines in figure 5.12c). This may be caused by the large amplitude of the saccades generated by the saccadic controller. The average amplitude is 70° which is in the range of the largest saccades observed in the behavioural experiments (van Hateren and Schilstra, 1999). Smaller amplitudes were not generated in the simulation with random amplitude selection and will be used in future versions of the system coupling the saccade amplitude to the neuronal signals, too.

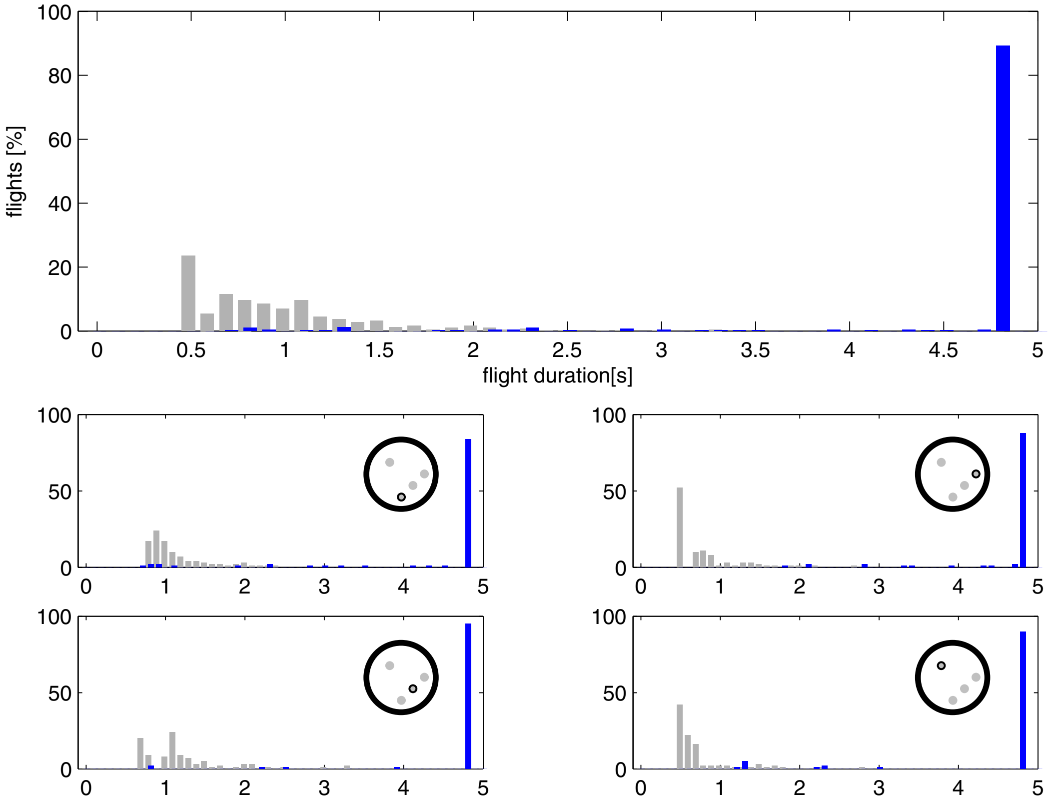

Figure 5.10: Histogram of the simulated flight duration of a saccadic flight controller without inertia. Lower panels show the histograms of the duration of 100 flights for each of 4 different starting positions, the upper panel shows an average of these histograms. The gray bars show the durations of 100 flights with random saccade generation (direction, exact timing) as a reference. The blue bars show the durations of the visually controlled flights.

5.4.4 Simulation with inertia

Translational physics: Air drag and inertia

Drag is a force generated by a body moving in a fluid, in this case by a flying insect in the air. This force is generated by the friction between the body and the surrounding medium. Its direction is opposite and parallel to the direction of movement. The size of this force is determined by the velocity and the shape and size of the body. Depending on the velocity, the size and form of the body and the viscosity of the medium, different types of flow around the body can be observed.

At low velocities, smooth and regular so-called laminar flow is observed. In this

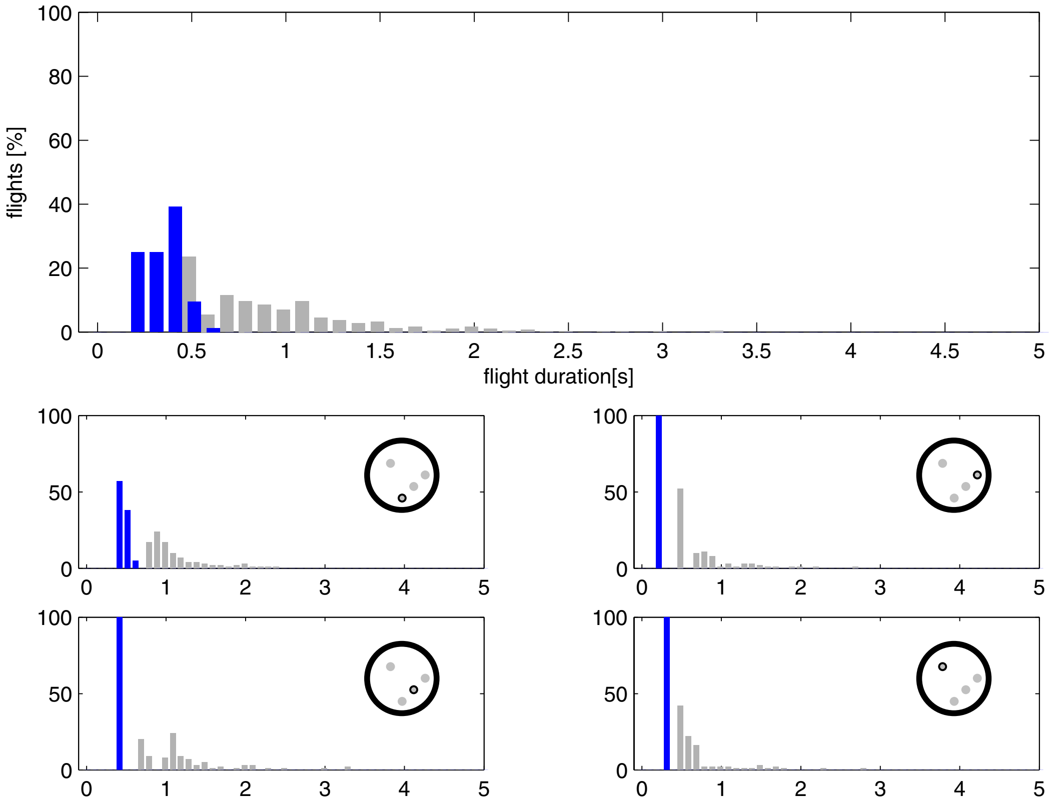

Figure 5.11: Histogram of the simulated flight duration of a saccadic flight controller without inertia for 100 flight for each of 4 starting positions . The direction of the saccadic turns in inversed in comparison to figure 5.10. A controller responding by avoidance of the more depolarised HSE cell is by far less successful than the random saccade generation.

case, the viscous forces dominate and the drag depends linearly on the velocity. For a sphere of radius r moving at velocity v, the drag in laminar flow can be computed by Stokes' law (Gerthsen and Volgel, 1997):

$$f_d^{laminar} = -6\pi\nu r v \tag{5.2}$$

where ν is the viscosity coefficient of the fluid.

At higher velocities, vortices occur and disturb the flow. This flow type is called turbulent flow. The drag in this type of flow depends on the squared velocity. In turbulent flow, the drag force is

$$f_d^{turbulent} = -\frac{1}{2} c_d \rho A v^2 \tag{5.3}$$

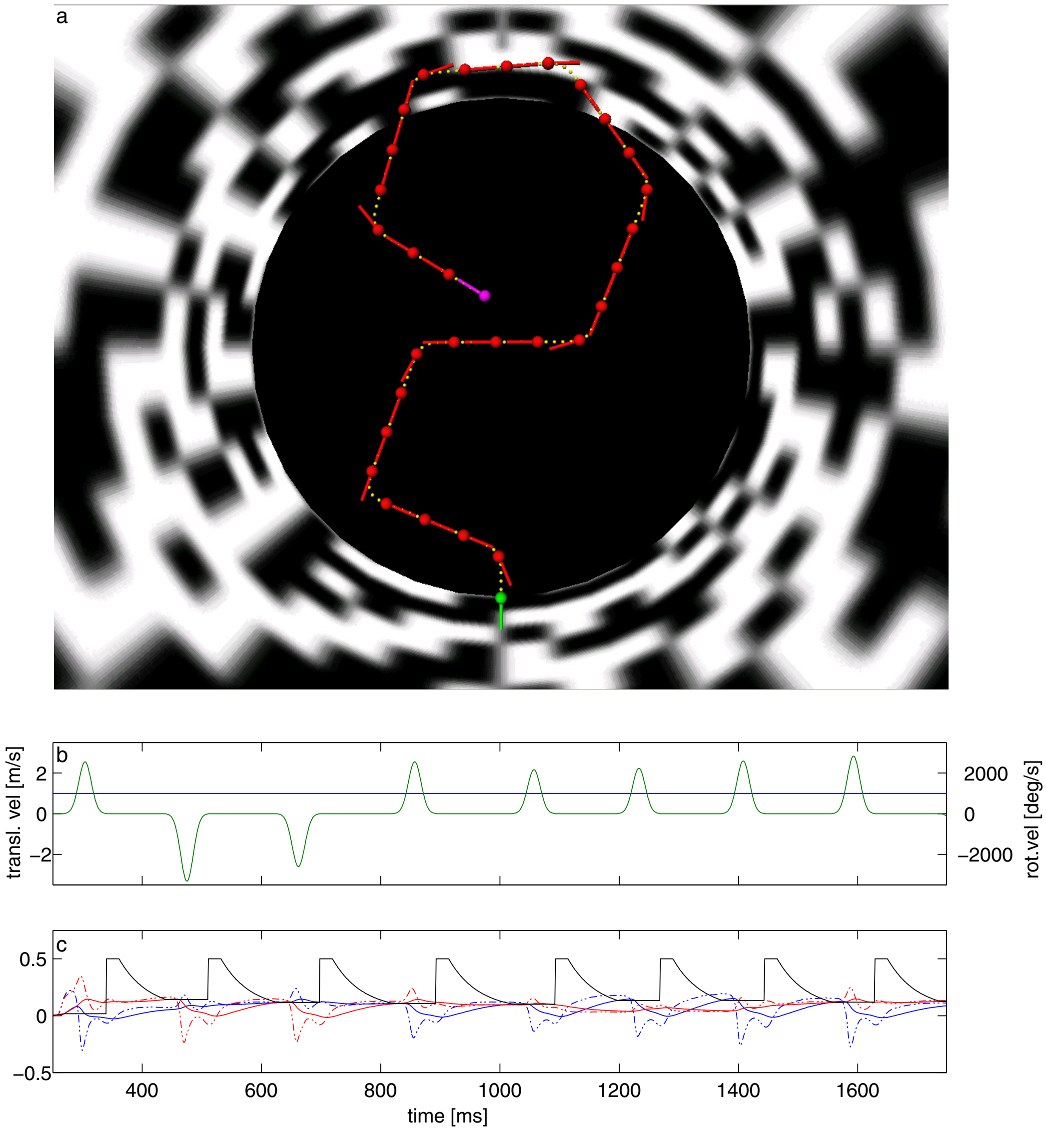

Figure 5.12: Typical example for the trajectory and signals generated by the closed loop simulation of the saccadic controller without inertia. (a) The trajectory clearly shows the saccadic turns and perfectly straight movements in-between. (b) The translational velocity is constant, the yaw velocity is derived from the differently scaled saccadic templates. (c) The signals (dashed lines) of the right (red) and the left (blue) HSE cell, the according lowpass filtered signals (red and blue lines) and the threshold of the saccadic controller (black line).

where A is the frontal area of the body, ρ the density of the medium and c_d a dimensionless coefficient depending on the form of the body. For a sphere, the drag coefficient is typically $c_d = 0.45$.

Information on the type of flow occurring in a certain situation is given by the Reynolds number, defined as

$$Re = \frac{\rho v L}{\nu} \tag{5.4}$$

where v is the velocity, L the length of the body, ν the fluid viscosity and ρ the density of the fluid. For low Reynolds numbers, the flow is laminar. The transition to turbulent flow is marked by the critical Reynolds number Re, depending on the form of the body. This transition is not very sharp. For a wide range of velocities, the flow is in a transitional state so that both mechanisms are partly responsible for the drag experienced by the moving body. This is illustrated by figure 5.13 showing measured drag coefficients for different bodies plotted against the Reynolds number characterising the flow situation.

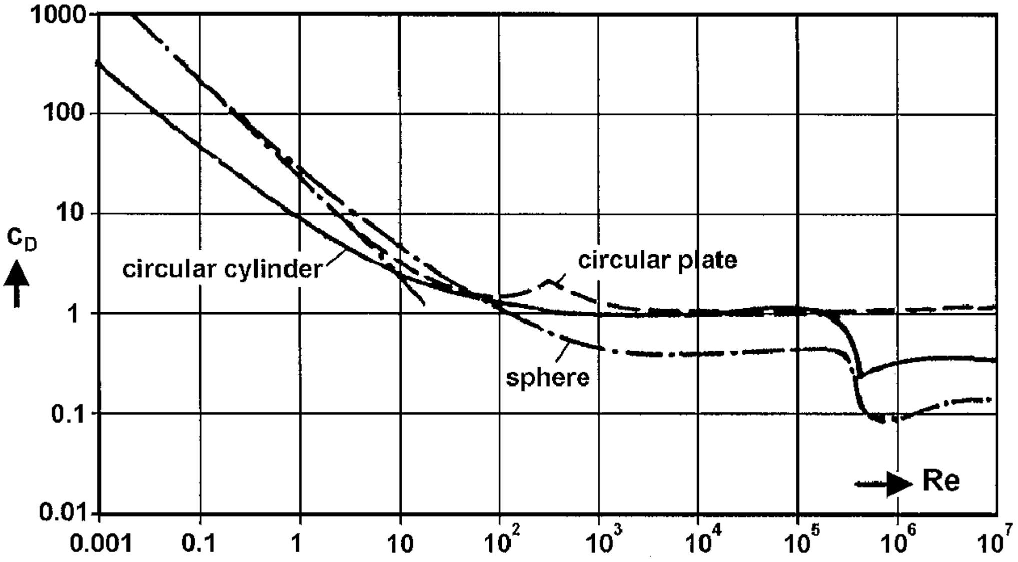

Figure 5.13: Drag coefficient c_d of technical bodies in dependence of the Reynolds number. Note that c_d is not constant for small Reynolds numbers. Figure taken from Nachtigall (2001)

A blowfly operates in this transitional range of Reynolds numbers. For a body with a length $L = 1\text{cm}$ moving at a velocity $v = 1\frac{\text{m}}{\text{s}}$, the Reynolds number in air ($\frac{\nu}{\rho} = 1.5110^{-5}\frac{\text{m}^2}{\text{s}}$, Nachtigall (1977)) is $Re = 6622.5$ being close to the range of the transition to pure turbulent flow (see 5.13). Therefore it is not trivial to calculate the drag experienced by a fly at a given velocity.

Two different approaches lead to an estimation of the drag coefficient.

In his diploma thesis, Weiss (2005) made an attempt to measure the drag coefficient of a fly body. To do this, he measured the velocity of a falling fly body using high-speed video recordings. From the velocity, the weight and the size of the fly, the drag coefficient can be calculated. He reports a drag coefficient of $c_d = 1.6$ for his experimental situation.

Another approach is to estimate the drag coefficient on the basis of observations from behavioural experiments.

To keep flight altitude, half of the force generated by a flying fly must be directed opposite to the gravitational vector (downwards in forward flight). In a constant velocity flight, the drag must further be equal to the opposing (forward) force generated by the animal. The maximal speed observed in free flying blowflies is approximately $2.5\frac{\text{m}}{\text{s}}$. The maximal translational force a blowfly can produce is thought to be $2g$ (Schilstra and van Hateren, 1999) (where g refers the the gravitational force generated by the body). Following this, in a flight with maximal velocity and at constant altitude, the drag equals the gravitational force of the fly.

$$mg = \frac{1}{2} c_d \rho A v^2 \tag{5.5}$$

With $m = 70\text{mg}$ the mass of the fly and $g = 9.81\frac{\text{m}}{\text{s}^2}$ the gravitational constant. $\rho = 1.29\frac{\text{kg}}{\text{m}^3}$ is the density of air, $A = 19.6\text{mm}^2$ the frontal area of the fly (circle assumed with radius $r = 2.5\text{mm}$), and $v = 2.5\frac{\text{m}}{\text{s}}$ the velocity of the fly.

The drag coefficient is the only unknown in the above equation and can be calculated to be $c_d = 8.691$ for the given values.

For the simulations described in the remainder of this chapter, a constant value of $c_d = 8$ was used. It should be noted, that the drag coefficient rises at low velocities, thus the calculation of air drag with a constant drag coefficient underestimates the real drag.

Results

Taking the inertia into account resulting in drift movements following saccadic turns, the model performance drops considerably. The system is still avoiding the walls, but the flight duration is longer than 4.75 seconds only in 40% of the simulated flights (figure 5.14). Furthermore, the performance varies strongly with the starting position in the simulated cylinder. From a starting position close to the cylinder wall, the system fails more frequently than if started in positions further away from the walls.

The example drawn in figure 5.15 shows that the virtual fly generates new saccades before the drift following the saccadic turn declines. The result is that the virtual fly is almost constantly oriented perpendicular to the flight direction, leading to a trajectory of sideward circular flight.

For these simulation experiments, the controller generated saccades towards the side of the larger depolarised simulated HSE cell, as was observed to be the successful direction in the simulations described above.

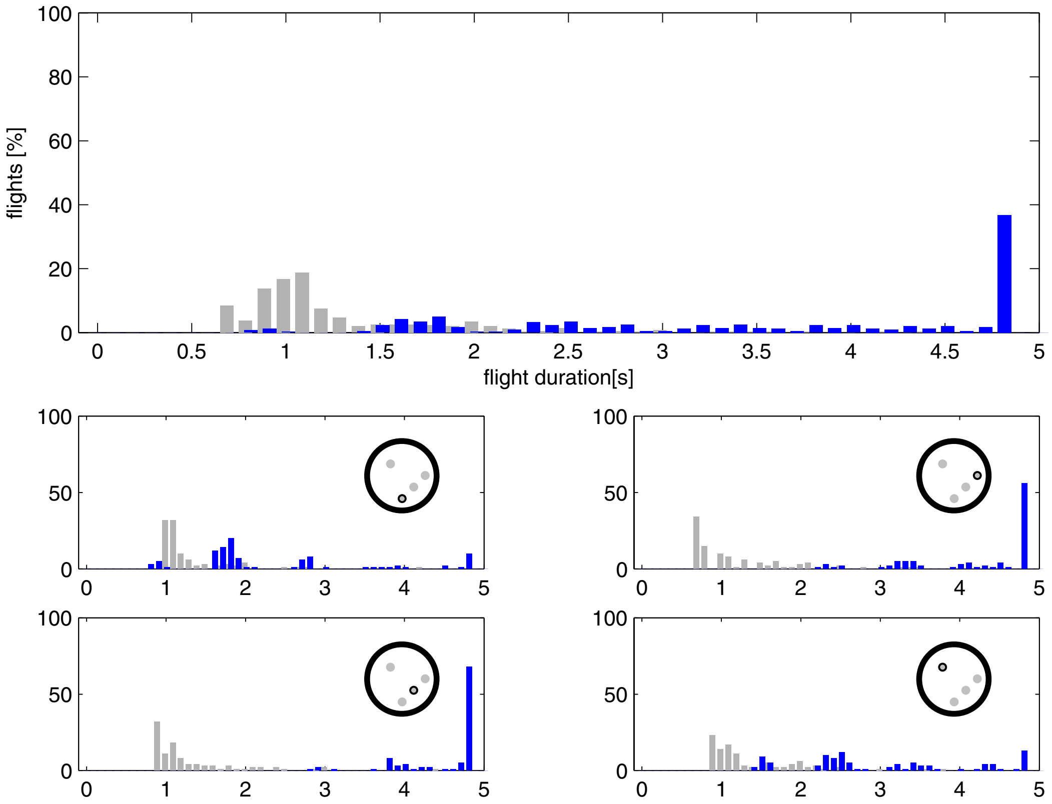

Figure 5.14: Histograms of the flight durations observed with saccadic control and simulation of the inertial forces (compare to figure 5.10).

5.4.5 Simulated banked turns

As an elaboration of the control system, active compensation for the drift movements was added. This resembles the banked turns observed in the saccades of freely flying flies. Following a saccade, the system generates a short translational

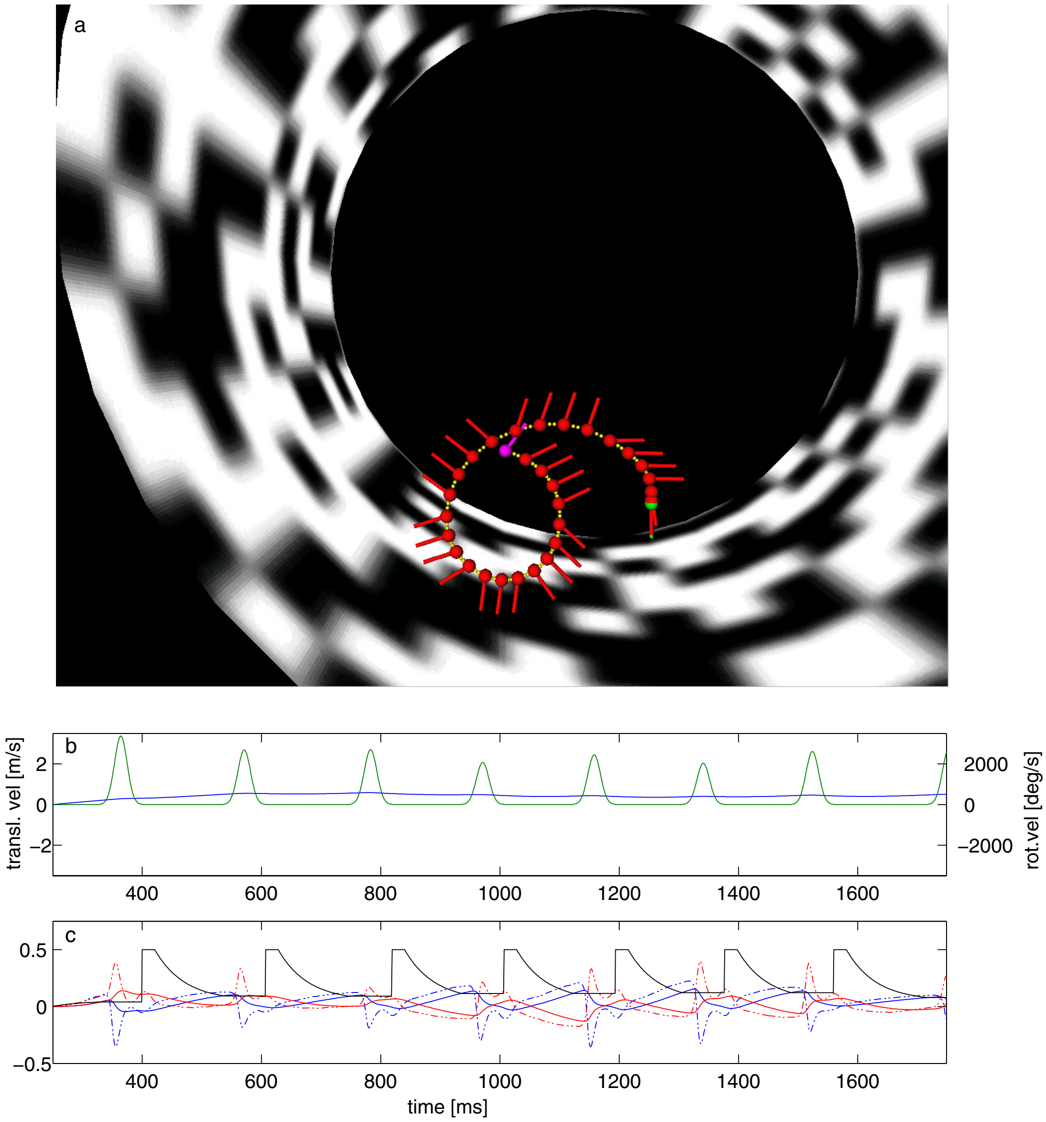

Figure 5.15: Example trajectory and signals generated by the saccadic controller with realistic physical modelling. After each saccadic turn, the virtual fly drifts into the old flight direction. The drag is too small to stop this drift movement before the next saccade is generated. This reduces the performance of the system dramatically.

force peak opposing the expected drift movement.

Controller extended to elicit banked turns

The controller generates a sideward thrust during the second state. If the fly banks by 90°, as observed in large amplitude saccades, it directs the upward thrust sidewards. Further, the system may create additional thrust to actively counteract the movement. The mean thrust generated by the system described below was 1.5 times the gravitational force. This sideward thrust is also generated during state 3 of the controller.

Results

This simple extension of the control mechanism leads to a significant improvement of the system performance. Using this control scheme, the system successfully avoids th wall for more than 4.75 seconds in almost all simulated flights (figure 5.16). This performance is invariant with respect to the starting position. Even if started relative close to a cylinder wall, the virtual fly avoids the wall.

The example trajectory presented in figure 5.17 shows that the virtual fly successfully compensates for the drift. The long axis of the system gets close to the direction of flight between saccades. However, a residual misalignment of body axis and flight direction causes non-zero sideward velocity of the system during intersaccades as observed in the real fly.

5.4.6 Combining saccadic and optomotor control

The saccadic controller described above and the optomotor control system described in section 5.3 can be combined by addition of the yaw moment generated independently by each controller (figure 5.18. The optomotor controller could stabilise the straight intersaccadic segments in such a combination. The combination was simulated to check that the two mechanisms do not interact destructively and to test whether the optomotor controller can stabilise the straight intersaccadic segments in presence of a rotational offset.

In simulated flights using this combination scheme of both controllers, the virtual fly shows a performance comparable to the pure saccadic controller. Figure 5.19 shows the duration histogram of simulated flights using the combined controllers. For this simulation experiment, a constant turning velocity of $10\frac{\circ}{s}$ was added to the yaw moment generated by the controller. Such a situation could arise from a small asymmetry in the motor or wing apparatus of the fly.

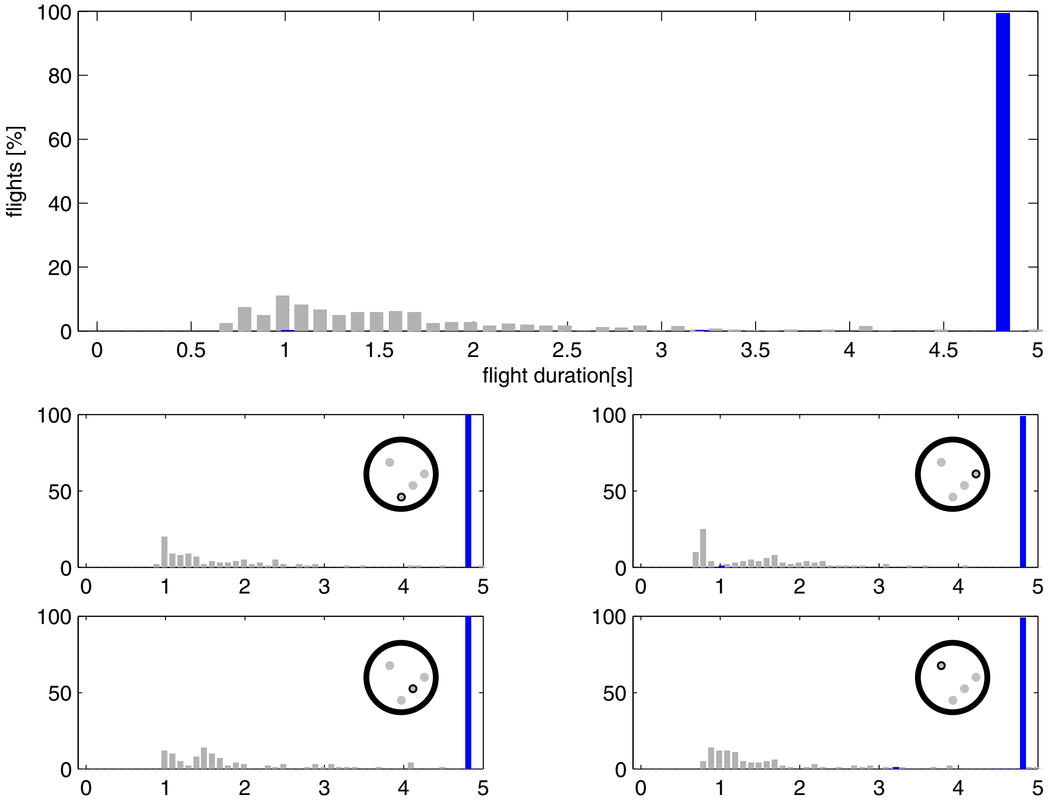

Figure 5.16: Histograms of the flight durations observed with additional drift compensation as observed in the banked turns of flies (compare to figure 5.14).

5.4.7 Different environment

A fly is capable to successfully navigate in different environments. For example, flies are able to fly around in human buildings although these environments differ significantly from the natural surroundings in which the evolution of the fly navigation system took place. A good model for the navigation system thus must also be able to deal with a variety of environmental situations.

Additionally to the simple cylinder, the saccadic controller was tested in two other environments.

Additional obstacle

The first test environment was simply derived from the cylindrical environment by adding an additional obstacle. The obstacle was a cylinder with a diameter of 4.5cm. It was placed in the centre of the cylindrical flight arena. The texture of

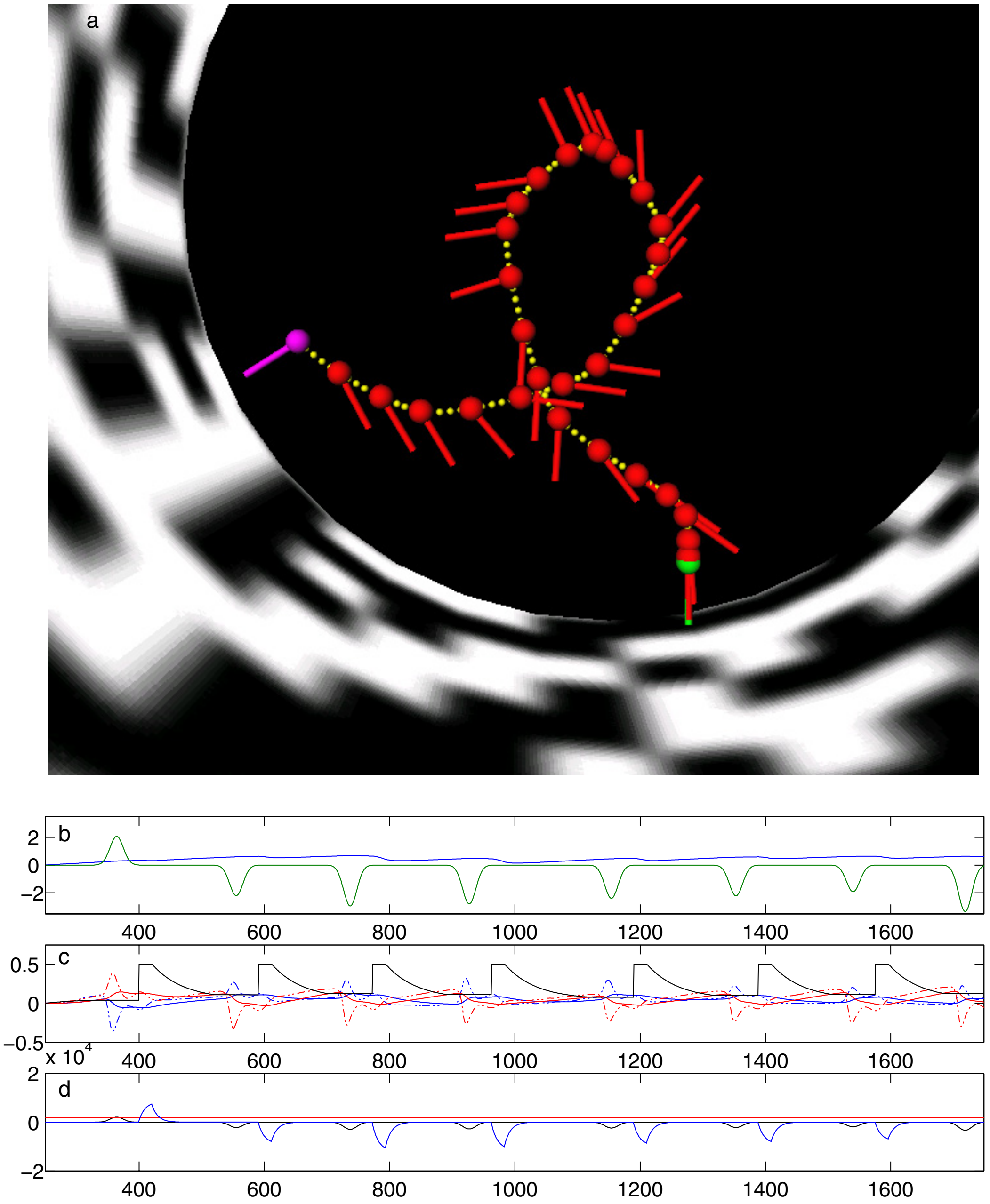

Figure 5.17: Example of a trajectory and signals of a saccadic controller compensating for the drift movements by mimicking banked turns. Like in the prior examples, plot b shows the velocities of the system and plot c shows the neuronal signals and the threshold. Plot d additionally shows the forces generated by the virtual fly. The constant forward thrust (red), the yaw moments (black), and the sideward thrust compensating the drift (blue).

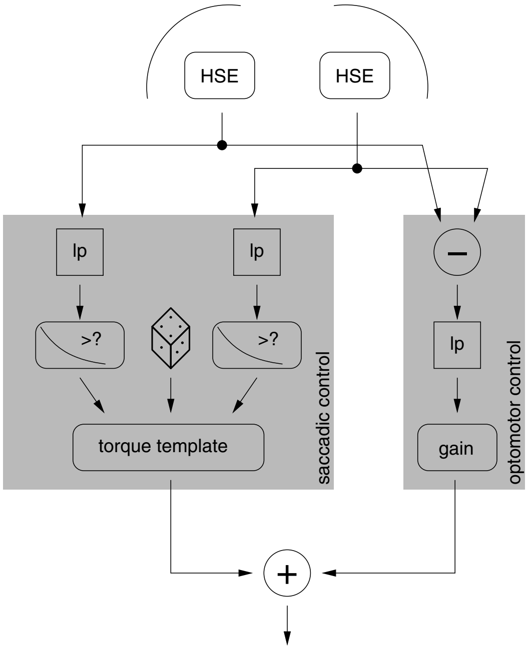

Figure 5.18: A possible combination scheme of the two controllers. The yaw moments independently generated by both controllers are combined by addition.

the obstacle is a copy of the one covering the surrounding walls, compressed in one direction to the length of the smaller perimeter.

The performance of the system is reduced by the presence of the additional object (figure 5.20). Only a fifth of the flights lasts longer than 4.75s. Compared to the durations of the random flights, the controlled flights are just slightly longer.

From certain positions in the cylinder the system seems to navigate towards the object instead of avoiding it. Such a behaviour could be interpreted as a fixation behaviour or a targeted landing behaviour in a real animal. This behaviour leads to a number of flights shorter than expected from random behaviour (lower left Histogram in figure 5.20). An example for such a “fixation” flight is shown in figure 5.22.

Living in a Box

A second test environment was a box like the one used in the experiments described before in chapter 4. For the simulated flights, the length of the cube edge was scaled to the diameter of the cylinder.

The cylinder setup and the box used in the experiments differ not only with respect to the geometry but also to the textures covering the walls. Using the same random dot texture as in the simulation experiments in the cylinder, the performance of the system is comparable for both spatial layouts. Simulation experiments with the box textured like the flight arena used by Schilstra and van

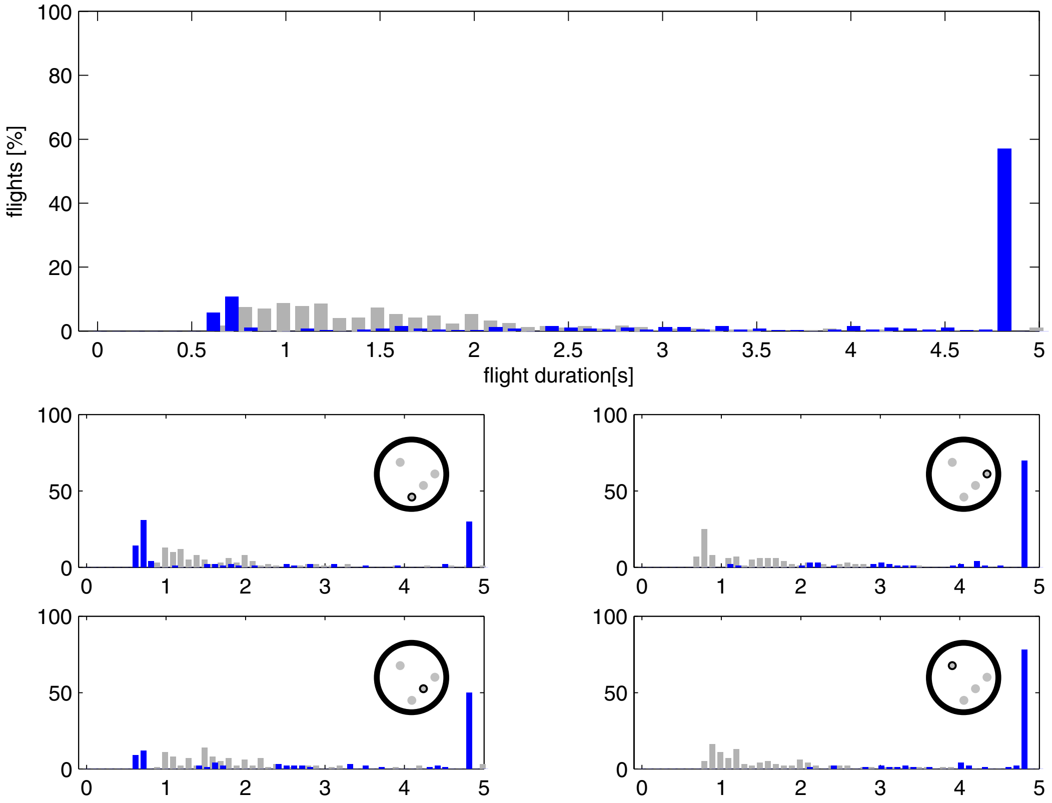

Figure 5.19: Histogram for flight durations for the combination of saccadic control and optomotor reflex.

Hateren (1998b) reveal that the change in texture is a critical one.

In this differently textured cube, the virtual fly cannot successively avoid the walls although real flies successfully navigate in a much smaller version (Schilstra and van Hateren, 1998b). All simulated flights are shorter than 4.5s and even slightly shorter on average compared to random flights (figure 5.23). Again, the system seems to fly towards the walls of the environment instead of avoiding them.

Changing the sign of the saccade directions so that the virtual fly avoids the side of larger HSE depolarisation does not change the situation qualitatively. The controlled flights in this case also are shorter than the random flights.

Depending on the starting position within the cube, the system hits a certain part of the wall. Figure 5.24 shows the “landing” position in dependence of the starting position of the system. The corners of the box seem to be a target of the system in some cases. For a starting position in front of one wall (red asterisk), the system turns around by $180°$ and flies towards the wall behind the virtual fly in the starting direction.

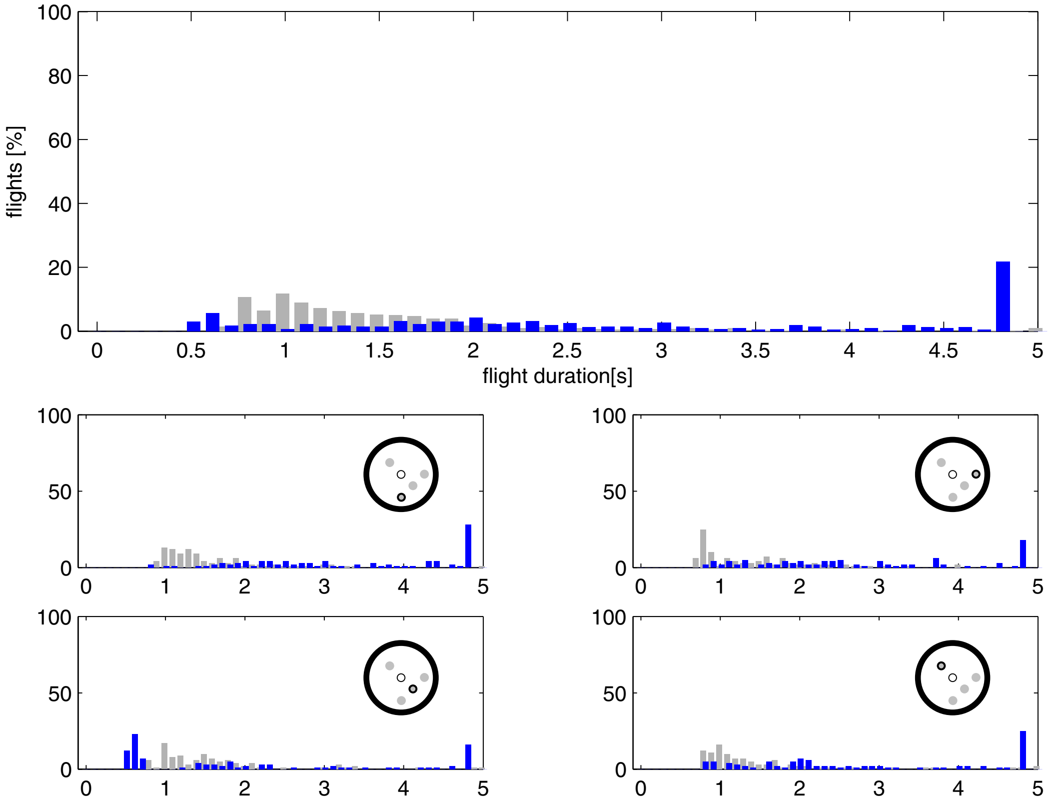

Figure 5.20: Histogram of the durations of simulated flights in presence of a central obstacle in the cylindrical arena. The performance of the system is reduced by the introduction of the additional object (compare to figure 5.16). In certain positions within the arena the system tends to navigate towards the object instead of avoiding it.

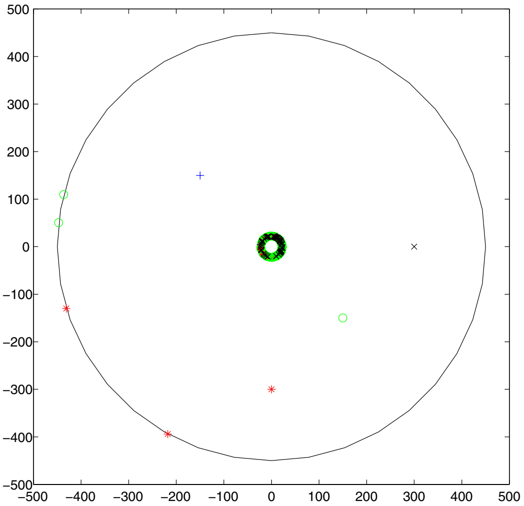

Figure 5.21: Final positions of the trajectories hitting the wall or the object in a cylindrical environment. The different symbols reflect the starting point of the trajectories. Symbols inside the cylinder mark the start, symbols on the cylinder or object walls mark the end of an trajectory.

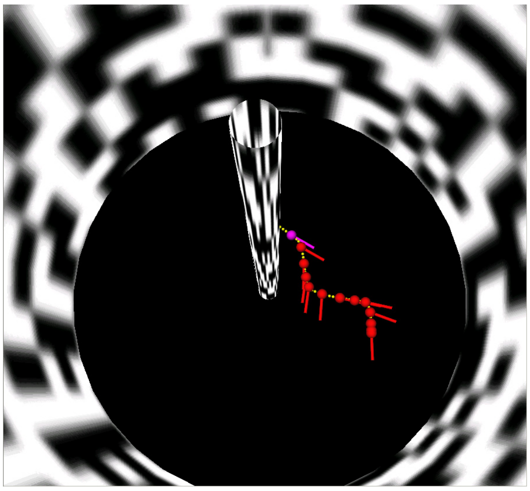

Figure 5.22: Example trajectory for the fixation behaviour of the system in certain positions in the arena.

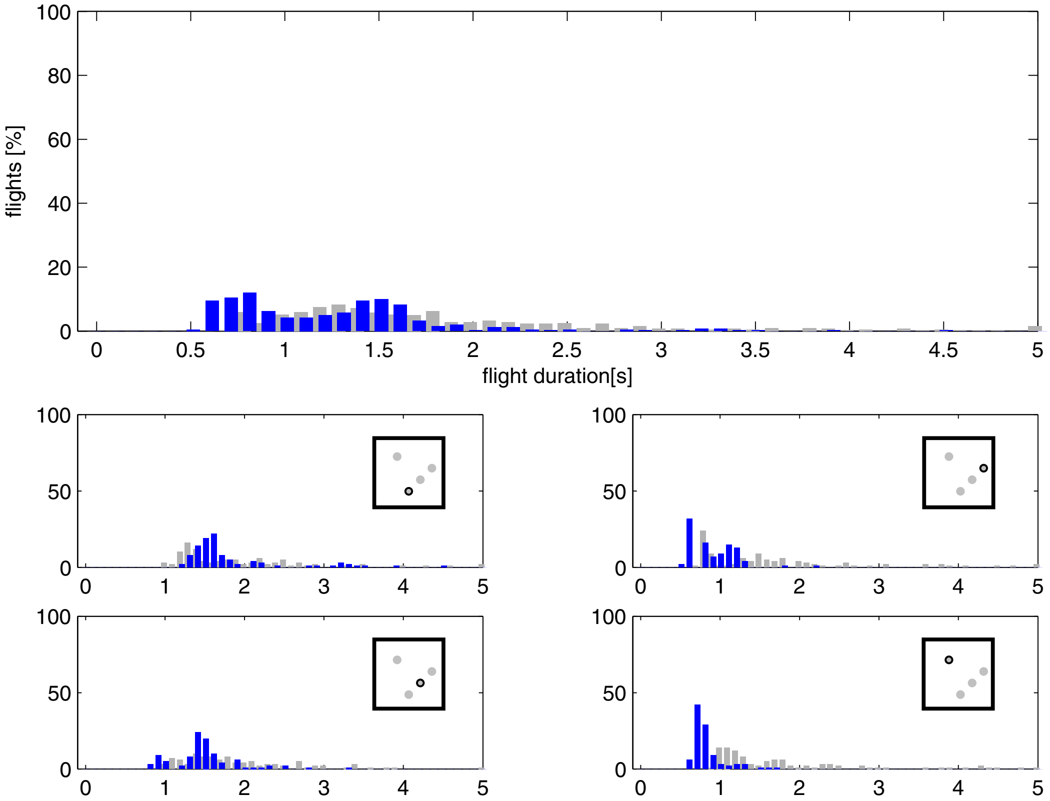

Figure 5.23: Histogram of the flight durations observed in a box environment. On average, the flights are shorter than the random flights in this environment. The lower panels show the separate histograms for the 100 flights for each starting position, the upper panel shows the joint histogram of all starting positions.

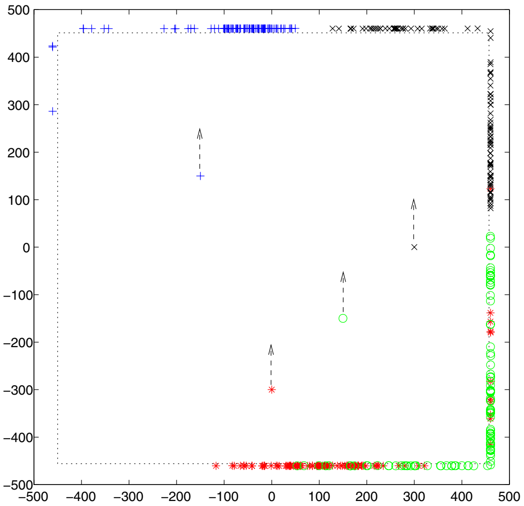

Figure 5.24: Positions of the virtual fly hitting the wall of a cube with low-contrast texture in dependence of the starting positions. Each colour/symbol is assigned to a certain starting positions, dashed arrows indicate the starting directions. Each symbol on the walls (dashed box) indicates the end point of one flight.

On first sight, this seems to contradict the finding that the responses of the model to the behavioural trajectories are robust against changes in texture (see section 4.2.7). However, the difference measure defined in chapter 4 compares two responses after optimally scaling one to the amplitudes of the other. To check whether a difference in amplitude can cause the performance drop observed with the natural scene texture, the simulation experiment was repeated with a halved threshold value. This shortens the duration of the intersaccadic periods because the lower threshold reaches the value of the lowpass filtered HSE signals earlier, but it does not enhance the performance qualitatively.

Single-flight experiments with different other textures show that the system performs well for most textures tested but fails for some textures similar to the natural textures used in the behavioural experiments. Furthermore, the performance of the system for a given texture can be reduced dramatically by reducing the contrast of this texture. This indicates that the contrast sensitivity of the sensory system may cause these results. In contrast to the blowfly system, the sensory module does not contain contrast saturation. Introducing such a saturation may lead to a more robust behaviour of the system in low-contrast environments. A recent study proposes a simple motion adaptation mechanism which is shown to largely reduce the sensitivity of the sensory module for contrast changes (Shoemaker et al., 2005). Such a mechanism should be integrated in the sensory module for further studies.

5.5 Summary and Discussion

The sections above describe the closed-loop simulation of a simple hypothetical control scheme based on the responses of the sensory neuronal model discussed in chapter 4. The results show that visual navigation based on the signals of HSE neurons is possible. Two different basic behaviours can be generated on basis of these signals. On the one hand, the HSE responses can serve as input to a module implementing the so-called optomotor response, on the other hand, saccadic obstacle avoidance can be implemented based on these signals.

The results obtained with a continuous optomotor-like coupling show that an optomotor controller parameterised to create a realistic response to pure rotational stimuli is incapable of controlling a wall avoidance. It has been shown in different studies, that such a circuit can correct for systematic asymmetries of the motor system of a robot (Webb and Harrison, 2000; Webb et al., 2004). A similar circuit also is able to implement some fixation reflexes as observed in fly behaviour (Huber et al., 1999). Principally, obstacle avoidance can also be achieved by balancing the optic flow on both sides of a translating animal.

However, it is unlikely that such a circuit generating continuous rotations will show both the optomotor response and an obstacle avoidance behaviour for a theoretical reason. During translational movement, both HSE cells are confronted with front-to-back optic flow. If the translation is overlayed by a rotation, the velocity of this flow is reduced on one and increased on the other eye. For instance, for an overlayed turn to the right, the left eye is confronted by faster flow than the right eye. A similar asymmetry is caused by a closer object on one side of the system. If e.g. the left wall in a tunnel is closer than the right one, the left side again faces a faster optic flow compared to the right side. However, the appropriate response to both situations should have the opposite sign. To compensate an overlayed turn, the system has to turn towards the side confronted with the faster flow (the turn to the right in the example must be compensated by steering leftward), while it must avoid this side for the wall avoidance task (the close wall on the left side would be avoided by steering rightward).

On the basis of spatially integrated horizontal flow information the system cannot distinguish between the two situations described above. Nonetheless, the optic flow fields differ between these situations. The focus of expansion, indicating the direction of movement, is located frontally if the system translates forward. If this situation is detected, the system can safely assume an asymmetry to indicate an object and respond by avoidance of the larger flow. Otherwise, the system may correct for the rotation causing the lateral position of the focus of expansion.

The closed-loop simulations using the saccadic control scheme show that this behavioural paradigm can indeed separate the rotational and translational components of the optic flow and thereby enable a controller to respond correctly to the translational flow information coded in the signals of large-field motion sensitive neurons. However, the sign of the successful turning response to an asymmetry in the HSE signals shows, that the inherent ambiguities of the motion detection system cannot be resolved by this approach either. A saccadic controller thus also has no chance to detect solely on the basis of these signals, if a small response of the HSE neuron is caused by small translational flow and thus by far distant objects or by very high velocities caused by nearby objects.

However, for future modelling attempts this observation could guide changes in the controller design or controller strategy. The signals of additional sensors such as the other HS or the vertically sensitive VS cells could be used by the controller to distinguish between the two possible reasons for a low HSE response during forward translation.

Furthermore, additional signals could be used to control other flight parameters such as thrust, pitch or height above the simulated ground.

Another possible strategy for the system, completely different from the one described above, could be to actively search for movements that maximise the response of both HSE neurons. While this would lead the virtual fly into the vicinity of objects on the one hand, it also keeps the system at a safe distance to these objects. Both a large and a small distance would then cause the signal of the HSE cell to drop beyond the maximal value, either because of low optic flow or because of large velocities in their receptive fields.

The simple control scheme described above randomly chooses the amplitude of the saccades. While this keeps the system simple, it is by no means a plausible strategy for the fly. The saccadic amplitude could for example very well be generated from the differential HSE response. The larger the asymmetry in the signal amplitudes, the larger a saccade could be.

6 Summary, outlook and conclusion

The navigational system of the virtual fly presented in this thesis can be decomposed into a sensory module and a sensor-motor coupling module. Both modules were implemented and tested as described in the previous chapters. Much of the knowledge used in this implementation was derived from the large amount of literature published over five decades of research in the field of optic flow processing in insect brains. A short overview of the knowledge relevant for this theses is given in chapter 2.

Although the algorithms implemented in the sensory module described in chapter 4 are described in detail in the literature, the response of a joint implementation of all these components to image sequences a fly is typically confronted to in behaviour had to be tested.

Chapter 3 describes several technical tools necessary to generate such image sequences and to replay these sequences to a real fly to get a benchmark for the calibration of the sensory model. The first step in this process is the quantitative analysis of behavioural experiments which is aided by the computer vision system presented in section 3.4. Using computer graphics methods the image sequences a fly has seen can be reconstructed from the flight trajectory and a 3D-model of the experimental setup using computer graphics techniques as described in section 3.2. These image sequences can then be replayed to the fly. Because of the almost panoramic visual field of the fly's facet eyes and its very fast photoreceptors this replay necessitates a special purpose device, the FliMax described in section 3.3, for presentation of these images.

The possibility to confront a fixated fly in an electrophysiological experiment with image sequences that represent what a fly sees in a behavioural experiment revealed that some of the conclusions drawn from experiments using more classical stimuli were incomplete. These experiments revealed that cells previously interpreted to act mainly as rotational sensors also encode translational information in their signals in a potentially useful form.

While these results were unexpected, the computational model of the sensory pathway is able to reproduce these results quantitatively as shown in chapter 4. The model described there has the long-known computational structure. However, this analysis is the first one calibrating the model parameters systematically with respect to behaviourally generated stimuli. This analysis reveals that the model is astonishingly robust against parameter changes when stimulated with behaviourally generated image sequences which again is an unexpected result because the same model is far less robust, if classical stimuli are used for the calibration. An important result of the model study was that the parameters determined by classical stimulation lead also to a model response to behaviourally generated stimuli that qualitatively fits the biological counterpart. Although these are not the optimal parameters for this fit, this result makes clear that there is no obvious adaptational change in the system properties between the different experimental situations.

Based on the resulting sensory module, the implementation of hypothetical sensor-motor coupling modules is possible. By a simple dynamical model of the flight mechanics, the control loop is closed and flights of the virtual fly in a simulation experiment are possible. Examples for such controller modules and results of simulation experiments were described in chapter 5.

These simulation experiments show that the avoidance of obstacles and the stabilisation of the flight direction using visual information coded in only two neurons of the fly brain can indeed be concurrently mimicked by such a system. Nevertheless, the experiments using a different wall texture or an additional object also make clear that both the sensory module and the sensor-motor coupling are still far from a perfect model of the fly neuronal system. Different extensions are necessary to make the system more robust against changes of the environmental structure. Furthermore, the system as described above is, so far, only capable to steer in two of the six degrees of freedom a real fly successfully controls.

6.1 Outlook

The research tools and the simulation model discussed so far can be extended in many respects. The following sections describe some possible directions of further development.

6.1.1 Extension of the model system

The model system as presented in chapters 4 and 5 covers only a small part of the known neuronal structures and the behavioural repertoire of the blowfly.

Additional sensory features

Additional to the HSE neuron modelled as described in chapter 4, the fly has at least 12 other large-field motion sensitive output neurons in each visual hemisphere. These cells are characterised anatomically and physiologically and they seem to be very similar in their overall structure and function to the HSE neuron. They clearly differ in the positions of their receptive fields and in their preferred directions of motion, but they seem to be comparable in respect to their computational properties. Thus it should be straightforward to adapt the model to these cells and to jointly compute the activity pattern of the whole ensemble formed by these neurons.

While these wide-field neurons are thought to analyse the aspects of the optic flow that reflect the self-motion of the animal, other neurons specialised on detecting discontinuities in the flow flied are possible sources of information on small objects in the visual field of the fly. Models of such neurons could further extend the sensory module of the virtual fly.

Sensor-motor coupling

The sensor-motor coupling scheme described in chapter 5 is based on hypotheses resulting from behavioural experiments. Without further insights into the neuronal networks of the fly brain processing the tangential cell signals, no real constraints exist for the computational structure of such a coupling.

Heuristic optimisation methods such as genetic algorithms and genetic programming or machine learning paradigms could aid the design of such a coupling.

One possible approach could be to optimise the entire coupling mechanism with respect to a certain task. For example, the task could be to avoid the walls in a given environment. The coupling could then be modelled as an artificial neural network which is optimised by reinforcement learning. The tangential cell signals would be the input for the network, the forces generated by the virtual fly would be the output. The duration of simulated flights using a candidate network could be the "reward" used by the training algorithm to optimise the network. Since the signals of the tangential cells may have crucial information in their time structure which would lead to different interpretation of a given activation pattern depending on the history of the signals, it might be useful to model the controller with a method that allows such dependencies to be discovered.

Another approach to the design of the coupling mechanism could be to split the controller and optimise the components individually. For example, the saccade generating module of the controller discussed in chapter 5 could be replaced by an artificial neural network which is optimised in a supervised learning paradigm using experimental data. The data used for the calibration of the sensory model (see chapter 4) could easily be used for such an optimisation. The input of the network would then be the sensory neuronal signals (either of the HSE neurons or of a simulated tangential cell ensemble) and the output to be learned would be a representation of the timing, amplitude, and direction of saccades. If the network is able to predict the saccades generated by the real fly from the signals of the sensory neuron, it could be used as a saccade generation module in the controller of the virtual fly. Furthermore, an analysis of such a network could give hints to neurophysiologists to search for certain couplings in the brain of the real fly e.g. if only a part of the neuronal ensemble activity is evaluated by the network.

6.1.2 Recording of behavioural data

Recording of behavioural data with fixed camera positions has the drawback, that the camera images need to show the entire experimental setup.

An active camera system that tracks the movements of the animal, would allow the observation using smaller viewing angles and thereby would increase the effective resolution of the animal in the camera image. This would allow the reconstruction of the head's trajectory from a video sequence which is the relevant trajectory for the analysis of optic flow processing.

Such a system could be constructed with relatively little effort using standard high speed cameras mounted as a stereo camera system on a pan-tilt motor controlled by a real-time vision system equipped with a camera viewing the entire setup (see figure 6.1). This camera does not need to have the temporal resolution necessary for the detailed analysis of behaviour, because the task of this system would only be to ensure that the animal is in view of the high speed cameras throughout the entire recording time. Since the position of the animal does not have to be reconstructed very precisely for the control task, the spatial resolution of the controlling could be low, making the real time image processing feasible.

6.1.3 FliMax in closed loop

The FliMax stimulation device was only used for replay experiments, so far. In such experiments, the neuronal responses to a prepared set of stimuli can be recorded. The resulting data are valuable material for the system analysis of the neuronal circuits processing the stimuli.

However, the same device can be used for online stimulation in a simulated closed loop experiment. In such an experiment either behavioural or neuronal responses of an animal can be coupled to the temporal development of the stimuli. The electrophysiologically recorded signals of certain neurons or the reactions of a tethered flying animal could be used as the input to a flight simulator in a animal-computer hybrid.

The hardware described in section 3.3 allows such an approach, if the software is extended appropriately. The Linux version of the driver code is already prepared to display stimuli generated in real time. However, the current implementation

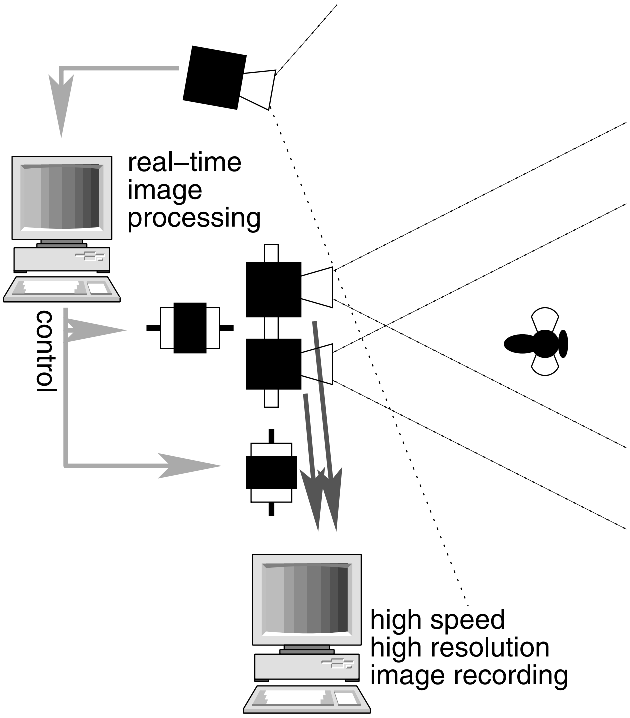

Figure 6.1: Schematic drawing of a possible active behavioural recording setup. Based on the real time processing of the images of a low resolution and low speed camera, the viewing direction of a high speed stereo recording system can be controlled. The active movements of the recording cameras allow a small viewing angle and thereby a high resolution of the observed animal.

of the rendering process is far to slow for this task. A major acceleration of this part of the software could be achieved by the use of the 3D acceleration offered by modern graphics hardware.

Another precondition for simulated closed-loop experiments is the real time recording of behavioural responses. The tracking of wing beats as described in section 3.4 could be coupled to simulated movements of the animal. Prior closed-loop experiments have already shown that flies show interesting behaviours in such a setup.

6.1.4 Further development of the wingbeat analyser

The wing beat analysis could be extended in order to record wing beat parameters initiating the saccadic rotations observed in free flight. As discussed in section 3.4.3, the current data analysis did not reveal a saccade-like event, but the real fly obviously is able to initiate saccadic turns so that such an event must be present in the wing beat pattern. One aspect of the pattern not yet analysed is the rotation of the wing about its long axis. This rotation should cause modulations in the width of the wing as seen from the tracking camera and if these can be extracted, they might be the key to saccadic turn initiation.

6.2 Conclusion

Flies are more or less nothing but bothersome for most people. The artistic flight manoeuvres of these animals and the amazing capabilities these animals gain from their small brains make them even more annoying, because they make it very difficult to catch a fly. Viewed from a different perspective, these small flying animals are highly interesting creatures. With a brain weighing only a view milligrams they solve several problems that are still challenging tasks for artificial systems.

Flies are able to avoid obstacles in their flight path on the basis of visual information. Simultaneously they use the same source of information to control their orientation in respect to the environment and to stabilise their flight path. To solve these problems, evolution developed algorithms that are amazingly robust against changes in environmental structure. Flies are able to navigate not only in a wide variety of natural habitats, but also in artificial environments like human buildings.

The part of the neuronal system of the fly analysing this information is one of the best known neuronal circuits in animal kingdom. The neuronal structures of the fly motion vision system were analysed with behavioural as well as neuroanatomical and neurophysiological techniques over several decades. A detailed algorithmic model for the computations implemented by this neuronal network was derived in these studies.

For technical autonomous systems such a visual control is associated with a very high computational effort. Visual navigation systems also typically rely on certain structural features of the environment and thus lack the robustness observed in biological systems. Some of these technical systems are already inspired by the computational strategies flies use to analyse the visual information.

This thesis presents contributions to the attempt to mimic the fly navigation and flight control in an artificial system here called the virtual blowfly. Building such a virtual fly is interesting for biological research as a test-bed for hypotheses on the computational structure of the fly neuronal system, on the one hand, and for engineers constructing autonomous robots as a source of more inspiration, on the other hand.

Bibliography

Bab-Hadiashar A, Suter D (1998) Robust Optic Flow Computation. International Journal of Computer Vision 29: 59–77.

Ballard DH, Brown CM (1982) Computer Vision. Prentice Hall.

Barron JL, Fleet DJ, Beauchemin SS (1994) Performance of Optical Flow Techniques. Internation Journal of Computer Vision 12: 43–77.

Beauchemin SS, Barron JL (1995) The Computation of Optical Flow. ACM Computing Surveys 27: 433–467.

Bialek W, Rieke F, d van Steveninck R, Warland D (1991) Reading a neural code. Science 252: 1854–1857.

Blanchard M, Rind FC, Verschure PFMJ (2000) Collision avoidance using a model of the locust LGMD neuron. Robotics and Autonomous Systems 30: 17–38.

Boeddeker N, Kern R, Egelhaaf M (2003) Chasing a dummy target: smooth pursuit and velocity control in male blowflies. Proceedings of the Royal Society London B pp. 393–400.

Boeddeker N, Lindemann JP, Egelhaaf M, Zeil J (2005) Responses of blowfly motion-sensitive neurons to reconstructed optic flow along outdoor flight paths. Journal of Comparative Physiology A DOI: 10.1007/s00359-005-0038-9.

Borst A (1986) Time Course of the Houseflies' Landing Response. Biological Cybernetics 54: 379–383.

Borst A (2000) Models of motion detection. Nature Neuroscience Supplement 3: 1168.

Borst A, Egelhaaf M (1987) Temporal modulation of luminance adapts time constant of fly movement detectors. Biological Cybernetics 56: 209–215.

Borst A, Egelhaaf M (1989) Principles of visual motion detection. Trends in Neuroscience 12: 297–306.

Borst A, Egelhaaf M (1993a) Detecting visual motion: Theory and models. In: Miles F, JWallman, editors, Visual Motion in the Stabilization of Gaze, pp. 3–27, Elsevier.

Borst A, Egelhaaf M (1993b) Processing of synaptic signals in fly visual interneurons selectively responsible to small moving objects. In: Aertsen A, editor, Brain Theory, pp. 47–66, Elsevier.

Borst A, Egelhaaf M, Haag J (1995) Mechanisms of dendritic integration underlying gain control in fly motion-sensitive interneurons. Journal of Computational Neuroscience 2: 5–18.

Borst A, Haag J (1996) The Intrinsic Electrophysiological Characteristics of Fly Lobula Plate Tangential Celss: I. Passive Membrane Properties. Journal of Computational Neuroscience 3: 313–336.

Borst A, Haag J (2002) Neural networks in the cockpit of the fly. Journal of Comparative Physiology A 188: 419–437.

Borst A, Reisenman C, Haag J (2003) Adaptation of response transients in fly motion vision. II: Model studies. Vision Research 43: 1309–1322.

Brady M, Wang H (1992) Vision for Mobile Robots. Philosophical Transactions of the Royal Society London B 337: 341–350.

Brenner N, Bialek W, de Ruyter van Steveninck R (2000) Adaptive Rescaling Maximises Information Transmission. Neuron 26: 695–702.

Bruhn A, Weickert J (2005) Lucas/Kanade Meets Horn/Schunck: Combining Local and Global Optic Flow Methods. International Journal of Computer Vision 61: 1–21.

Calow D, Krüger N, Wörgötter F, Lappe M (2004) A biologically motivated mid-level stage for robust optic flow processing. In: Early Cognition Vision Workshop.

Chellappa R, Zheng Q (1995) Automatic Feature Point Extraction and Tracking in Image Sequences for Arbitrary Camera Motion. International Journal of Computer Vision 15: 31–76.

Cuntz H, Haag J, Borst A (2003) Neural image processing by dendritic networks. Proceedings of the National Acedemy of Sciences USA 100: 11082–11085.

Dahmen H, Wüst RM, Zeil J (1997) Extracting egomotion from optic flow: principal limits for animals and machines. In: Srinivasan M, Venkatesh S, editors, From Living Eyes to Seeing Machines, pp. 174–198, Oxford University Press.

Dahmen HJ, Franz MO, Krapp HG (2001) Extracting Egomotion from Optic Flow: Limits of Accuracy and Neural Matched Filters. In: Zanker JM, Zeil J, editors, Motion Vision — Computational, Neural, and Ecological Constraints, pp. 143–168, Springer.

de Ruyter van Steveninck R, Bialek W (1988) Real-time performance of a movement-sensitive neuron in the blowfly visual system: Coding and information transfer in short spike sequences. Proceedings of the Royal Society London B 234: 379–414.

Dev A, Kröse BJA, c A Groen F (1996) Confidence Measures for Image Motion Estimation. In: Proceedings 1997 RWC Symposium, no. 96001 in RWC Technical Report TR, pp. 199–206.

Dickinson MH, Lehmann FO, Sane SP (1999) Wing Rotation and the Aerodynamic Basis of Insect Flight. Science 284: 1954–1960.

Douglass JK, Strausfeld NJ (2001) Pathways in Dipteran Insects for Early Visual Motion Processing. In: Zanker JM, Zeil J, editors, Motion Vision — Computational, Neural, and Ecological Constraints, pp. 67–81, Springer.

Dror RO, O'Carroll DC, Laughlin SB (2001) Accuracy of velocity estimation by Reichardt correlators. Journal of the Optical Society of America A 18: 241–252.

Eckert H, Hamdorf K (1981) The contrast frequency-dependence: A criterion for judgung the non-participation of neurones in the control of behavioural responses. Journal of Comparative Physiology A 145: 241–247.

Egelhaaf M (1985) On the Neuronal Bassi of Figure-Ground Discrimination by Relative Motion in the Visual System of the Fly I. Behavioural Constraints Imposed on the Neuronal Network and the Role of the Optomotor System. Biological Cybernetics 52: 123–140.

Egelhaaf M (1987) Dynamic properties of two control systems unerlying visually guided turning in house-flies. Journal of Comparative Physiology A 161: 777–783.

Egelhaaf M, Borst A (1989) Transient and steady-state response properties of movement detectors. Journal of the Optical Society of America A 6: 116–126.

Egelhaaf M, Borst A (1993) Movement detection in arthropods. In: Miles F, JWallman, editors, Visual Motion in the Stabilization of Gaze, pp. 53–77, Elsevier.

Egelhaaf M, Borst A, Reichardt W (1989) Computational structure of a biological motion-detection system as revealed by local detector analysis in the fly's nervous system. Journal of the Optical Society of America A 6: 1070–1087.

Egelhaaf M, Kern R, Kurtz R, Krapp HG, Kretzberg J, et al. (2002) Neural encoding of behaviourally relevant motion information in the fly. Trends in Neuroscience 25: 96–102.

Egelhaaf M, Reichardt W (1987) Dynamic Response Properties of Movement Detectors: Theoretical Analysis and Electrophysiological Investigation in the Visual System of the Fly. Biological Cybernetics 56: 69–87.

Egelhaaf M, Warzecha AK (1999) Encoding of motion in real time by the visual system. Current Opinon in Neurobiology 9: 454–460.

Fairhall AL, Lewen GD, Bialek W, de Ruyter van Steveninck RR (2001) Efficiency and ambiguity in an adaptive neural code. Nature 412: 787–792.

Franceschini N, Pichon JM, Blanes C (1992) From insect vision to robot vision. Philosophical Transactions of the Royal Society London B 337: 283–294.

Franz MO, Chahl JS (2002) Linear Combinatios of Optic Flow Vectors for Estimating Self-Motion – A Real-World Test of a Neural Model. In: NIPS.

Franz MO, Krapp HG (1998) Wide-Field, Motion-Sensitive Neurons and Optimal Matched Filters for Optic Flow. Technical Report 61, Max-Planck-Institut für biologische Kyberntik, Tübingen.

Fry SN, Sayaman R, Dickinson MH (2003) The Aerodynamics of Free-Flight Maneuvers in Drosophila. Science 300: 495–498.

Gabbiani F, Mo C, Laurent G (2001) Invariance of Angular Threshold Computation in a Wide-Field Looming-Sensitive Neuron. Journal of Neuroscience 21: 314–329.

Gerthsen C, Volgel H (1997) Physik. 19th ed., Springer.

Gibson JJ (1950) The Perception of the Visual World. Hougthon Mifflin.

Gonzales RC, Woods RE (2002) Digital Image Processing. 2nd ed., Prentice-Hall.

Götz KG (1964) Optomotrische Untersuchungen des visuellen Systems einiger Augenmutanten der Fruchtfliege Drosophila. Kybernetik 2: 77–92.

Götz KG (1968) Flight Control in Drosophila by Visual Perception of Motion. Kybernetik 4: 199–208.

Götz KG (1975a) The optomotor equilibrium of the Drosophila navigation system. Journal of Comparative Physiology 99: 187–210.

Götz KG (1975b) The Optomotor Equilibrium of the Drosophila Navigation System. Journal of Comparative Physiology 99: 187–210.

Götz KG (1983) Bewegungssehen unf Flugsteuerung der der Fliege Drosophila. In: Nachtigall W, editor, Biona-report 2, pp. 20–35, Urban & Fischer.

Götz KG (1987) Course-Control, Metabolism and Wing Interference During Ultralong Tethered Flight in Drosophila melanogaster. Journal of Experimental Biology 128: 35–46.

Götz KG, Wenking H (1973) Visual Control of Locomotion in the Walking Fruitfly Drosophila. Journal of Comparative Physiology 85: 235–266.

Haag J, Borst A (1997) Encoding of Visual Motion Information and Reliability in Spiking and Graded Potential Neurons. Journal of Neuroscience 17: 4809–4819.

Haag J, Borst A (1998) Active Membrane Properties and Signal Encoding in Graded Potential Neurons. Journal of Neuroscience 18: 7972–7986.

Haag J, Borst A (2003) Orientation tuning of motion-sensitive neurons shaped by vertical–horizontal network interactions. Journal of Comparative Physiology A 189: 363–370.

Haag J, Borst A (2004) Neural mechanism underlying complex receptive field properties of motion-sensitive interneurons. Nature Neuroscience 7: 628–634.

Haag J, Egelhaaf M, Borst A (1992) Dendritic integration of visual motion information in the fly. Neuroscience Letters 140: 173–176.

Haag J, Theunissen F, Borst A (1997) The Intrinsic Electrophysiological Characteristics of Fly Lobula Plate Tangential Cells: II. Active Membrane Properties. Journal of Computational Neuroscience 4: 349–369.

Hardie R (1985) Functional organization of the fly retina. In: Autrum H, editor, Progress in Sensory Physiology, vol. 5, pp. 1–79, Springer.

Harris RA, O'Carrol DC, Laughlin SB (1999a) Adaptation and the temporal delay filter of fly motion detectors. Vision Research 39: 2603–2613.

Harris RA, O'Carroll DC (2002) Afterimages in fly motion vision. Vision Research 42: 1701–1714.

Harris RA, O'Carroll DC, Laughlin SB (1999b) Two components of motion adaptation in the fly. Journal of Physiology 513P: 105P–106P.

Harris RA, O'Carroll DC, Laughlin SB (2000) Contrast Gain Reduction in Fly Motion Adaptation. Neuron 28: 595–608.

Harrison RR, Koch C (1999) A robust analog VLSI motion sensor. Autonomous Robots 7: 211–224.

Harrison RR, Koch C (2000) A Silicon Implementation of the Fly's Optomotor Control System. Neural Computation 12: 2291–2304.

Hassenstein B, Reichardt W (1956) Systemtheoretische Analyse der Zeit-, Reihenfolgen- und Vorzeichenauswertung bei der Bewegungsperzeption des Rüsselkäfers Chlorophanus. Zeitschrift für Naturforschung 11b: 513–524.

Hausen K (1982a) Motion Sensitive Interneurons in the Optomotor System of the Fly I. The Horizontal Cells: Structure and Signals. Biological Cybernetics 45: 143–156.

Hausen K (1982b) Motion Sensitive Interneurons in the Optomotor System of the Fly II. The Horizontal Cells: Receptive Field Organization and Response Characteristics. Biological Cybernetics 46: 67–79.

Hausen K (1984) The lobula-complex of the fly: Structure, function and significance in visual behavior. In: Ali M, editor, Photoreception and Vision in Invertebrates, pp. 523–559, Plenum Press.

Hausen K, Egelhaaf M (1989) Neural mechanisms of visual course control in insects. In: Stavenga D, Hardie R, editors, Facets of vision, pp. 391–424, Springer-Verlag, Berlin Heidelberg.

Heisenberg M, Wolf R (1984) Vision in drosophila : genetics of microbehavior. Springer.

Hengstenberg R (1977) Spike responses of 'non-spiking' visual interneurone. Nature 270: 338–340.

Hengstenberg R (1982) Common Visual Response Properties of Giant Vertical Cells in the Lobula Plate of the Blowfly Calliphora. Journal of Comparative Physiology A 149: 179–193.

Hengstenberg R, Hausen K, Hengstenberg B (1982) The Number and Structure of the Giant Vertical Cells (VS) in the Lobula Plate of the Blowfly Calliphora erythrocephala. Journal of Comparative Physiology A 149: 163–177.

Hengstenberg R, Sandeman DC, Hengstenberg B (1986) Compensatory head roll in the blowfly Calliphora during flight. Proceedings of the Royal Society London B 227: 455–482.

Hildreth EC (1984) The measurement of visual motion. MIT Press.

Horstmann W, Egelhaaf M, Warzecha AK (2000) Synaptic interactions increase optic flow specificity. European Journal of Neuroscience 12: 2157–2165.

Huber SA, Franz MO, Bülthoff HH (1999) On robots and flies: Modeling the visual orientation behavior of flies. Robotics and Autonomous Systems 29: 227–242.

Jähne B (1997) Digitale Bildverarbeitung. 4th ed., Springer.

James AC (1990) White-noise studies in the fly lamina. Ph.d.-thesis, Australian National University.

Jansonius N, van Hateren J (1991) Fast temporal adaption of on-off units in the first optic chiasm of the blowfly. Journal of Comparative Physiology A 168: 631–637.

Jansonius N, van Hateren J (1993) On-off units in the first optic chiasm of the blowfly I. Spatial Properties. Journal of Comparative Physiology A 172: 467–471.

Juusola M, French AS, Uusitalo RO, Wecström M (1996) Information processiong by graded-potential transmission through tonically active synapses. Trends in Neuroscience 19: 292–297.

Juusola M, Weckström M, Uusitalo RO, Korenberg MJ, French AS (1995) Nonlinear Models of the First Synapse in the Light Adapted Fly Retina. Journal of Neurophysiology 74: 2538–2547.

Karmeier K, Krapp HG, Egelhaaf M (2003) Robustness of the Tuning of Fly Visual Interneurons to Rotatory Optic Flow. Journal of Neurophysiology 90: 1626–1634.

Karmeier K, Krapp HG, Egelhaaf M (2005) Population Coding of Self-Motion: Applying Bayesian Analysis to a Population of Visual Interneurons in the Fly. Journal of Neurophysiology 94: 2182–2194.

Kent J (1993) The Flic File Format. Dr Dobbs Journal 18: 18–22.

Kern R, Lutterklas M, Egelhaaf M (2000) Neuronal representation of optic flow experienced by unilaterally blinded flies on their mean walking trajectories. Journal of Comparative Physiology A 186: 467–479.

Kern R, Lutterklas M, Petereit C, Lindemann JP, Egelhaaf M (2001a) Neuronal processing of behaviourally generated optic flow: experiments and model simulations. Network: Computation in Neural Systems 12: 351–369.

Kern R, Petereit C, Egelhaaf M (2001b) Neural Processing of Naturalistic Optic Flow. Journal of Neuroscience 21: 1–5.

Kern R, van Hateren JH, Egelhaaf M (2005a) Representation of behaviourally relevant information by motion sensitive visual interneurons requires precise compensatory head movements, submitted.

Kern R, van Hateren JH, Michaelis C, Lindemann JP, Egelhaaf M (2005b) Function of a Fla Motion Sensitive Neuron Mathes Eye Movements during Free Flight. PLoS Biology 3: 1130–1138.

Kimmerle B, Egelhaaf M (2000) Detection of object motion by a fly neuron during simulated flight. Journal of Comparative Physiology A 186: 21–31.

Kimmerle B, Eickermann J, Egelhaaf M (2000) Object Fixation by the Blowfly During Tethered Flight in a Simualted Three-Dimensional Environment. Journal of Experimental Biology 203: 1723–1732.

Kimmerle B, Warzecha AK, Egelhaaf M (1997) Object detection in the fly during simulated translatory flight. Journal of Comparative Physiology A 181: 247–255.

Koch C (1999) Biophysics of computation : information processing in single neurons. Oxford University Press.

Koenderink JJ (1986) Optic Flow. Vision Research 26: 61–180.

Koenderink JJ, van Doorn AJ (1987) Facts on Optic Flow. Biological Cybernetics 56: 247–254.

Krapp HG, Hengestenberg B, Hengstenberg R (1998) Dendritic Structure and Receptive-Field Organization of Optic Flow Processing Interneurons of the Fly. Journal of Neurophysiology 79: 1902–1917.

Krapp HG, Hengstenberg R (1996) Estimation of self-motion by optic-flow processing in single visual interneurons. Nature 385: 463–466.

Krapp HG, Hengstenberg R, Egelhaaf M (2001) Binocular Contributions to Optic Flow Processing in the Fly Visual System. Journal of Neurophysiology 85: 724–734.

Kurtz R, Dürr V, Egelhaaf M (2000) Dendritic calcium accumulation associated with direction selective adaptation in visual motion sensitive neurons in vivo. Journal of Neurophysiology 84: 1914–1923.

Laughlin S (1984) Parallel channels in the arthropod compound eye. In: Ali M, editor, Photoreception and Vision in Invertebrates, pp. 457–481, Plenum Press.

Laughlin SB (1994) Matching coding, circuits, cells, and molecules to signals: General principles of retinal design in the fly's eye. Progr Ret Eye Res 13: 165–196.

Lehmann FO, Dickinson MH (1997) The Changes in Power Requirements and Muscle Efficiency During Elevated Force Production in the Fruit Fly Drosophila Melanogaster. Journal of Experimental Biology 200: 1133–1143.

Lehmann FO, Dickinson MH (2001) The Production of elevated flight force compromises manoeuverability in the fruit fly drosophila melanogaster. Journal of Experimental Biology 205: 627–635.

Lewis MA (1998) Visual Navigation in a Robot using Zig-Zag Behavior. NIPS 10: 822–828.

Lindemann JP, Kern R, Michaelis C, Meyer P, van Hateren JH, et al. (2003) Flimax, a novel stimulus device for panoramic and highspeed presentation of behaviorally generated optic flow. Vision Research 43: 779–791.

Lindemann JP, Kern R, van Hateren JH, Ritter H, Egelhaaf M (2005) On the Computations Analyzing Natural Optic Flow: Quantitative Model Analysis of the Blowfly Motion Vision Pathway. Journal of Neuroscience 25: 6435–6448.

Lutterklas M (1996) Flugbahnanlyse und Simulation retinaler Reizmuster. Diplomarbeit, Technische Fakultät der Universität Bielefeld.

Maddess T, Laughlin SB (1985) Adaptation of the motion-sensitive neuron H1 is generated locally and governed by contrast frequency. Proceedings of the Royal Society London B 225: 251–275.

Nachtigall W (1977) Zur Bedeutung der Reynoldszahl und der damit zusammenhängenden strömungsmechanischen Rhänomene in der Schwimmphysiologie und Flugphysik. Fortschritte der Zoologie 24: 13–56.

Nachtigall W (2001) Some aspects of Reynolds number effects in animals. Mathematical Methods in the applied sciences 24: 1401–1408.

Nalbach G (1994) Extremely non-orthogonal axes in a sense organ for rotation: Behavioural analysis of the dipteran haltere system. Neuroscience 61: 149–163.

Neumann TR (2002) Modeling Insect Eyes: Space-Variant Spherical Vision. In: Bülthoff HH, Lee SW, Poggio T, Wallraven C, editors, Proceedings of the 2nd International Workshop on Biologically Motivated Computer Vision, vol. 2525 of Lecture Notes in Computer Science, pp. 360–367, Springer.

Neumann TR (2004) Biomimetic Spherical Vision. Phd-thesis, Universität Tübingen.

O'Carroll DC, Laughlin SB, Bidwell NJ, Harris RA (1997) Spatio-Temporal Properties of Motion Detectors Matched to Low Velocities in Hovering Insetcs. Vision Research 37: 3427–3439.

Petereit C (2002) Grenzen der Linearität: Wie kodieren HS-Neuronen der Fliege verhaltensgenerierten optischen Fluss? Diplomarbeit, Universität Bielefeld.

Petrowitz R, Dahmen H, Egelhaaf M, Krapp HG (2000) Arrangement of optical axes and spatial resolution in the compund eye of the female blowfly Calliphora. Journal of Comparative Physiology A 186: 737–746.

Reichardt W (1973) Musterinduzierte Flugorientierung – Verhaltens-Versuche an der Fliege Musca Domestica. Naturwissenschaften 60: 122–138.

Reichardt W, Poggio T (1976) Visual Control of orientation behaiour in the fly Part: I. A quantitative analysis. Quaterly Reviews of Biophysics 9: 311–375.

Reichardt W, Varjú D (1959) Übertragungseigenschaften im Auswertesystem für das Bewegungssehen. Zeitschrift für Naturforschung 14b: 674–689.

Reisenman C, Haag J, Borst A (2003) Adaptation of response transients in fly motion vision. I: Experiments. Vision Research 43: 1291–1307.

Reiser MB, Dickinson MH (2003) A test bed for insect-inspired robotic control. Philosophical Transactions of the Royal Society London A 361: 2267–2285.

Roberts K, Coombs D (1993) Centering Behavior Using Peripheral Vision. In: IEEE Compter Society Conference On Computer Vision And Pattern Recognition, pp. 440–445.

Schenato L, Deng X, Wu WC (2001) Virtual Insect Flight Simulator (VIFS): A Software Testbed for Insect Flight. In: IEEE Int. Conf. Robotics and Automation, pp. 3885–3892.

Schilstra C, van Hateren J (1998a) Using minitaure sensor coils for simultaneous measurement of orientation and position of small, fast-moving animals. Journal of Neuroscience Methods 83: 125–.

Schilstra C, van Hateren J (1999) Blowfly Flight and Optic Flow. I. Thorax Kinematics and Flight Dynamics. Journal of Experimental Biology 202: 1481–1490.

Schilstra C, van Hateren JH (1998b) Stabilizing gaze in flying blowflies. Nature 395: 654.

Shoemaker PA, O'Carroll DC, Straw AD (2005) Velocity constancy and models for wide-field visual motion detection in insects. Biological Cybernetics .

Smakman JG, van Hateren JH, Stavenga DG (1984) Angular sensitivity of blowfly photoreceptors: Intracellular measurements and wave-optical predictions. Journal of Comparative Physiology A 155: 239–247.

Sonka M, Hlavac V, Boyle R (1999) Image Processing, Analysis and Machine Vision. 2nd ed., PWS Publishing.

Srinivasan M, Zhang S (2003) Motion Cues in Insect Vision and Navigation. In: Chalupa LM, Werner JS, editors, The visual neurosciences, pp. 1193–1202, MIT Press.

Stöffler NO, Burkert T, Färber G (2000) Real-Time Obstacle Avoidance Using an MPEG-Processor-based Optic Flow Sensor. In: Proc. 15th Int. Conf. Pattern Recognition, pp. 161–166.

Strauss R, Schuster S, Götz KG (1997) Processing of artificial visual feedback in the walking fruit fly drosophila melanogaster. Journal of Experimental Biology 200: 1281–1296.

Sun H, Frost DJ (1998) Computation of different optical variables of looming objects in pigeon nucleus rotundus neurons. Nature Neuroscience 1: 296–303.

Tammero LF, Dickinson MH (2002a) Collision-avoidance and landing responses are mediated by separate pathways in the fruit fly, Drosophila melanogaster. Journal of Experimental Biology 205: 2785–2798.

Tammero LF, Dickinson MH (2002b) The influence of visual landscape on the free flight of the fruit fly Drosophila menlanogaster. Journal of Experimental Biology 205: 327–343.

Tatler B, O'Carroll DC, Laughlin SB (2000) Temperature an the temporal resolving power of fly photoreceptors. Journal of Comparative Physiology A 186: 399–407.

Tomasi C, Tian TY, Heeger DJ (1996) Comparison of Approaches to Egomotion Computation. In: IEEE Computer Society Conference on Computer Vision and Pattern Recognition, pp. 315–.

van Hateren J, Schilstra C (1999) Blowfly Flight and Optic Flow. II. Head Movements and Optic Flow. Journal of Experimental Biology 202: 1491–1500.

van Hateren JH, Kern R, Schwerdtfeger G, Egelhaaf M (2005) Function and Coding in the Blowfly H1 Neuron during Naturalistic Optic Flow. Journal of Neuroscience 25: 4343–4352.

van Hateren JH, Rüttiger L, Sun H, Lee B (2002) Processing of natural temporal stimuli by macaque retinal ganglion cells. Journal of Neuroscience 22: 9945–9960.

van Hateren JH, Snippe HP (2001) Information theoretical evaluation of parametric models of gain control in blowfly photoreceptor cells. Vision Research 41: 1851–1865.

Vázques F, Pay E, Marín R (1994) Real-Time Vision Based Navigation and 3D Depth Estimation for an Indoor Autonomous Mobile Robot. In: Crespo A, editor, Artificial Intelligence in Real Time Control 1994, pp. 221–226, Pergamon.

Warzecha AK, Egelhaaf M (1996) Intrinsic properties of biological motion detectors prevent the optomotor system from getting unstable. Philosophical Transactions of the Royal Society London B 351: 1579–1591.

Warzecha AK, Egelhaaf M (2001) Neuronal Encoding of Visual Motion in Real-Time. In: Zanker JM, Zeil J, editors, Motion Vision — Computational, Neural, and Ecological Constraints, pp. 239–277, Springer.

Warzecha AK, Kretzberg J, Egelhaaf M (1998) Temporal precision of the encoding of motion information by visual interneurons. Current Biology 8: 359–368.

Webb B, Harrison R (2000) Eyes and Ears: Combining Sensory Motor Systems Modelled on Insect Physiology. In: Proceedings of the 2000 IEEE International Conference on Robotics & Automation, pp. 3913–3918, San Francisco, CA.

Webb B, Harrison RR, Willis MA (2004) Sensorimotor control of navigation in arthropd and artificial systems. Arthropod Structure and Devlopment 33: 301–329.

Weiss H (2005) Closed-Loop Simulation der visuellen Kurssteuerung einer Fliege. Master's thesis, Technische Fakultät, Universität Bielefeld.